

Distribution Agreement

In presenting this thesis or dissertation as a partial fulfillment of the requirements for an advanced degree from Emory University, I hereby grant to Emory University and its agents the non-exclusive license to archive, make accessible, and display my thesis or dissertation in whole or in part in all forms of media, now or hereafter known, including display on the world wide web. I understand that I may select some access restrictions as part of the online submission of this thesis or dissertation. I retain all ownership rights to the copyright of the thesis or dissertation. I also retain the right to use in future works (such as articles or books) all or part of this thesis or dissertation.

Signature:

Date

**Development of Fluorescence-based Molecular Tension Probes
to Investigate Cellular Mechanical Forces**

By

Carol Jurchenko

Doctor of Philosophy

Chemistry

Khalid Salaita
Advisor

Dennis Liotta
Committee Member

David Lynn
Committee Member

Accepted:

Lisa A. Tedesco, Ph.D.
Dean of the James T. Laney School of Graduate Studies

Date

**Development of Fluorescence-based Molecular Tension Probes
to Investigate Cellular Mechanical Forces**

By

Carol Jurchenko

B.S. Kennesaw State University, 2009

Advisor: Khalid Salaita, Ph.D.

An abstract of

A dissertation submitted to the Faculty of the
James T. Laney School of Graduate Studies of Emory University

in partial fulfillment of the requirements for the degree of

Doctor of Philosophy

in Chemistry

2015

Abstract

**Development of Fluorescence-based Molecular Tension Probes
to Investigate Cellular Mechanical Forces**

By Carol Jurchenko

Mechanical forces are important in cellular development, normal morphogenesis, and wound healing. The mechanisms by which cells utilize tension to regulate biochemical events, however, are not well understood. In part, this is due to the limited availability of tools to study molecular mechanotransduction in live cells. The aim of this thesis is to describe the development and application of fluorescence-based sensors for mapping forces exerted by cell-surface proteins in living cells.

Chapter 1 describes the historical context and biological motivation for developing molecular tension fluorescence microscopy (MTFM) probes. This chapter includes an analysis of the available methods for measuring cellular forces and case studies of model mechanotransduction pathways.

Chapter 2 details the development of MTFM probes and their application in studying the forces associated with the initial stages of endocytosis of the ligand-activated epidermal growth factor receptor (EGFR). This work revealed that clathrin-mediated endocytosis of the EGFR is associated with pN scale forces and represents the first demonstration of a molecular probe to study forces applied by cell-surface receptors.

Chapter 3 explores integrin receptor forces, which are important in cell adhesion. An MTFM probe consisting of a cyclic RGD peptide conjugated to a polyethylene glycol polymer was surface immobilized through streptavidin-biotin linkage. Although

streptavidin-biotin binding affinity is described as the strongest noncovalent bond in nature, and is $\sim 10^6$ - 10^8 times larger than integrin-RGD affinity, this work led to the discovery that integrin receptors in focal adhesions mechanically dissociate streptavidin-biotin tethered ligands. These results suggest that integrin-ligand complexes undergo a marked enhancement in stability when assembled within focal adhesions.

In chapter 4, MTFM is used to examine the role of force in the activation of the Notch receptor, which plays a critical role in cell development. While the activation mechanism for Notch remains unclear, one widely accepted hypothesis involves force-mediated unfolding of the receptor that leads to cleavage by a metalloprotease, resulting in receptor activation. To validate this model, we engineered Notch MTFM probes and mapped Notch-ligand forces in live cells.

Chapter 5 concludes the thesis by summarizing the work and discussing future directions for MTFM probes.

**Development of Fluorescence-based Molecular Tension Probes
to Investigate Cellular Mechanical Forces**

By

Carol Jurchenko

B.S. Kennesaw State University, 2009

Advisor: Khalid Salaita, Ph.D.

A dissertation submitted to the Faculty of the
James T. Laney School of Graduate Studies of Emory University
in partial fulfillment of the requirements for the degree of
Doctor of Philosophy
in Chemistry

2015

Acknowledgements

First, I would like to acknowledge the guidance and perspective provided by my advisor, Khalid Salaita. His creativity and knowledge of science always brought a fresh approach to any problem that needed to be solved. I would also like to thank the two professors on my committee, David Lynn and Dennis Liotta. Dr. Lynn never failed to offer valuable advice when I came to him with questions and Dr. Liotta, with his gift of being simultaneously honest and kind, provided valuable support. I have benefited from both of their opinions on multiple occasions over the years.

I am also very grateful to the friends I have discovered along the way, specifically Kelly Kluge, Jen Bon, Omar Villanueva, and Yoshie Narui. All of them have kept me sane at various times throughout this process.

Finally, I would like to thank my wife who consistently sacrificed her time and energy to keep our life in order while giving me the freedom to pursue my goals. Without her support this work would not have been possible.

List of Frequently Used Abbreviations

Abbreviation	Full Name
ADAM	a disintegrin and metalloprotease
AFM	atomic force microscopy
AuNP	gold nanoparticle
cRGD	cyclic arginine-glycine-aspartate
DLL1	Delta-like protein 1
ECM	extracellular matrix
EGF	epidermal growth factor
eGFP	enhanced green fluorescent protein
EGFR	epidermal growth factor receptor
FA	focal adhesion
FRET	fluorescence resonance energy transfer
HD	heterodimerization domain
K_d	dissociation constant
k_{off}	dissociation rate
LNR	Lin12-Notch repeat
MTFM	molecular tension-based fluorescence microscopy
NECD	Notch extracellular domain
NICD	Notch intracellular domain
NRR	negative regulatory region
PEG	polyethylene glycol

pN	piconewton
QE	quenching efficiency
RICM	reflection interference contrast microscopy
S1, S2, S3	site 1, site 2, site 3
SLB	supported lipid bilayer
TACE	tumor necrosis factor- α converting enzyme
TIRF	total internal reflection fluorescence
TM	transmembrane

Table of Contents

Chapter 1. Mechanotransduction and Methods to Measure Cellular Tension.....	1
1.1 Role of molecular mechanotransduction in cell biology and biochemistry.....	2
1.1.1 A brief history of measuring molecular tension in live cells.....	2
1.1.2 Focal adhesions as a model mechanotransduction system	4
1.2 Emerging methods for measuring molecular tension	10
1.2.1 Genetically encoded tension sensors	14
1.2.2 Immobilized tension sensors.....	19
1.3 Outlook	24
1.4 References.....	29
Chapter 2. Visualizing mechanical tension across membrane receptors with a fluorescent sensor.....	46
2.1 Development of a fluorescence-based molecular tension sensor	47
2.1.1 Motivation for developing a molecular mechanosensor.....	47
2.1.2 Design of the sensor.....	48
2.2 Application of the sensor	48
2.3 Characterization of the sensor.....	50
2.4 Correlation of EGFR endocytosis with sensor signal.....	54
2.5 Materials and methods	56
2.5.1 Synthesis and characterization of streptavidin-quencher conjugates.....	56
2.5.2 Synthesis and characterization of EGF-PEG conjugates.....	57
2.5.3 Cell culture.....	58

2.5.4 Functionalization of glass substrate biosensors	59
2.5.5 Functionalization of supported lipid bilayers	60
2.5.6 Characterization of the zero-force sensor confirmation.....	61
2.5.7 Fluorescence microscopy.....	62
2.5.8 Image analysis.....	62
2.5.9 Quantitative force maps	63
2.5.10 Determination of EGFR phosphorylation and activation	65
2.5.11 Actin inhibition	65
2.5.12 CLC-eGFP transfection	65
2.6 References.....	66
Appendix 2.....	69

Chapter 3. Integrin-generated forces lead to streptavidin-biotin unbinding in

cellular adhesions	80
3.1 Introduction.....	81
3.1.1 Mechanotransduction in the integrin pathway	81
3.1.2 Methods for studying adhesion forces	81
3.2 Design and synthesis of MTFM sensor	84
3.3 Surface characterization and density calibration	85
3.4 Integrin forces lead to MTFM sensor dissociation	89
3.5 Imaging integrin force dynamics	94
3.6 Generality of integrin-driven biotin dissociation and relationship to focal adhesions.....	96
3.7 Conclusion	97

3.8 Materials and methods	99
3.8.1 Reagents	99
3.8.2 Synthesis of cRGDfK(C)-QSY21-PEG ₂₃ -biotin and cRGDfK(C)-A647- PEG ₂₃ -biotin.....	99
3.8.3 Streptavidin labeling	100
3.8.4 Biotin functionalization of glass substrates	100
3.8.5 Surface density quantification.....	101
3.8.6 Determination of Förster distance between Alexa 647 and QSY21	104
3.8.6.1 Calibration A to obtain the Förster distance of Alexa 647 and QSY21	106
3.8.6.2 Calibration B to obtain the Förster distance of Alexa 647 and QSY21	108
3.8.7 cRGDfK(C)-peptide conjugate immobilization with streptavidin-biotin ...	110
3.8.8 Synthesis of cRGDfK α -thioester, 1	110
3.8.9 Synthesis of fluorescein-PEG ₂₄ -biotin conjugate, 2	110
3.8.10 Conjugation of 1 and 2 to generate cRGDfK-Alexa 647-PEG ₂₄ - fluorescein-biotin, 4	111
3.8.11 Covalent conjugation of cRGDfK(C)-A647-PEG ₂₄ to substrate	111
3.8.12 Cell culture.....	111
3.8.13 Live cell fluorescence microscopy imaging	112
3.8.14 Immunostaining protocols	113
3.9 References.....	113
Appendix 3	120

Chapter 4. Exploring the Mechanotransduction Model of Notch Receptor

Activation	132
4.1 Brief overview of the Notch-Delta system	133
4.1.1 Description of the Notch receptor and its ligands.....	133
4.1.2 Events leading to Notch activation and translocation to the nucleus.....	135
4.2 Discussion of proposed mechanisms of Notch activation	137
4.3 Development of an MTFM probe to study Notch activation.....	138
4.3.1 DNA-based MTFM Notch probes	139
4.3.2 Binding of Dll1-expressing cells to a recombinant Notch 1 extracellular domain.....	141
4.3.3 Differentiating the effects of clustering and density in Dll1-expressing cells binding to NECD surfaces	144
4.4 Testing the ability of Dll1-expressing cells to exert a force on the Notch receptor	146
4.4.1 The streptavidin anchored DNA-based MTFM Notch sensor.....	146
4.4.2 The AuNP anchored DNA-hairpin MTFM sensor	149
4.5 Conclusions.....	155
4.6 Materials and methods	155
4.6.1 Cell Culture.....	155
4.6.2 Insect cell (Sf9) transfection and expression of NECD-mCherry	156
4.6.3 Mammalian cell (HEK293FT) transfection.....	156
4.6.4 Purification and biotinylation of expressed proteins	156
4.6.5 Synthesis of synthetic lipid bilayer surfaces.....	157

4.6.6 Synthesis of streptavidin anchored MTFM surfaces	158
4.6.7 Synthesis of AuNP-DNA MTFM surfaces	159
4.6.8 Microscopy methods	160
4.7 References.....	160
Chapter 5. Summary and future directions	165
5.1 Summary	166
5.2 Future directions	168
5.2.1 Advancing the MTFM probe design.....	168
5.2.2 Clustering and force.....	169
5.3 References.....	170

List of Figures

Figure 1.1 General schematic of genetically encoded molecular tension sensors and immobilized molecular tension sensors	9
Figure 1.2 Plots of fluorescence as a function of force for typical genetically encoded tension sensors (GETS) and immobilized MTFM probes	11
Figure 1.3 Examples of genetically engineered molecular tension sensors.....	15
Figure 1.4 Examples of immobilized molecular tension sensors.....	19
Figure 1.5 Schematic summary of tension values reported using molecular tension-sensing probes	26
Figure 2.1 Design and response of the EGFR tension sensor	49
Figure 2.2 Characterization and quantification of the EGFR tension sensor.....	54
Figure A2.1 Fabrication of glass surface-functionalized force sensors	69
Figure A2.2 Zero-force conformation of the sensor	70
Figure A2.3 Zero-force conformation of the sensor at physiological conditions	71
Figure A2.4 Theoretical plots of PEG ₂₄ and PEG ₇₅ extension and quenching efficiency as a function of applied force	72
Figure A2.5 Specific EGF-EGFR interactions are required to activate the force sensor	73
Figure A2.6 Force Sensor response requires a specific ligand-receptor interaction.....	73
Figure A2.7 Specific EGF-EGFR interactions are required to activate the force sensor: role of apposed ligand.....	74
Figure A2.8 Data analysis of force sensor response	75

Figure A2.9 Cell binding does not induce clustering of sensor	75
Figure A2.10 Binding of EGF antibody to EGF ligand does not trigger the force sensor	76
Figure A2.11 The activity of EGF ligand is independent of linker length	77
Figure A2.12 Flow chart of data analysis for converting quenching efficiency to force maps	78
Figure A2.13 Stability of the sensor as a function of time	79
Figure 3.1 Schematic of the MTFM integrin force sensor.....	84
Figure 3.2 Representative fluorescence images of MTFM sensor surfaces generated with a range of densities and the corresponding mean streptavidin intermolecular distance	86
Figure 3.3 Cells incubated on the biotin-immobilized MTFM sensors exhibit negative signal suggesting streptavidin-biotin dissociation	88
Figure 3.4 Integrin tension imaging in cells incubated on the redesigned MTFM sensor surface.....	95
Figure 3.5 Cells immunostained for focal adhesion markers.....	97
Figure 3.6 Photograph of TLC plate collected after the final stage of purification indicating no free dye present in the final lipid-dye product.....	103
Figure A3.1 Purification and characterization of the cRGDfK(C)-A647-PEG ₂₃ -biotin conjugate.....	120
Figure A3.2 Purification and characterization of the cRGDfK(C)-QSY21-PEG ₂₃ -biotin conjugate.....	121
Figure A3.3 Scheme depicting the covalent biotin-functionalization of glass	

surfaces	122
Figure A3.4 Determination of streptavidin-biotin dissociation rate	122
Figure A3.5 Force sensor conjugates are immobilized through biotin-specific Interactions.....	123
Figure A3.6 Quantitative fluorescence calibration to measure surface density of streptavidin and peptide mechanophore.....	124
Figure A3.7 Calibration A to obtain the Förster distance of Alexa 647 and QSY21	124
Figure A3.8 Calibration B to obtain the Förster distance of Alexa 647 and QSY21.....	125
Figure A3.9 Areas of decreased MTFM fluorescence colocalize with focal adhesion proteins.....	125
Figure A3.10 Conjugation of cRGDfK α -thioester with fluorescein-PEG ₂₄ -biotin conjugate and coupling of Alexa 647 as the acceptor fluorophore.....	126
Figure A3.11 Purification and characterization of the cRGDfK-Alexa647-PEG ₂₄ -fluorescein-biotin conjugate.....	127
Figure A3.12 Biotin dissociation requires myosin and f-actin	128
Figure A3.13 Cell dissociation does not reverse negative MTFM signal.....	129
Figure A3.14 When two bonds are found in a series and subjected to an external mechanical load, it is expected that the weaker bond will be more likely to dissociate.....	130
Figure A3.15 Global cell response to integrin MTFM sensor surface for 5 h.....	131
Figure 4.1 Notch receptors and ligands found in <i>D. melanogaster</i> , <i>H. sapiens</i> , and <i>C. elegans</i>	133
Figure 4.2 Structural aspects of the Notch pathway	135

Figure 4.3 Series of events leading to Notch activation and translocation to the nucleus	137
Figure 4.4 Design of two MTFM probes used to explore Notch mechanotransduction by ligand expressing cells	140
Figure 4.5 Binding of Dll1-expressing cells to recombinant NECD-mCherry expressed by Sf9 cells.....	142
Figure 4.6 Binding of Dll1-mCherry expressing cells to recombinant NECD-Fc chimera expressed by mammalian cells.....	143
Figure 4.7 Ligand density affects the degree of binding to NECD coated lipid surfaces	145
Figure 4.8 Unlabeled Dll1-expressing cells on streptavidin anchored MTFM surfaces exhibit positive fluorescence signal	147
Figure 4.9 Non-specific binding of NECD to streptavidin anchored MTFM surfaces...	148
Figure 4.10 Bleedthrough occurs from Dll1-mCherry into the sensor channel.....	150
Figure 4.11 Updated optical configuration for correction of spectral bleedthrough	150
Figure 4.12 Dll1-mCherry bound to NECD-eGFP on AuNP MTFM surface exhibits positive tension signal.....	153
Figure 4.13 Unlabeled Dll1 expressing cells appear to remove MTFM probe from the surface.....	154

List of Tables

Table 1.1 Comparison of molecular force sensors.....	13
Table 4.1 Percentage of spectral bleedthrough observed when imaging single fluorophore functionalized surfaces.....	151

Chapter 1: Mechanotransduction and Methods to Measure Cellular Tension

Adapted from Jurchenko, C.; Salaita, K.S. Lighting up the force: Investigating mechanisms of mechanotransduction using fluorescent tension probes. *Mol. Cell. Biol.* **2015**, *35*, 2570-2582, used with permission.

1.1 The role of molecular mechanotransduction in cell biology and biochemistry

1.1.1 A brief history of measuring molecular tension in live cells

Multicellular organisms depend on the ability of individual cells to communicate with each other and sense their external environment, including the extracellular matrix (ECM). Studies of cellular communication and signaling have historically focused on chemical pathways. However, the role of physical cues exchanged among cells and through the ECM is increasingly being recognized as an important mediator of cellular sensing and communication. For example, the stiffness of the ECM has profound impacts on cell morphology and cytoskeletal structure¹ and on stem cell differentiation^{2, 3} and is associated with tumor formation^{4, 5}. Sensitivity to physical cues within the microenvironment demonstrates that cells are able to convert mechanical signals into biochemical signals. Conversely, cells remodel their surrounding ECM in response to specific chemical cues. For example, secretion of TGF- β or the absence of TNF- α leads to increased fibrosis and increased stiffness of the ECM^{6, 7}. Therefore, cells transduce chemical signals into physical signals that trigger changes in nearby cells. Mechanotransduction is a dynamic process that plays a critical role in the survival of multicellular organisms.

It has long been known that stretching of nerve cells leads to cellular depolarization⁸. The mechanism, however, by which this mechanical stimulation is transduced into a chemical signal was not confirmed until Guharay and Sachs⁹ reported the presence of mechanosensing ion channels in muscle cells. These ion channels are a critical feature of specialized force-sensing cells, such as hair cells in the inner ear¹⁰. In the 30 years since this discovery, many additional mechanotransduction pathways have

been identified. Typically, the mechanisms employed involve force-induced conformational changes in a protein that trigger additional protein-protein interactions. For example, the mechanical unfolding of fibronectin, an ECM protein, has been shown to expose cryptic binding sites that allow fibronectin crosslinking^{11, 12}, thus providing a method for cells to mechanically manipulate and remodel the structure of their surrounding ECM. An additional example is talin, an adaptor protein in focal adhesions (FAs), which has been reported to reveal additional sites for vinculin binding in response to mechanical strain¹³. The increase in vinculin binding under strain results in reinforcement of the attachment of the FA to the cytoskeleton^{13, 14}. Another FA adaptor protein, p130Cas, exposes tyrosine phosphorylation sites for Src family kinases when stretched, suggesting an additional force-sensitive aspect of FA signaling and regulation¹⁵. Gaining a molecular-level understanding of these and other mechanotransduction processes is of fundamental importance to cell biology.

Early topics in the field of cellular mechanotransduction, some of which are still being actively investigated today, include the study of cellular adhesion forces, stiffness characteristics of intact cells, cellular stiffening and chemical responses to applied forces, and the viscoelastic properties of cells. Methods used to conduct these studies include atomic force microscopy (AFM)¹⁶⁻²⁰, magnetic twisting cytometry²¹⁻²⁵, particle tracking rheology²⁶⁻³¹, and laser ablation of cytoskeletal structures³²⁻³⁶. Given the interdisciplinary nature of mechanotransduction studies, advances in the field have been heavily dependent on technique development. Specifically, methods to measure and apply forces have been central to defining the types of biological questions that could be pursued.

Due to tremendous advances in single-molecule techniques, there has been a

recent trend of investigating mechanotransduction events on a molecular scale. In fact, a vast number of quantitative molecular tension measurements have been obtained from single-molecule techniques, such as AFM^{19, 37-43}, optical and magnetic tweezers^{13, 14, 44-51}, and biomembrane force probes⁵²⁻⁵⁵. Primarily, these measurements are performed *in vitro* and typically require that the experimenter apply a force to a protein complex. When researchers are able to perform these experiments with live cells, they interrogate receptors on the membrane but not cytosolic proteins. Thus, questions remain about how or whether many mechanotransduction events occur *in vivo* and whether force-induced changes are used by the cell to regulate function. Live-cell experiments, which measure tension within the cell or applied by the cell, have the potential to inform our understanding of chemomechanical coupling and are particularly relevant for trying to understand the formation of protein assemblies and how force is propagated through these assemblies to initiate biochemical responses in the cell.

Currently, the field of mechanotransduction is undergoing rapid growth due, in part, to the availability of new fluorescence-based molecular tension-sensing probes that report forces for discrete, site-specifically labeled molecules. These sensors are filling the need for molecularly specific, quantitative force imaging methods. The advent of these probes is allowing the research community to explore molecular tension events and to correlate these events with biochemical processes in live cells. The following chapter gives a brief overview of the history of measuring cellular forces and summarizes the state of the art in performing such measurements and how it is transforming the field of mechanotransduction.

1.1.2 Focal adhesions as a model mechanotransduction system

Physical sensing of the microenvironment and remodeling of the ECM are mediated by protein assemblies that form at the cell-ECM junction. The primary proteins linking the cell to the ECM are the integrin receptors, which are responsible for directly binding and bridging the intracellular cytoskeleton with the ECM⁵⁶. Once ligand bound, the integrin receptors typically cluster, recruit intracellular adaptor and signaling proteins, and form FAs. Given that integrins experience significant mechanical load and also display differential ligand affinities as a function of matrix stiffness, integrin-based FAs have quickly become the prototypical model for studying mechanotransduction.

Many methods have been applied to study the potential role of force in integrin-ECM binding and subsequent FA formation. For example, Jiang et al.⁵⁷, using a laser-trapped bead, observed a 2 pN slip bond between the ECM protein fibronectin (Fn) and the integrin $\alpha_v\beta_3$ /talin 1/F-actin complex. In this work, the 2 pN bond was hypothesized to represent the force at which the connection to the cytoskeleton is disrupted. Additional work by Roca-Cusachs et al.⁵⁸ used magnetic tweezers to explore how Fn clustering modulates cell adhesion strength. They found that cells bound to Fn pentamers could withstand ~6-fold greater forces before rupture of the bond than Fn monomers. Furthermore, $\alpha_5\beta_1$ integrins were primarily responsible for maintaining adhesion strength, while $\alpha_v\beta_3$ integrins responded to mechanical stimulation by inducing cellular stiffening, likely through recruitment of more integrins, adaptor proteins, or cytoskeletal attachments to reinforce adhesion sites. They also noted that integrin clustering is required for binding of talin to cytoplasmic integrin tails.

Additional methods for observing and analyzing cellular traction forces include traction force microscopy (TFM)⁵⁹⁻⁶³ and micropillar array detectors (mPADs)⁶⁴⁻⁷². TFM

and mPADS are designed to detect cellular forces applied to the ECM by observing deformation of the underlying substrate. In the standard TFM experiment, cells are cultured on hydrogels containing fluorescently labeled beads, and cell traction force measurements are based on measuring bead displacement while accounting for the elasticity (or resistance) of the substrate. When mPADs are used, the gel is patterned into micrometer-sized polydimethylsiloxane (PDMS) posts onto which cells are cultured. Deformation, or bending, of the posts is measured optically to infer lateral forces. These methods have greatly contributed to the field of mechanotransduction. High-resolution TFM experiments have revealed that FAs contain both stable, static states and dynamic, sampling states that allow the cell to sense its physical environment⁷³. TFM studies, coupled with small interfering RNA (siRNA) knockdown, by Prager-Khoutorsky et al.⁷⁴ identified several protein tyrosine kinases that appear to play a role in force application through FAs. However, estimating single-molecule forces using these methods requires assessing the local density of receptors and averaging of substrate stress across micrometer-sized regions. Therefore, while these methods are valuable, they are not well suited to the study of molecular-scale forces.

Determining polymer deformation using fluorescence resonance energy transfer (FRET), rather than bead or pillar displacement is, in principle, capable of tracking nanometer scale deformations, thus potentially offering greater sensitivity. FRET is a mechanism of nonradiative energy transfer from one fluorophore (donor) to another fluorophore (acceptor). The efficiency of energy transfer is dependent on the donor-acceptor distance and the alignment of the fluorophore transition dipole moments⁷⁵. Pairs of fluorophores, which have spectral overlap between the donor emission and the

acceptor absorbance, have a characteristic distance (Förster distance, or R_0) at which energy transfer efficiency is equal to 50%. R_0 values are typically in the range of 4 to 7 nm. Due to nanometer distance dependence, FRET is routinely used to quantify conformational dynamics in single molecules⁷⁶⁻⁸⁰ and has been used in several biosensors designed to detect activated forms of specific proteins, such as Src kinase⁸¹⁻⁸⁴, focal adhesion kinase (FAK)⁸⁵, and the GTPases Rac^{84, 86} and RhoA^{87, 88}. These types of biosensors were the original inspiration for many of the newly emerging molecular tension-sensing methods that are discussed in the following section. Initial approaches using FRET to determine Fn network deformation used random dye labeling of Fn. Therefore, the signal-force response function of the labeled Fn could not be calibrated to report specific forces. Thus, while these measurements were highly sensitive and could be obtained in real time, the methods generated qualitative tension maps rather than quantitative and calibrated images. For example, Baneyx et al.⁸⁹ and Smith et al.⁹⁰ labeled Fn by reacting the free cysteine residues of FnIII7 and FnIII15 with acceptor fluorophore followed by labeling of free amines with the donor dye⁸⁹. Alternatively, labeling could be achieved by coupling a 1:1 ratio of donor and acceptor fluorophore in a one-pot reaction⁹⁰. In this way, FRET was used to report on the deformation and extension of Fn fibers. As a proof of concept, fibroblasts were cultured with the Fn conjugates, and cell-driven changes in FRET were monitored. Importantly, FRET-based detection of Fn deformation was also applied to fibroblasts cultured in three-dimensional (3D) matrices⁹¹, which more accurately represent the native cellular environment than 2D substrates. An alternative FRET-based method involves fluorescent labeling of a population of adhesion ligands with donor or acceptor molecules and embedding these in hydrogels. Cells

cultured on the surface caused the distance between donor and acceptor chromophores to change, thus providing a FRET readout that correlated to cell-applied tension⁹². While useful in providing relative FRET values, a challenge of these methods pertains to the cross-linked nature of the matrix. This results in forces being distributed across the polymer network, thus limiting the ability to quantify precise forces associated with individual adhesion receptors during cell signaling events.

Although many studies of FA mechanotransduction have been reported, there are still many questions remaining about the cellular mechanisms of mechanosensing in adhesions. For example, how does clustering of integrin receptors affect the ability of cells to apply tension? What is the loading rate of force applied by the cell and how does this affect tension? What is the amount of tension applied across an individual integrin-ECM bond? An additional question concerns the nature of the integrin-ECM bond itself. Certain integrins ($\alpha_5\beta_1$) have been shown to exhibit catch-bond behavior, in which a reduction in the receptor-ligand dissociation rate is observed in response to moderate levels of force applied across the bond^{93, 94}. Catch-bond behavior is in contrast to the vast majority of bonds (slip bonds), which accelerate the rate of dissociation upon application of a mechanical load^{95, 96}. It is not clear, however, if other integrin receptors also display a catch-bond character. Examples of proteins exhibiting catch-bond behavior include P-selectin and its ligand⁹⁷ and the $\alpha_5\beta_1$ integrin receptors bound to fibronectin⁹⁴. Recently, the E-cadherin/ β -catenin/ α E-catenin complex has also been shown to have more stable binding to F actin when ~ 5 to 10 pN of tension is applied to the bond⁵¹. The majority of studied catch bonds are observed in the range of ~ 5 to 20 pN per receptor-ligand pair. Given the limitations of TFM, it is not possible to address these questions at this time.

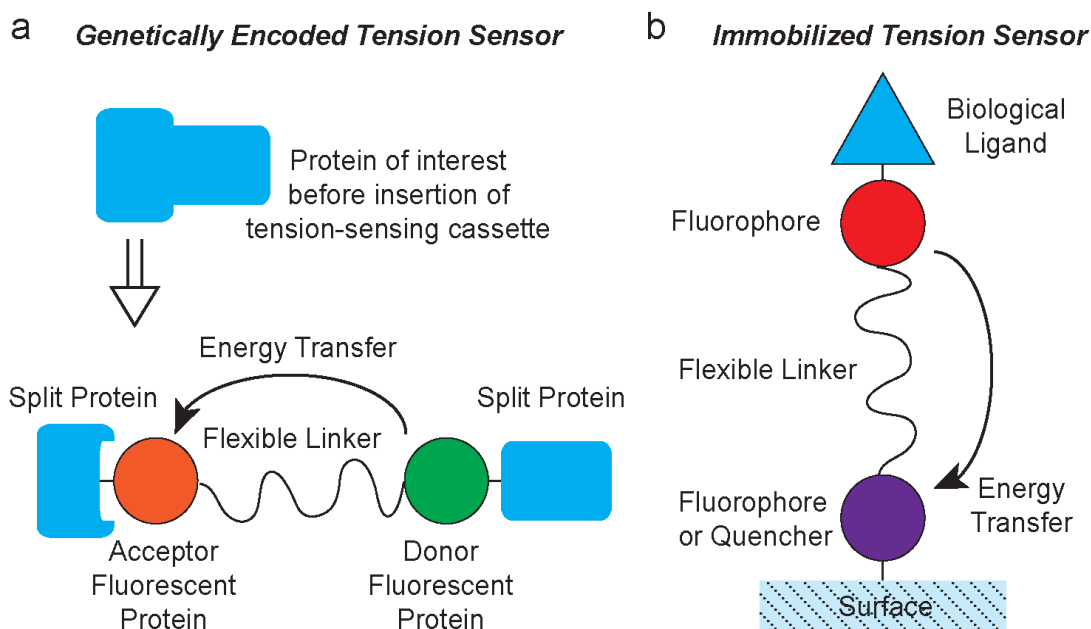


Figure 1.1 General schematic of genetically encoded molecular tension sensors (a) and immobilized molecular tension sensors (b). Genetically encoded tension sensors require modification of a protein to introduce a fluorescent tension-sensing module. Immobilized tension sensors are directly grafted onto cell culture substrates. Both designs employ fluorescence energy transfer to report on forces that extend a flexible linker.

The inherent elasticity of TFM substrates or micropillar array substrates dictates the sensitivity of these approaches to quantify cell traction forces. However, this introduces some challenges, because the substrate elasticity also influences cell biology and cell adhesion. Thus, the measurement itself can be confounding. Another limitation of TFM and mPADS is related to the spatial resolution, which is typically on the order of a few micrometers to $\sim 0.7 \mu\text{m}^{63,73}$. This is dictated by the density of the fiducial markers in TFM or the density and size of PDMS pillars used in mPADS⁶⁶. Finally, TFM and mPADS are sensitive to forces in the nanonewton range, which are significantly greater than the forces experienced by nascent adhesions and certainly greater than the forces experienced by individual molecules. These limitations have motivated the development

of molecular tension probes, which are described in the following section.

1.2 Emerging methods for measuring molecular tension

Recently, new methods have been developed that address the need for measuring live-cell molecular-scale forces. These molecular tension sensors contain two basic components. The first component is a pair of chromophores that act as a spectroscopic ruler through an energy transfer mechanism, such as FRET. The second component is a flexible linker that connects the two chromophores. For the purpose of this discussion, we have divided the molecular tension sensors into two categories, those that are genetically engineered and expressed within living cells (**Figure 1.1a**) and those that are anchored to a surface (**Figure 1.1b**), to probe receptor forces at the interface between living cells and their external ligands. In the case of genetically encoded tension sensors (GETS), the fluorophore and linker are inserted into a protein of interest inside the cell. In contrast, immobilized tension sensors are anchored to a substrate and present a ligand specific to a cell surface receptor (**Figure 1.1**). The choice of fluorescent donor and acceptor, as well as the choice of linker, impacts the dynamic range and the sensitivity of the sensor by dictating the magnitude of linker extension that can be measured (thus the range of detectable forces) and the amount of fluorescent signal in the absence of force.

Most molecular tension probes utilize FRET, which requires spectrally matched fluorophores or fluorophore-quencher pairs. Fluorophores may be organic dyes or fluorescent proteins. Due to the distance dependence of FRET, placement of a flexible linker between the donor and acceptor allows fluorescence imaging to be used to detect nanometer changes in extension of the linker under tension. The Förster distance (R_0) of each FRET pair is critical to determining the range of distances at which the fluorophores

can participate in energy transfer and therefore often limits the range of extensions and forces that can be explored.

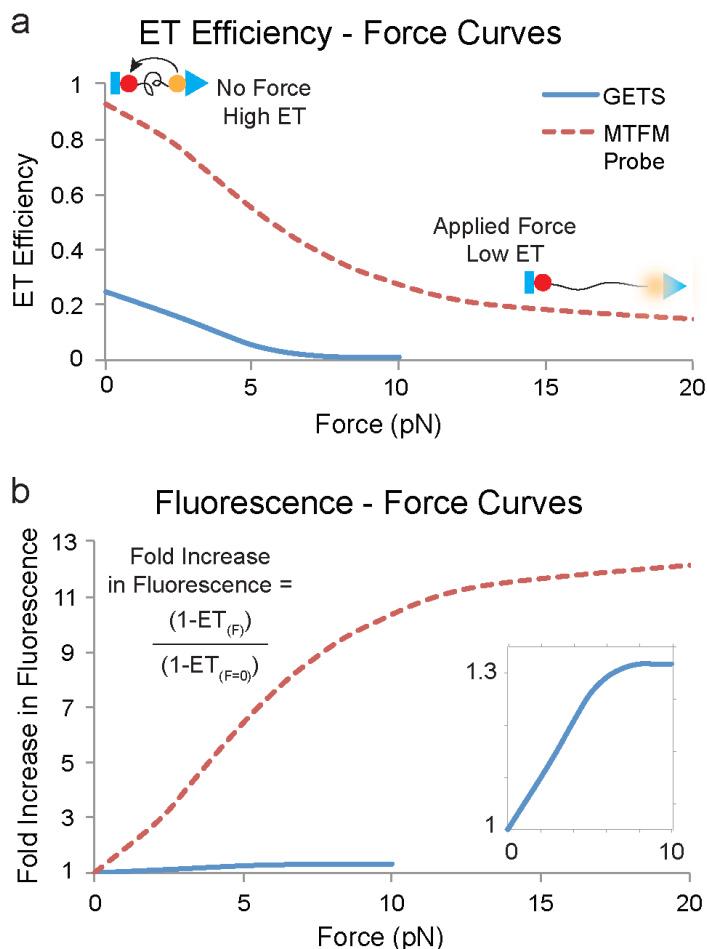


Figure 1.2 Plots of fluorescence as a function of force for typical genetically encoded tension sensors (GETS) and immobilized MTFM probes. (a) Plot of energy transfer (ET) efficiency as a function of applied force in units of pN. ET efficiency is dependent on the distance between donor and acceptor to the sixth power. (b) Plot of the fold increase in fluorescence as a function of force (in piconewtons). The fold increase in signal is normalized to the fluorescence signal when force is 0 pN. Fold increase in fluorescence is defined as $(1-ET_F)/(1-ET_{F=0})$, where ET_F is the energy transfer efficiency as a function of force and $ET_{F=0}$ is the energy transfer efficiency in the absence of force. Data for the GETS signal were estimated from the work of Grashoff et al.⁹⁸, while the data for the MTFM probes were obtained from the work of Jurchenko et al.⁹⁹.

The relationship between force and fluorescence can be assessed through experimental calibration or by using well-established models of linker behavior under

force. Once a tension sensor has been shown to have a predictable fluorescence-force curve (**Figure 1.2**), quantitative force measurements can be obtained in live cells. It is important to note that the molecular tension sensors start with some degree of donor-acceptor separation even in the absence of force, which leads to energy transfer (ET) efficiencies that are less than 100% at a force of 0 pN. The amount of fluorescent signal in the absence of force is a critical parameter, since it influences the dynamic range and sensitivity of the probe. For example, if a tension sensor has an ET efficiency of 50% in the absence of force, then the maximum increase in donor fluorescence is 2-fold over the resting value of donor emission. In contrast, a probe with 95% ET efficiency at rest can display a maximum increase in donor signal of 20-fold, which is much more desirable when live cells that exhibit auto-fluorescence are being imaged. Given the intrinsic dimensions of fluorescent proteins, the typical ET efficiencies at rest for GETS are lower than that of probes employing organic dyes. To illustrate this point, **Figure 1.2a** shows a plot of the ET efficiency as force is applied to either a GETS (solid blue line)⁹⁸ or an immobilized molecular tension fluorescence microscopy (MTFM) probe (dotted red line)⁹⁹. A low ET efficiency at zero force indicates a resting conformation in which the donor and acceptor are significantly separated. The effect of low ET at the resting state is shown in **Figure 1.2a**, where the maximum donor fluorescent signal for the GETS is ~1.3-fold over the starting fluorescence intensity. The representative immobilized probe, which utilizes organic dye donor-acceptor pairs rather than fluorescent proteins, has a resting ET efficiency of ~0.9. Therefore, the immobilized probe exhibits a maximum signal approximately 10-fold greater than the fluorescence intensity at zero force. Also note that, due to the nonlinear character of the fluorescence-force curves, the sensors

become less sensitive to changes in force at ~ 12 pN for the representative immobilized probe and ~ 6 pN for the representative GETS.

TABLE 1.1 Comparison of Molecular Force Sensors^a

Type and sensor	Spectroscopic Ruler	Linker	Max S/B ^b	Force Dynamic Range (pN)	Protein(s) Targeted	Reference(s)
GETS						
stFRET	FRET	α -helical peptide	1.8-fold	$\sim 5-7^c$	Spectrin, α -actinin, filamin A, collagen-19	(103,104)
sstFRET	FRET	Spectrin repeat	2-fold	$\sim 5-7^c$	α -actinin	(105-107)
cpstFRET	FRET	Poly(G) peptide	4-fold	$\sim 5-10^c$	Spectrin	(108)
PriSSM	PRIM	AS(GGS) ₉	2-fold	N.d.	Myosin II, Vinculin, E-cadherin, VE-cadherin, PECAM, β -spectrin,	(109,111)
TSMoD	FRET	(GPGGA) ₈	1.3-fold	$\sim 1-6^c$	MUC1	(35, 98, 112-116)
Immobilized						
MTFM-FRET	FRET	PEG ₂₄	10-fold	$\sim 1-20^d$	EGFR, integrins	(99,117)
MTFM-NSET	NSET	PEG ₈₀	10-fold	$\sim 1-25^d$	Integrins	(126,127)
MTFM-DNA	FRET	DNA hairpin	30-fold	$\sim 5-16^c$	Integrins	(129)
TP	FRET	DNA hairpin	~ 30 -fold	$\sim 6-17^c$	Integrins	(130)
MTS	FRET	(GPGGA) ₈	3-fold	$\sim 1-7^d$	Integrins	(118,135)
TGT	NA	DNA	NA	$\sim 12-56^d$	Integrins, Notch/Delta	(131)

^a ND, not determined; NA, not applicable.

^b Maximum signal/background ratio (S/B) is defined as $(1 - ET_{F_{\max}})/(1 - ET_{F=0})$, where $ET_{F_{\max}}$ is the energy transfer efficiency at full linker extension and $ET_{F=0}$ is the energy transfer efficiency in the absence of force.

^c The sensor response was experimentally calibrated.

^d Sensor response was determined through calculation.

The choice of linker between the two chromophores also plays an important role in defining the dynamic range of the sensor by tuning the “spring constant” of the probe. Each type of linker has a unique force-extension response function, and this should be well matched to the linear range of ET distances for the donor-acceptor pair. The linker may behave as an entropic spring, as is the case for polyethylene glycol (PEG) polymers, or it may contain some degree of secondary structure, such as with some peptides or proteins. An additional example linker is a DNA hairpin. This type of linker behaves

more like a digital switch, abruptly dehybridizing and changing extension in response to a threshold magnitude of force. A summary of reported molecular tension sensors is given in **Table 1.1**.

1.2.1 Genetically encoded tension sensors

Genetically encoded molecular tension sensors (GETS) are engineered proteins in which a tension sensing module, or cassette, has been genetically inserted into a protein of interest. This class of probes contains two fluorescent proteins (a donor and an acceptor) and a flexible protein-based linker connecting the fluorophores (**Figure 1.1a**). As with all of the molecular tension sensors, when the tension-sensing cassettes are being designed, concerns such as matching the R_0 of the donor-acceptor pair with the extension range of the linker must be taken into account. Then, a library (or multiple libraries with different cassette design variants) of protein mutants is created and tested to assess the best location within the protein to insert the cassette. The ideal location would be a region of the protein that maintains a relatively high ET efficiency in the absence of force and experiences forces that extend the linker during cell activity. After the site of module insertion is chosen, DNA that codes for the cellular expression of the engineered protein must be transfected into living cells, and appropriate protein expression, localization, and function must be verified. This is necessary to ensure that insertion of the ~60 kDa tension sensing module does not affect, or inhibit, protein function. Several reviews have recently been published that further describe a thorough list of the control experiments and constructs that are recommended to verify that the GETS is functioning properly and not interfering with cell or protein function¹⁰⁰⁻¹⁰². Once a mutant is identified that preserves biological function and contains an appropriately placed sensor, tension across

the protein can be observed in living cells using fluorescence imaging. These sensors, therefore, take time to design and engineer, but they are very simple to adopt and use. The FRET measurement requires appropriate bleed-through and cross talk corrections, but image acquisition is relatively straightforward. Another benefit of these biologically encoded sensors is that the fluorophores are more likely to be present at a 1:1 ratio, which improves the accuracy of the FRET measurement. Since these sensors are genetically encoded, the use of fluorophores and linkers is limited to protein based constructs. The R_0 of most fluorescent proteins is between 4 and 6 nm; therefore, the effective spring constant of the linker becomes the primary element available to the researcher to control the dynamic range of the sensor. This makes the choice of linker critical to the effectiveness of the sensor and requires that the dynamic range match the range of forces that are expected in the system under investigation.

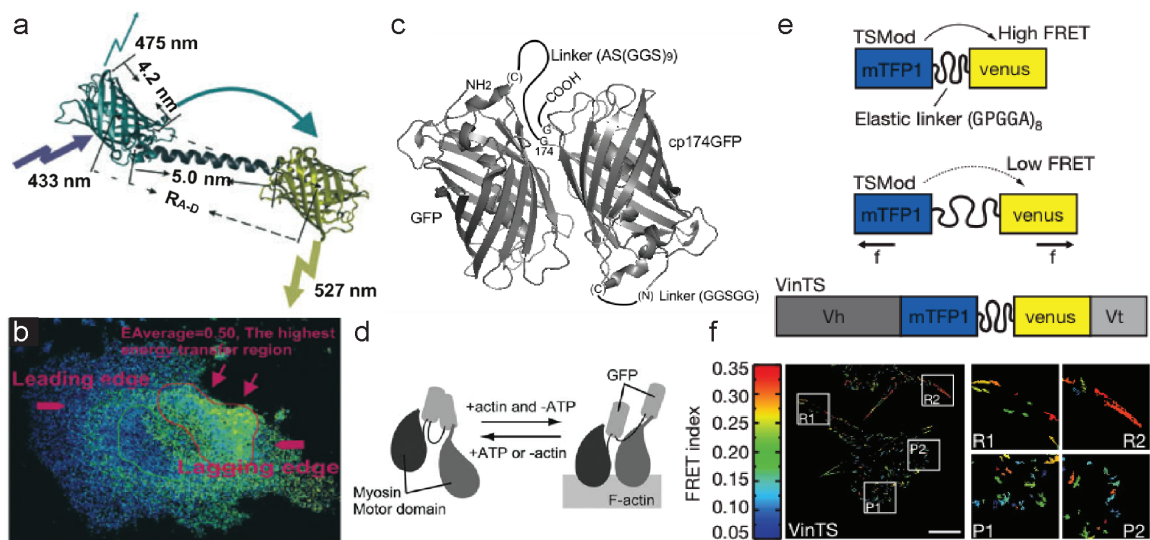


Figure 1.3 Examples of genetically engineered molecular tension sensors. (a) FRET cassette (stFRET) designed by Meng et al.¹⁰³ (b) Data from 3T3 cells containing the stFRET showing decreased tension in α -actinin at the lagging edge of the cell. (Images in panels a and b are reprinted from reference 103 with permission of the publisher.) (c) A PRIM-based strain sensor module (PriSSM) reported by Iwai and Uyeda¹⁰⁴. (d) Schematic of the incorporation of PriSSM into myosin. (Images in panels c and d are

reprinted from reference 109 with permission of the publisher.) (e) Tension sensor module (TSMoD) designed for insertion into vinculin by Grashoff et al.⁹⁸. (f) Cells containing the TSMoD inserted into vinculin reveal higher tension (low FRET index) in regions of cell protrusion (P1 and P2) compared to regions where the cell retracts (R1 and R2). (Images in panels e and f are reprinted from reference 98 with permission of the publisher.)

In 2008, Meng and coworkers reported one of the first biologically engineered tension sensors¹⁰³. This sensor, which was termed a stretch-sensitive FRET cassette (stFRET), consisted of two fluorescent proteins, Cerulean and Venus, joined by a 5 nm protein α -helix (**Figure 1.3a**). As a proof of concept, the stFRET was inserted into several different proteins (spectrin, α -actinin, and filamin A) and expressed in cultured cells¹⁰³. Insertion of the stFRET into α -actinin revealed a decrease in tension at the lagging edge of 3T3 fibroblasts (**Figure 1.3a**). Furthermore, by inserting the sensor into collagen, Meng et al. were able to express it in a living host, *Caenorhabditis elegans*^{103, 105}. The initial work, however, did not include a calibration of the sensor; thus, no quantification of the observed forces was possible. In later work, the sensitivity range of the stFRET was determined to be 5 to 7 pN by using DNA hybridization to generate a force and extend the sensor^{105, 106}. FRET measurements of the stFRET probe indicate that the probe is slightly extended when conjugated to single stranded DNA (ssDNA) (prior to DNA hybridization). This suggests that the force dynamic range of the stFRET is slightly larger than the 5 to 7 pN range and that the probe is more likely analog than digital. However, unambiguous calibration of this probe needs to be performed using a single-force spectroscopy experiment in order to determine its response function. The sensor was also improved (and renamed the spectrin repeat stretch-sensitive FRET sensor [sstFRET]) by substituting a spectrin repeat for the α -helix initially used as the linker¹⁰⁶. This updated sensor was then used to observe mechanical behavior in α -actinin under

shear stress¹⁰⁷ and during FA growth¹⁰⁸. A further modification of the sensor utilized circular permutants of Cerulean and Venus to create a probe (termed cpstFRET) in which the fluorophores are closely linked and the tension signal is due to changes in the angle between the two proteins¹⁰⁹.

Another genetically engineered strain sensor was reported by Iwai and Uyeda¹⁰⁴. This sensor, named the proximity imaging (PRIM)-based strain sensor module (PriSSM), is based on proximity imaging of green fluorescent protein (GFP) (**Figure 1.3c**). PRIM compares the ratio of emission at 510 nm when GFP is excited at 395 and 475 nm¹¹⁰. When two GFPs dimerize, this ratio shifts, and thus, the change in proximity can be monitored. In order to generate an effective sensor, Iwai and Uyeda made a GFP circular permutant, which created new termini in one of the GFP monomers. This allowed the linker to connect the two monomers with minimal steric inhibition caused by their natural antiparallel dimerization. The linker chosen for PriSSM was a flexible 29 amino acid peptide linker. By incorporating the PriSSM into myosin II, researchers were able to observe myosin interaction with F-actin (**Figure 1.3d**)^{104, 111}. These experiments allowed the localization of myosin directly interacting with F-actin to be determined in live cells.

In 2010, Grashoff et al. designed a tension sensor module (TSMoD) which contained mTFP1 and Venus (A206K) as the fluorescent proteins and used a 40-amino-acid sequence derived from spider silk protein as the flexible linker (**Figure 1.3e**)⁹⁸. The dynamic range of the TSMoD was calibrated using single-molecule fluorescence imaging coupled with optical tweezers, which represented an important step in the field. In order to facilitate the single-molecule measurement, the ends of the linker were labeled with the organic dyes Cy3 and Cy5, and by using optical tweezers, this construct was stretched

and the resulting fluorescence changes recorded. TSMOD was then incorporated into vinculin to observe tension during cell migration, revealing an increase in tension across vinculin within FAs at the protruding edges of the cell (**Figure 1.3f**). Vinculin was reported to experience an average force of 2.5 pN.

Currently, the TSMOD probe is widely being adapted by many different research groups to test forces in a range of proteins and cellular signaling pathways. For example, it is now being used to explore the role of mechanical force across proteins in cellular systems that include E-cadherin^{112, 113}, VE-cadherin, and PECAM¹¹⁴. Additionally, incorporation of the TSMOD into β -spectrin in *C. elegans* allowed researchers to explore the role of β -spectrin in touch receptors in living organisms¹¹⁵. It has also been used in conjunction with another method to study cellular traction forces, laser ablation of cytoskeletal stress fibers³⁵, and was recently employed as a compression sensor to study the effect of the glycocalyx on integrin activation and FA formation in cancer cells¹¹⁶.

Although the use of TSMOD in cell mechanotransduction studies is expanding, certain limitations should be noted. The low sensitivity of the GETS presents some challenges. For example, when data from fluorescence images are analyzed, it is critical to differentiate between applied tension and other factors that may also contribute to a low ET efficiency, such as low sensor incorporation or high autofluorescence from the cell. To ensure that the observed data are quantitative, a method such as fluorescence lifetime imaging microscopy (FLIM) or normalization of fluorescence to either the donor or acceptor fluorophore emission needs to be applied. Furthermore, even under ideal imaging conditions, the GETS that have thus far been reported are limited to the detection of forces within the range of 1 to 7 pN^{98, 105}. Another limitation pertains to the

representative data for a MTFM probe designed to detect forces associated with endocytosis of the EGF ligand by its receptor. (Reprinted from reference 117 with permission of the publisher.) (b) Immobilized tension sensor that was modeled on the genetically encoded TMod. The spider silk protein domain (GPGGA)₈ was used as the linker, and Alexa Fluor 546 and 647 were used as the donor and acceptor. (Left) Location of FAs (circled in red), as indicated by fluorescent labeling of paxillin. (Right) Regions of tension (lower FRET index) that colocalize with FAs. (Reprinted from reference 118 with permission of the publisher.) (c) AuNP-based MTFM sensor that utilizes NSET as a spectroscopic ruler. This probe primarily reported the tension observed between $\alpha_v\beta_3$ integrins and cRGD. (Reprinted from reference 126 with permission of the publisher.) (d) Schematic and representative data of DNA-based MTFM probes that display a digital output. When sufficient force is applied (4.7 pN), the DNA hairpin is unfolded, leading to separation of the fluorophore from the quencher and an increase in fluorescence of ~20- to 30-fold. Cells expressing β_3 -integrin-GFP were cultured on the DNA-MTFM probes. Images on the right show two different time points, correlating to the arrival of β_3 integrins (black line scan) followed by the appearance of tension (green line scan). (Reprinted from reference 129 with permission of the publisher.)

The first immobilized molecular tension sensor specific to cell surface receptors was reported by our group in 2012 and revealed the force exerted during endocytosis of the EGF receptor after ligand binding (**Figure 1.4a**)¹¹⁷. This tension-sensing method was termed molecular tension fluorescence microscopy (MTFM)⁹⁹. The original MTFM sensor consisted of a synthetic fluorophore-quencher pair connected by a PEG linker anchored to the surface of a glass slide through streptavidin-biotin binding. Using a nonradiative chromophore as the FRET acceptor allows the sensor output to be read as a simple “turn on” signal without the need to perform corrections for spectral bleed-through or cross talk. Additionally, since only one fluorescence channel is needed for force imaging, it leaves 2 or 3 channels available for the imaging of downstream cellular signaling in response to tension. For example, FRET biosensors such as FAK⁸⁵ and Src biosensors^{81, 82} and ratiometric Ca²⁺ indicators can be combined with MTFM probes. The dynamic range of the MTFM sensor was calculated by applying the extended worm-like chain model to the extension of the PEG polymer. This model allows the fluorescence

signal and FRET efficiency to be converted into an estimated per ligand force value. These values, however, represent the minimum average force applied per receptor. This is due to the ensemble nature of the FRET measurements and is true for all of the molecular tension sensors, including those that are genetically incorporated. By using extremely low densities of immobilized sensors (as was shown by Morimatsu et al.¹¹⁸), single-molecule FRET measurements can provide the absolute extension of single molecules, which eliminates the ensemble nature of the measurements. However, single-molecule measurements introduce other challenges due to the need for O₂ scavengers and the scarcity of reporters.

The MTFM tension probe was also adapted for studying FA maturation by targeting integrin receptors via a cyclic RGD (cRGD) ligand⁹⁹. However, in these experiments, it was found that the forces applied through integrin receptors were sufficient to dissociate the streptavidin-biotin bond. Mechanical streptavidin-biotin dissociation was unexpected, because the reported K_d (affinity) for streptavidin-biotin is at least 10^6 times greater than that of the integrin-ligand bond¹¹⁹⁻¹²¹. In addition, dissociation rates (k_{off}) predict that the integrin receptors ($k_{\text{off}} \sim 0.072 \text{ s}^{-1}$ at 37° C)¹²² would dissociate before streptavidin-biotin dissociation ($k_{\text{off}} \sim 10^{-5} \text{ s}^{-1}$ at 37° C)^{99, 123, 124}. Streptavidin-biotin dissociation within a 45 min time window suggests that integrin receptors apply forces to ECM ligands that exceed 20 pN. This is because a constant force of 20 pN is required to dissociate streptavidin-biotin within the 45 min of cell adhesion¹²⁵. That said, the biological loading rate is unknown, and how it impacts the bond rupture force may be significant. In contrast to these results, researchers using an alternate design of an immobilized sensor found that integrin receptors apply 1 to 5 pN of

tension to their ligand¹¹⁸. These experiments utilized the spider silk protein linker developed for the TSMOD, which has a dynamic range of 1 to 6 pN. The construct was anchored to a surface via biotin-NeutrAvidin binding (**Figure 1.4b**), and the authors¹¹⁸ claimed that this bond was stable against integrin forces. The use of a linear RGD ligand in these experiments could affect the degree of force applied by the receptors, since it is known that the binding constant for integrins with certain cyclic RGD peptides is significantly greater than that for the linear RGD form^{120, 121}. Nonetheless, it is important to note that the attachment method of the anchored sensors must be sufficiently stable to withstand the biological forces being applied by the system.

An alternate approach to address the need for robust immobilization chemistry that is stable against mechanical dissociation yet is still compatible with MTFM probes is the use of gold-thiol (Au-SH) binding (**Figure 1.4c**). Using Au-SH binding is extraordinarily facile and avoids the need for a small-molecule quencher, since Au films and Au nanoparticles are effective quenchers. This type of MTFM sensor, developed by Liu et al.^{126, 127}, anchored a cRGD ligand to a gold nanoparticle (AuNP) through a PEG linkage and was sufficiently robust to withstand integrin-mediated tension. Since the AuNP in this probe acted as both the anchor and the quencher, the energy transfer mechanism in this probe is described as nanometal surface energy transfer (NSET) mechanism. Unlike FRET-based sensors, where energy transfer efficiency is dependent on the fluorophore-quencher distance with a $1/r^6$ relationship, energy transfer efficiency in NSET has a $1/r^4$ dependence. This distance dependence results in a more linear regime of fluorescence-distance response for NSET-based probes than is seen with FRET. In addition, NSET is highly efficient and typically displays larger R_0 values, thus probing

greater distances. Lastly, NSET efficiency has a weaker dependence on fluorophore transition dipole orientation and is therefore able to provide a more robust readout than FRET¹²⁸.

An additional advantage to using AuNP-based molecular tension sensors is the ability to pattern nanoparticles and explore the impact of clustering on force dynamics. Using the AuNP MTFM sensor, Liu et al. were able to determine that $\alpha_v\beta_3$ integrins exerted less force on cRGD ligands when receptors were separated by distances of 100 nm than when they were spaced by 50 nm¹²⁷. These experiments highlight the importance of molecular assemblies in the ability of cells to apply forces to the ECM and raises further questions regarding how these assemblies contribute to cellular adhesion and sensing of the surrounding physical environment. It also suggests that ligand spacing may be detected using mechanical sensing mechanisms.

To determine the magnitude of tension experienced by integrins during FA formation, it is necessary to avoid ensemble averaging. One solution to this problem is the use of single-molecule imaging, which was explored by Morimatsu et al.¹¹⁸. Given the challenges inherent in single-molecule imaging, our lab, along with the Chen lab, developed digital tension sensors. These digital probes utilize a DNA hairpin as the linker rather than an entropic PEG spring (**Figure 1.4d**)^{129, 130}. Our version of these probes employed three DNA strands, one containing a hairpin with a calibrated force threshold of unfolding and two that hybridize to the termini of the hairpin strand. These two strands act as arms to anchor the hairpin sensor to the surface and to present the cell adhesion ligand. A fluorophore and a quencher attached to the two DNA arms maintain close proximity when the hairpin is folded. When sufficient force is applied to open the hairpin

the fluorophore is separated from the quencher, thus leading to an increase in signal. The version of the DNA hairpin sensor developed by Blakely et al.¹³⁰ employs a single strand of DNA. This oligonucleotide contains the hairpin, the fluorophore-quencher pair, and the anchoring molecule. These sensors were functionalized with a linear and cyclic RGD ligand and were used to investigate forces applied by integrin receptors. Experiments revealed that integrin forces were highly dynamic and heterogeneous^{129, 130}. These results further support the role of ligand identity in modulating the amount of force that can be applied across integrin ligand bonds.

Another class of probes that use DNA to investigate the magnitude of tension across integrin-ligand bonds was reported by Wang and Ha¹³¹ and termed the tension gauge tether (TGT). The TGT consists of cRGD ligands bound to a surface by dsDNA that exhibits a known tension tolerance (T_{tol}). The T_{tol} is defined as the amount of tension required to rupture the dsDNA tether in less than 2 s under constant force. In order to examine the amount of mechanical tension required by cells to trigger adhesion and FA formation, cells were plated onto the TGT surface, and cell adhesion was monitored by phase-contrast microscopy. Surprisingly, these experiments revealed that initial cellular adhesion applies at least 33 to 43 pN of force to the substrate and that this tension, common to all cell types tested, is likely controlled by membrane tension mediated through integrin receptors. Furthermore, FA and cytoskeletal stress fiber formation required ~56 pN of tension applied by integrins. The TGT system was also used to examine forces involved in Notch receptor activation. However, experiments were unable to verify a specific force requirement for Notch activation.

1.3 Outlook

Molecular tension sensors have improved our ability to observe and study molecular forces in real time within living cells. One of the remaining challenges for these probes is to move away from ensemble averaging of forces to determine the level of tension per protein. The ability to achieve this would allow us to answer questions such as whether integrin receptors within focal adhesions experience similar forces or a range of dynamic and transient forces and whether the force propagated through focal adhesions is disseminated equally among all integrin receptors in the complex. The most obvious method to answer these questions involves single-molecule fluorescence microscopy using molecular tension probes. However, genetically encoded sensors require the use of fluorescent proteins, which represent a challenge for single-molecule studies. Compounding this challenge is the difficulty in controlling the number and density of genetically encoded sensors expressed in the cell. Immobilized sensors show more promise in this area, but obtaining a sparse density of tension sensors to image a few of the thousands of receptors within the functional focal adhesion offers only a limited view of the entire picture, where forces are precisely orchestrated in space and time. Another approach to address this challenge may be through super-resolution fluorescence microscopy techniques^{132, 133}. Already, the super-resolution technique iPALM (interferometric photoactivatable localization microscopy) has been used to determine the localization of proteins within FAs with nanometer resolution¹³⁴. An additional super-resolution imaging technique, Bayesian localization microscopy, has been used to image force in FAs using an immobilized sensor¹³⁵. It is likely that the combination of molecular tension sensors with superresolution techniques will become a rich area for exploration in mechanotransduction.

A benefit of the molecular tension sensors is the ability to observe downstream chemical signaling concurrent with fluorescence signals associated with tension. This allows one to correlate tension with specific cellular events. However, spectrum limitations can be challenging when downstream signaling is being explored. Since these sensors employ FRET as the signal output, only one (or possibly two) fluorescence signal can be used to monitor additional protein behavior in the cell in order to minimize confounding signals due to fluorescence bleed-through or cross talk. Sensors that use fluorescence quenchers rather than fluorescent FRET pairs have an advantage in this area, since more of the spectrum is available for tracking additional signals. For sensors that require two protein fluorophores, such as the genetically encoded sensors, this presents a challenge. Advanced imaging techniques, such as spectral imaging with linear unmixing, could present a solution to imaging with multiple fluorophores¹³⁶.

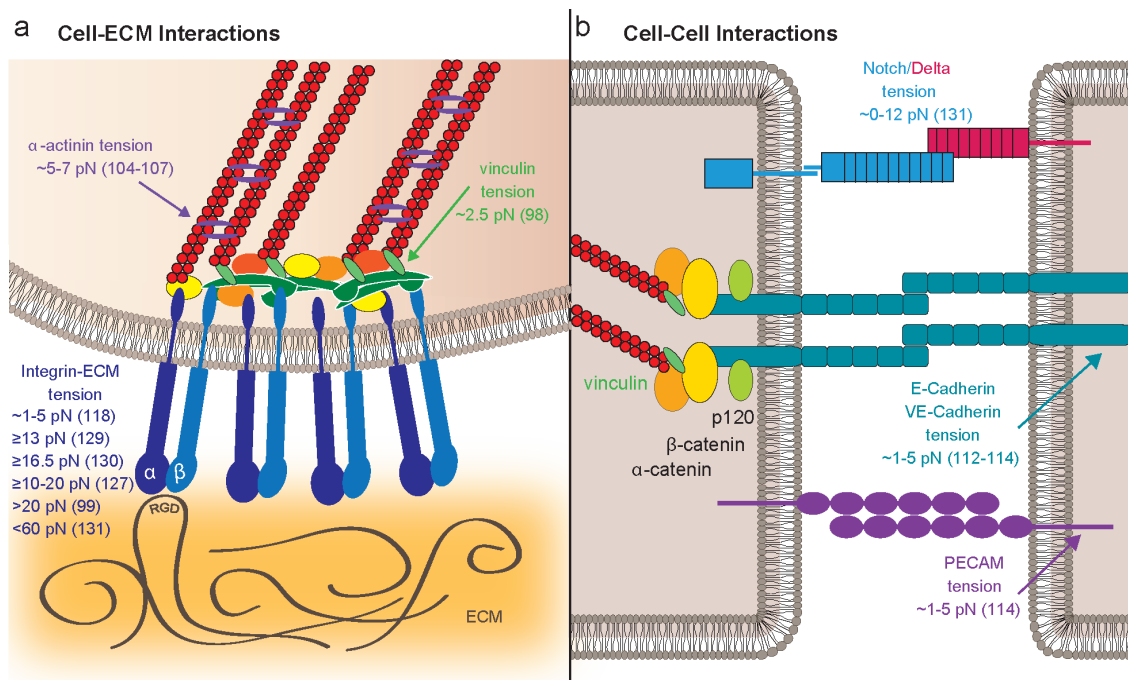


Figure 1.5 Schematic summary of tension values reported using molecular tension-sensing probes. (a) Cell-ECM interactions, typified by focal adhesions. Tension in α -actinin was measured using stFRET or sstFRET, while vinculin tension was determined

using the TSMod. Estimates of integrin-ECM tension were obtained using different types of immobilized molecular probes, including standard FRET-based MTFM, AuNP MTFM, DNA-hairpin sensors, and TGTs. Note that listed values were obtained using different cell types, different types of ECM ligands, and different classes of tension probes. (b) Representative schematic showing cell-cell interactions, such as cadherin complexes and Notch-Delta binding. Tension values applied by the Notch-Delta pathway, as tested by the TGT system, were reported to be either zero or less than 12 pN. E-cadherin, VE-cadherin, and PECAM tension was determined using the TSMod inserted into the cytoplasmic sites of the protein of interest.

There are still many questions yet to be answered regarding the role that biophysical signals play in cellular biology. As can be seen in **Figure 1.5**, tension values have been obtained for several cell adhesion proteins using the molecular tension probes discussed in this review. However, these values are not always consistent across various techniques, and more experiments need to be performed to address this issue.

Experiments with integrin receptors, specifically, have produced a wide range of estimates for tension. This may be a reflection of differences between the various tension observation techniques, including the use of different versions of ECM ligands. It may also suggest that forces applied by the cell through integrin receptors are highly dynamic. Also, differences in the force loading rate across the receptors may result in tension probe signals that vary dramatically. However, as yet, there are no robust methods to measure molecular force loading rates applied by cells. Additionally, targeting of specific integrin heterodimers with molecular tension probes has so far been limited to $\alpha_v\beta_3$. It would be interesting to see molecular tension probe studies that uniquely target other integrins, such as $\alpha_5\beta_1$, since catch-bond behavior has been reported only with $\alpha_5\beta_1$ integrins. There are also other FA-related proteins that have yet to be explored, such as the many adaptor proteins associated with FAs. The family of cadherins is beginning to be addressed, but there are still gaps in our knowledge. N-cadherin tension has not been explored, nor has

vinculin been explored in the context of cell-cell junctions. PECAM has been shown to be responsive to tension, but many other cell adhesion molecules may be involved.

There are hundreds of signaling pathways with the potential of having sensitivity to physical inputs. For example, the Notch signaling pathway, which is universally conserved across all metazoa and is fundamental to cell-cell communication and cell fate determination, has long been suspected of mechanical sensitivity. Notch receptors and their ligands are presented on the surfaces of two different cells, one that is signal sending (ligand cell) and one that is signal receiving (Notch cell). Activation of the receptor requires physical contact between the two cells. Notch contains a metalloprotease cleavage site hidden within the protein that is hypothesized to be exposed only when force is applied^{137, 138}. Therefore, proteolysis, leading to activation of the receptor, is suspected of being force dependent. In this case, endocytosis of the Notch-ligand complex by the ligand-expressing cell is thought to supply the force¹³⁹. Several lines of evidence have led to this hypothesis. It has been found that depletion of calcium releases the extracellular portion of the receptor and leads to receptor activation even in the absence of ligand¹⁴⁰. This is due to disruption of the region that masks the metalloprotease site and requires calcium to remain folded. It is also known that free ligand or mobile ligand does not typically activate Notch as well as bound or immobilized ligand^{141, 142}. Experimental evidence confirming the mechanism of force-mediated Notch activation in living cells is not yet conclusive. These studies have not been able to rule out the role of clustering in Notch activation. It has been shown that preclustered soluble ligand is capable of inducing Notch activation¹⁴³ while, in general, soluble ligand is not an efficient activator and, in some cases, can actually inhibit Notch

signaling¹⁴¹. Therefore, the question of how the Notch-ligand interaction leads to activation of the Notch receptor has not been fully resolved. The question of how Notch is activated represents a typical mechanistic challenge that faces the field of mechanotransduction.

Another frontier for mechanotransduction pertains to cell-pathogen interactions, which are already suspected of involving mechanics. For example, force-mediated extension of the CD4 receptor has been reported to be involved in HIV-1 infection of T cells¹⁴⁴. Looking forward, it is likely that fluorescence-based molecular tension probes will play a critical role in unraveling the physical aspects of cell signaling.

1.4 References

1. Yeung, T. et al. Effects of substrate stiffness on cell morphology, cytoskeletal structure, and adhesion. *Cell Motil Cytoskeleton* **2005**, *60*, 24-34.
2. Engler, A.J., Sen, S., Sweeney, H.L. & Discher, D.E. Matrix Elasticity Directs Stem Cell Lineage Specification. *Cell* **2006**, *126*, 677-689.
3. Holle, A.W. et al. *In situ* mechanotransduction via vinculin regulates stem cell differentiation. *Stem Cells* **2013**, *31*, 2467-2477.
4. Paszek, M.J. et al. Tensional homeostasis and the malignant phenotype. *Cancer Cell* **2005**, *8*, 241-254.
5. Shi, Q. et al. Rapid disorganization of mechanically interacting systems of mammary acini. *Proc. Natl. Acad. Sci. U.S.A.* **2014**, *111*, 658-663.
6. Leask, A. & Abraham, D.J. TGF- β signaling and the fibrotic response. *FASEB J.* **2004**, *18*, 816-827.

7. Pickup, M.W., Mouw, J.K. & Weaver, V.M. The extracellular matrix modulates the hallmarks of cancer. *EMBO Rep* **2014**, *15*, 1243-1253.
8. Katz, B. Depolarization of sensory terminals and the initiation of impulses in the muscle spindle. *J. Physiol.* **1950**, *111*, 261-282.
9. Guharay, F. & Sachs, F. Stretch-activated single ion channel currents in tissue-cultured embryonic chick skeletal muscle. *J. Physiol.* **1984**, *352*, 685-701.
10. Corey, D.P. & Hudspeth, A.J. Kinetics of the receptor current in bullfrog saccular hair cells. *J. Neurosci.* **1983**, *3*, 962-976.
11. Zhong, C. et al. Rho-mediated contractility exposes a cryptic site in fibronectin and induces fibronectin matrix assembly. *J. Cell Biol.* **1998**, *141*, 539-551.
12. Klotzsch, E. et al. Fibronectin forms the most extensible biological fibers displaying switchable force-exposed cryptic binding sites. *Proc. Natl. Acad. Sci. U.S.A.* **2009**, *106*, 18267-18272.
13. del Rio, A. et al. Stretching Single Talin Rod Molecules Activates Vinculin Binding. *Science* **2009**, *323*, 638-641.
14. Yao, M.X. et al. Mechanical activation of vinculin binding to talin locks talin in an unfolded conformation. *Sci. Rep.* **2014**, *4*, 4610.
15. Sawada, Y. et al. Force sensing by mechanical extension of the Src family kinase substrate p130Cas. *Cell* **2006**, *127*, 1015-1026.
16. Radmacher, M., Fritz, M., Cleveland, J.P., Walters, D.A. & Hansma, P.K. Imaging adhesion forces and elasticity of lysozyme adsorbed on mica with the atomic force microscope. *Langmuir* **1994**, *10*, 3809-3814.

17. Rotsch, C., Jacobsen, K. & Radmacher, M. Dimensional and mechanical dynamics of active and stable edges in motile fibroblasts investigated by using atomic force microscopy. *Proc. Natl. Acad. Sci. U.S.A.* **1999**, *96*, 921-926.
18. Rotsch, C. & Radmacher, M. Drug-induced changes of cytoskeletal structure and mechanics in fibroblasts: an atomic force microscopy study. *Biophys. J.* **2000**, *78*, 520-535.
19. Lehenkari, P.P. & Horton, M.A. Single integrin molecule adhesion forces in intact cells measured by atomic force spectroscopy. *Biochem. Biophys. Res. Comm.* **1999**, *259*, 645-650.
20. Charras, G.T. & Horton, M.A. Single cell mechanotransduction and its modulation analyzed by atomic force microscope indentation. *Biophys. J.* **2002**, *82*, 207-2981.
21. Wang, N., Butler, J.P. & Ingber, D.E. Mechanotransduction across the cell surface and through the cytoskeleton. *Science* **1993**, *260*, 1124-1127.
22. Ingber, D.E., Prusty, D., Sun, Z., Betensky, H. & Wang, N. Cell shape, cytoskeletal mechanics, and cell cycle control in angiogenesis. *J. Biomechanics* **1995**, *28*, 1471-1484.
23. Mijailovich, S.M., Kojic, M., Zivkovic, M., Fabry, B. & Fredberg, J.J. A finite element model of cell deformation during magnetic bead twisting. *J. Appl. Physiol.* **2002**, *93*, 1429-1436.
24. Deng, L., Fairbank, N.J., Fabry, B., Smith, P.G. & Maksym, G.N. Localized mechanical stress induces time-dependent actin cytoskeletal remodeling and

- stiffening in cultured airway smooth muscle cells. *Am. J. Physiol. Cell Physiol.* **2004**, *287*, C440-C448.
25. Trepap, X. et al. Viscoelasticity of human alveolar epithelial cells subjected to stretch. *Am. J. Physiol. Lung Cell Mol. Physiol.* **2004**, *287*, L1025-L1034.
 26. Mason, T.G., Ganesan, K., van Zanten, J.H., Wirtz, D. & Kuo, S.C. Particle tracking microrheology of complex fluids. *Phys. Rev. Lett.* **1997**, *79*, 3282-3285.
 27. Yamada, S., Wirtz, D. & Kuo, S.C. Mechanics of living cells measured by laser tracking microrheology. *Biophys. J.* **2000**, *78*, 1736-1747.
 28. Valentine, M.T. et al. Investigating the microenvironments of inhomogenous soft materials with multiple particle tracking. *Phys. Rev. E* **2001**, *64*, 061506.
 29. Tseng, Y., Kole, T.P. & Wirtz, D. Micromechanical mapping of live cells by multiple-particle-tracking microrheology. *Biophys. J.* **2002**, *83*, 3162-3176.
 30. Gordon, V.D. et al. Measuring mechanical stress induced by an expanding multicellular tumor system: a case study. *Exp. Cell Res.* **2003**, *289*, 58-66.
 31. Valentine, M.T. et al. Colloid surface chemistry critically affects multiple particle tracking measurements of biomaterials. *Biophys. J.* **2004**, *86*, 4004-4014.
 32. Heisterkamp, A. et al. Pulse energy dependence of subcellular dissection by femtosecond laser pulses. *Opt. Express* **2005**, *13*, 3690-3696.
 33. Kumar, S. et al. Viscoelastic retraction of single living stress fibers and its impact on cell shape, cytoskeletal organization, and extracellular matrix mechanics. *Biophys. J.* **2006**, *90*, 3762-3773.

34. Colombelli, J. et al. Mechanosensing in actin stress fibers revealed by a close correlation between force and protein localization. *J. Cell Sci.* **2009**, *122*, 1665-1679.
35. Chang, C.-W. & Kumar, S. Vinculin tension distributions of individual stress fibers within cell-matrix adhesions. *J. Cell Sci.* **2013**, *126*, 3021-3030.
36. Bruges, A. et al. Forces driving epithelial wound healing. *Nature Phys.* **2014**, *10*, 683-690.
37. Li, F., Redick, S.D., Erickson, H.P. & Moy, V.T. Force measurements of the $\alpha 5\beta 1$ integrin-fibronectin interaction. *Biophys. J.* **2003**, *84*, 1252-1262.
38. Kokkoli, E., Ochsenhirt, S.E. & Tirrel, M. Collective and single-molecule interactions of $\alpha 5\beta 1$ integrins. *Langmuir* **2004**, *20*, 2397-2404.
39. Lee, S., Yang, Y., Fishman, D., Banaszak Holl, M.M. & Hong, S. Epithelial-mesenchymal transition enhances nanoscale actin filament dynamics of ovarian cancer cells. *J. Phys. Chem. B* **2013**, *117*, 9233-9240.
40. Friedrichs, J., Taubenberger, A., Franz, C.M. & Muller, D.J. Cellular remodeling of individual collagen fibrils visualized by time-lapse AFM. *J. Mol. Biol.* **2007**, 594-607.
41. Nordin, D., Donlon, L. & Frankel, D. Characterising single fibronectin-integrin complexes. *Soft Matter* **2012**, *8*, 6151-6160.
42. Rakshit, S., Zhang, Y., Manibog, K., Shafriz, O. & Sivasankar, S. Ideal, catch, and slip bonds in cadherin adhesion. *Proc. Natl. Acad. Sci. U.S.A.* **2012**, *109*, 18815-18820.

43. Sun, Z., Martinez-Lemus, L.A., Hill, M.A. & Meininger, G.A. Extracellular matrix-specific focal adhesions in vascular smooth muscle produce mechanically active adhesion sites. *Am. J. Physiol. Cell Physiol.* **2008**, *295*, C268-C278.
44. Smith, S.B., Finzi, L. & Bustamante, C. Direct mechanical measurements of the elasticity of single DNA molecules by using magnetic beads. *Science* **1992**, *258*, 1122-1126.
45. Kellermayer, M.S.Z., Smith, S.B., Granzier, H.L. & Bustamante, C. Folding-unfolding transitions in single titin molecules characterized with laser tweezers. *Science* **1997**, *276*, 1112-1116.
46. Kuo, S.C. & Sheetz, M.P. Force of single kinesin molecules measured with optical tweezers. *Science* **1993**, *260*, 232-234.
47. Alenghat, F.J., Fabry, B., Tsai, K.Y., Goldman, W.H. & Ingber, D.E. Analysis of cell mechanics in single vinculin-deficient cells using a magnetic tweezer. *Biochem. Biophys. Res. Comm.* **2000**, *277*, 93-99.
48. Hayakawa, K., Tatsumi, H. & Sokobe, M. Actin stress fibers transmit and focus force to activate mechanosensitive channels. *J. Cell Sci.* **2008**, *121*, 495-503.
49. Molloy, J.E., Burns, J.E., Kendrick-Jones, J., Tregar, R.T. & White, D.C.S. Movement and force produced by a single myosin head. *Nature* **1995**, *378*, 209-212.
50. Walter, N., Selhuber, C., Kessler, H. & Spatz, J.P. Cellular unbinding forces of initial adhesion processes on nanopatterned surfaces probed with magnetic tweezers. *Nano Lett.* **2006**, *6*, 398-402.

51. Buckley, C.D. et al. The minimal cadherin-catenin complex binds to actin filaments under force. *Science* **2014**, *346*, 1254211.
52. Kong, F. et al. Cyclic mechanical reinforcement of integrin-ligand interactions. *Mol. Cell* **2013**, *49*, 1060-1068.
53. Chen, W., Lou, J., Evans, E. & Zhu, C. Observing force-regulated conformational changes and ligand dissociation from a single integrin on cells. *J. Cell Biol.* **2012**, *199*, 497-512.
54. Husson, J., Chemin, K., Bohineust, A., Hivroz, C. & Henry, N. Force generation upon T cell receptor engagement. *PLoS ONE* **2011**, *6*, e19680.
55. Liu, B., Chen, W., Evavold, B.D. & Zhu, C. Accumulation of dynamic catch bonds between TCR and agonist peptide-MHC triggers T cell signaling. *Cell* **2014**, *157*, 357-368.
56. Hynes, R.O. Integrins: bidirectional, allosteric signaling machines. *Cell* **2002**, *110*, 673-687.
57. Jiang, G., Giannone, G., Critchley, D.R., Fukumoto, E. & Sheetz, M.P. Two-piconewton slip bond between fibronectin and the cytoskeleton depends on talin. *Nature* **2003**, *424*, 334-337.
58. Roca-Cusachs, P., Gauthier, N.C., del Rio, A. & Sheetz, M.P. Clustering of alpha(5)beta(1) integrins determines adhesion strength whereas alpha(v)beta(3) and talin enable mechanotransduction. *Proceedings of the National Academy of Sciences of the United States of America* **2009**, *106*, 16245-16250.

59. Pelham, R.J. & Wang, Y.-L. High resolution detection of mechanical forces exerted by locomoting fibroblasts on the substrate. *Mol. Biol. Cell* **1999**, *10*, 935-945.
60. Dembo, M. & Wang, Y.-L. Stresses at the cell-to-substrate interface during locomotion of fibroblasts. *Biophys. J.* **1999**, *76*, 2307-2316.
61. Balaban, N.Q. et al. Force and focal adhesion assembly: a close relationship studied using elastic micropatterned substrates. *Nat. Cell Biol.* **2001**, *3*, 466-472.
62. Schwarz, U.S. et al. Calculation of forces at focal adhesions from elastic substrate data: The effect of localized force and the need for regularization. *Biophys. J.* **2002**, *83*, 1380-1394.
63. Sabass, B., Gardel, M.L., Waterman, C.M. & Schwarz, U.S. High resolution traction force microscopy based on experimental and computational advances. *Biophys. J.* **2008**, *94*, 201-220.
64. Tan, J.L. et al. Cells lying on a bed of microneedles: An approach to isolate mechanical force. *Proc. Natl. Acad. Sci. U.S.A.* **2003**, *100*, 1484-1489.
65. Bhadriraju, K. et al. Activation of ROCK by RhoA is regulated by cell adhesion, shape, and cytoskeletal tension. *Exp. Cell Res.* **2007**, *313*, 3616-3623.
66. Yang, M.T., Sniadecki, N.J. & Chen, C.S. Geometric considerations of micro- to nanoscale elastomeric post arrays to study cellular traction forces. *Adv. Mater.* **2007**, *19*, 3119-3123.
67. Lemmon, C.A., Chen, C.S. & Romer, L.H. Cell traction forces direct fibronectin matrix assembly. *Biophys. J.* **2009**, *96*, 729-738.

68. Ruiz, S.A. & Chen, C.S. Emergence of patterned stem cell differentiation within multicellular structures. *Stem Cells* **2008**, *26*, 2921-2927.
69. Liu, Z. et al. Mechanical tugging force regulates the size of cell-cell junctions. *Proc. Natl. Acad. Sci. U.S.A.* **2010**, *107*, 9944-9949.
70. Fu, J. et al. Mechanical regulation of cell function with geometrically modulated elastomeric substrates. *Nat. Methods* **2010**, *7*, 733-736.
71. Lin, G.L. et al. Activation of beta 1 but not beta 3 integrin increases cell traction forces. *FEBS Lett.* **2013**, *587*, 763-769.
72. Dumbauld, D.W. et al. How vinculin regulates force transmission. *Proc. Natl. Acad. Sci. U.S.A.* **2013**, *110*, 9788-9793.
73. Plotnikov, S.V., Pasapera, A.M., Sabass, B. & Waterman, C.M. Force fluctuations within focal adhesions mediate ECM-rigidity sensing to guide directed cell migration. *Cell* **2012**, *151*, 1513-1527.
74. Prager-Khoutorsky, M. et al. Fibroblast polarization is a matrix-rigidity-dependent process controlled by focal adhesion mechanosensing. *Nat. Cell Biol.* **2011**, *13*, 1457-1465.
75. Lakowicz, J.R. Principles of Fluorescence Spectroscopy, Edn. 3rd edn. (Springer, New York; 2006).
76. Santoso, Y. et al. Conformational transitions in DNA polymerase I revealed by single-molecule FRET. *Proc. Natl. Acad. Sci. U.S.A.* **2010**, *107*, 715-720.
77. Choi, U.B. et al. Single-molecule FRET-derived model of the synaptotagmin 1-SNARE fusion complex. *Nature* **2010**, *17*, 318-325.

78. Ernst, S., Duser, M.G., Zarrabi, N., Dunn, S.D. & Borsch, M. Elastic deformations of the rotary double motor of single F₀F₁-ATP synthases detected in real time by Forster resonance energy transfer. *Biochim. Biophys. Acta* **2012**, *1817*, 1722-1731.
79. Verhalen, B., Ernst, S., Borsch, M. & Wilkens, S. Dynamic ligand-induced conformational rearrangements in P-glycoprotein as probed by fluorescence resonance energy transfer spectroscopy. *J. Biol. Chem.* **2012**, *287*, 1112-1127.
80. Guo, Z. & Noller, H.F. Rotation of the head of the 30S ribosomal subunit during mRNA translocation. *Proc. Natl. Acad. Sci. U.S.A.* **2012**, *109*, 20391-20394.
81. Ting, A.Y., Kain, K.H., Klemke, R.L. & Tsien, R.Y. Genetically encoded fluorescent reporters of protein tyrosine kinase activities in living cells. *Proc. Natl. Acad. Sci. U.S.A.* **2001**, *98*, 15003-15008.
82. Wang, Y. et al. Visualizing the mechanical activation of Src. *Nature* **2005**, *434*, 1040-1045.
83. Na, S. et al. Rapid signal transduction in living cells is a unique feature of mechanotransduction. *Proc. Natl. Acad. Sci. U.S.A.* **2008**, *105*, 6626-6631.
84. Ouyang, M., Sun, J., Chien, S. & Wang, Y. Determination of hierarchical relationship of Src and Rac at subcellular locations with FRET biosensors. *Proc. Natl. Acad. Sci. U.S.A.* **2008**, *105*, 14353-14358.
85. Seong, J. et al. Detection of focal adhesion kinase activation at membrane microdomains by fluorescence resonance energy transfer. *Nat. Commun.* **2011**, *2*, 406.

86. Kraynov, V.S. et al. Localized Rac activation dynamics visualized in living cells. *Science* **2000**, *290*, 333-337.
87. Pertz, O., Hodgson, L., Klemke, R.L. & Hahn, K.M. Spatiotemporal dynamics of RhoA activity in migrating cells. *Nature* **2006**, *440*, 1069-1072.
88. Machacek, M. et al. Coordination of Rho GTPase activities during cell protrusion. *Nature* **2009**, *461*, 99-103.
89. Baneyx, G., Baugh, L. & Vogel, V. Fibronectin extension and unfolding within cell matrix fibrils controlled by cytoskeletal tension. *Proc. Natl. Acad. Sci. U.S.A.* **2002**, *99*, 5139-5143.
90. Smith, M.L. et al. Force-induced unfolding of fibronectin in the extracellular matrix of living cells. *PLoS Biol.* **2007**, *5*, e268.
91. Legant, W.R., Chen, C.S. & Vogel, V. Force-induced fibronectin assembly and matrix remodeling in a 3D microtissue model of tissue morphogenesis. *Integr. Biol.* **2012**, *4*, 1164-1174.
92. Kong, H.J., Polte, T.R., Alsberg, E. & Mooney, D.J. FRET measurements of cell-contraction forces and nano-scale clustering of adhesion ligands varied by substrate stiffness. *Proc. Natl. Acad. Sci. U.S.A.* **2005**, *102*, 4300-4305.
93. Friedland, J.C., Lee, M.H. & Boettiger, D. Mechanically activated integrin switch controls $\alpha 5 \beta 1$ function. *Science* **2009**, *323*, 642-644.
94. Kong, F., Garcia, A.J., Mould, A.P., Humphries, M.J. & Zhu, C. Demonstration of catch bonds between an integrin and its ligand. *J. Cell Biol.* **2009**, *185*, 1275-1284.

95. Bell, G.I. Models for the specific adhesion of cells to cells. *Science* **1978**, *200*, 618-627.
96. Dembo, M., Torney, D.C., Saxman, K. & Hammer, D. The reaction-limited kinetics of membrane-to-surface adhesion and detachment. *Proc. R. Soc. Lond. B Biol. Sci.* **1988**, *234*, 55-83.
97. Marshall, B.T. et al. Direct observation of catch bonds involving cell-adhesion molecules. *Nature* **2003**, *423*, 190-193.
98. Grashoff, C. et al. Measuring mechanical tension across vinculin reveals regulation of focal adhesion dynamics. *Nature* **2010**, *466*, 263-266.
99. Jurchenko, C., Chang, Y., Narui, Y., Zhang, Y. & Salaita, K.S. Integrin-generated forces lead to streptavidin-biotin unbinding in cellular adhesions. *Biophys. J.* **2014**, *106*, 1436-1446.
100. Austen, K., Kluger, C., Freikamp, A., Chrostek-Grashoff, A. & Grashoff, C. in *Cell-Cell Interactions*, Edn. 2nd. (ed. T.A. Baudino) (Springer, New York; 2013).
101. LaCroix, A.S., Rothenberg, K.E., Berginski, M.E., Urs, A.N. & Hoffman, B.D. Construction, imaging, and analysis of FRET-based tension sensors in living cells. *Methods Cell Biol.* **2015**, *125*, 161-186.
102. Guo, J., Sachs, F. & Meng, F. Fluorescence-based force/tension sensors: A novel tool to visualize mechanical forces in structural proteins in live cells. *Antioxid. Redox. Signal* **2014**, *20*, 986-999.
103. Meng, F., Suchyna, T.M. & Sachs, F. A fluorescence energy transfer-based mechanical stress sensor for specific proteins in situ. *FEBS J.* **2008**, *275*, 3072-3087.

104. Iwai, S. & Uyeda, T.Q.P. Visualizing myosin–actin interaction with a genetically-encoded fluorescent strain sensor. *Proc. Natl. Acad. Sci. U.S.A.* **2008**, *105*, 16882-16887.
105. Meng, F., Suchyna, T.M., Lazakovitch, E., Gronostajski, R.M. & Sachs, F. Real time FRET based detection of mechanical stress in cytoskeletal and extracellular matrix proteins. *Cell. Mol. Bioeng.* **2011**, *4*, 148-159.
106. Meng, F. & Sachs, F. Visualizing dynamic cytoplasmic forces with a compliance-matched FRET sensor. *J. Cell Sci.* **2011**, *124*, 261-269.
107. Rahimzadeh, J. et al. Real-time observation of flow-induced cytoskeletal stress in living cells. *Am. J. Physiol. Cell Physiol.* **2011**, *301*, C646-C652.
108. Ye, N. et al. Direct observation of α -actinin tension and recruitment at focal adhesions during contact growth. *Exp. Cell Res.* **2014**.
109. Meng, F. & Sachs, F. Orientation-based FRET sensor for real-time imaging of cellular forces. *J. Cell Sci.* **2012**, *125*, 743-750.
110. De Angelis, D.A., Miesenbock, G., Zemelman, B.V. & Rothman, J.E. PRIM: Proximity imaging of green fluorescent protein-tagged polypeptides. *Proc. Natl. Acad. Sci. U.S.A.* **1998**, *95*, 12312-12316.
111. Iwai, S. & Uyeda, T.Q.P. Myosin-actin interaction in Dictyostelium cells revealed by GFP-based strain sensor and validated linear spectral unmixing. *Cytometry A* **2010**, *77A*, 743-750.
112. Borghi, N. et al. E-cadherin is under constitutive actomyosin-generated tension that is increased at cell-cell contacts upon externally applied stretch. *Proc. Natl. Acad. Sci. U.S.A.* **2012**, *109*, 12568-12573.

113. Cai, D. et al. Mechanical feedback through E-cadherin promotes direction sensing during collective cell migration. *Cell* **2014**, *157*, 1146-1159.
114. Conway, D.E. et al. Fluid shear stress on endothelial cells modulates mechanical tension across VE-cadherin and PECAM-1. *Curr. Biol.* **2013**, *23*, 1024-1030.
115. Krieg, M., Dunn, A.R. & Goodman, M.B. Mechanical control of the sense of touch by B-spectrin. *Nat. Cell Biol.* **2014**, *16*, 224-232.
116. Paszek, M.J. et al. The cancer glycocalyx mechanically primes integrin-mediated growth and survival. *Nature* **2014**, *511*, 319-325.
117. Stabley, D.R., Jurchenko, C., Marshall, S.S. & Salaita, K.S. Visualizing mechanical tension across membrane receptors with a fluorescent sensor. *Nat. Methods* **2012**, *9*, 64-67.
118. Morimatsu, M., Mekhdjian, A.H., Adhikari, A.S. & Dunn, A.R. Molecular tension sensors report forces generated by single integrin molecules in living cells. *Nano Lett.* **2013**, *13*, 3985-3989.
119. Green, N.M. Avidin and Streptavidin. *Methods Enzymol.* **1990**, *184*, 51-67.
120. Pfaff, M. et al. Selective recognition of cyclic RGD peptides of NMR defined conformation by α II β 3, α V β 3, and α 5 β 1 integrins. *J. Biol. Chem.* **1994**, *269*, 20233-20238.
121. Englund, E.A. et al. Programmable multivalent display of receptor ligands using peptide nucleic acid nanoscaffolds. *Nat. Commun.* **2012**, *3*, 614.
122. Jamali, Y., Jamali, T. & Mofrad, R.R.K. An agent based model of integrin clustering: Exploring the role of ligand clustering, integrin homo-oligomerization,

- integrin-ligand affinity, membrane crowdedness and ligand mobility. *J. Comp. Phys.* **2013**, *244*, 264-278.
123. Deng, L., Kitova, E.N. & Klassen, J.S. Dissociation kinetics of the streptavidin-biotin interaction measured using direct electrospray ionization mass spectrometry analysis. *J. Am. Mass Spectrom.* **2013**, *24*, 49-56.
124. Klumb, L.A.C., V.; Stayton, P.S. Energetic roles of hydrogen bonds at the ureido oxygen binding pocket in the streptavidin-biotin complex. *Biochemistry* **1998**, *37*, 7657-7663.
125. Tabard-Cossa, V. et al. Single-molecule bonds characterized by solid-state nanopore force spectroscopy. *ACS Nano* **2009**, *3*, 3009-3014.
126. Liu, Y., Yehl, K., Narui, Y. & Salaita, K. Tension sensing nanoparticles for mechano-imaging at the living/nonliving interface. *J. Am. Chem. Soc.* **2013**, *135*, 5320-5323.
127. Liu, Y. et al. Nanoparticle tension probes patterned at the nanoscale: Impact of integrin clustering on force transmission. *Nano Lett.* **2014**, *14*, 5539-5546.
128. Yun, C.S. et al. Nanometal surface energy transfer in optical rulers, breaking the FRET barrier. *J. Am. Chem. Soc.* **2005**, *127*, 3115-3119.
129. Zhang, Y., Ge, C., Zhu, C. & Salaita, K. DNA-based digital tension probes reveal integrin forces during early cell adhesion. *Nat. Commun.* **2014**, *5*, 5167.
130. Blakely, B.L. et al. A DNA-based molecular probe for optically reporting cellular traction forces. *Nat. Methods* **2014**, *11*, 1229-1232.
131. Wang, X. & Ha, T. Defining single molecular forces required to activate integrin and Notch signaling. *Science* **2013**, *340*, 991-994.

132. Huang, B., Bates, M. & Zhuang, X. Super resolution fluorescence microscopy. *Annu. Rev. Biochem.* **2009**, *78*, 993-1016.
133. Schermelleh, L., Heintzmann, R. & Leonhardt, H. A guide to super-resolution fluorescence microscopy. *J. Cell Biol.* **2010**, *190*, 165-175.
134. Kanchanawong, P. et al. Nanoscale architecture of integrin-based cell adhesions. *Nature* **2010**, *468*, 580-586.
135. Morimatsu, M., Mekhdjian, A.H., Chang, A.C., Tan, S.J. & Dunn, A.R. Visualizing the interior architecture of focal adhesions with high-resolution traction maps. *Nano Lett.* **2015**, *15*, 2220-2228.
136. Zimmerman, T., Rietdorf, J. & Pepperkok, R. Spectral imaging and its application in live cell microscopy. *FEBS J.* **2003**, *546*, 87-92.
137. Gordon, W.R. et al. Structural basis for autoinhibition of Notch. *Nat. Struct. Molec. Biol.* **2007**, *14*, 295-300.
138. Stephenson, N.L. & Avis, J.M. Direct observation of proteolytic cleavage at the S2 site upon forced unfolding of the Notch negative regulatory region. *Proc. Natl. Acad. Sci. U.S.A.* **2012**, *109*, E2757-E2765.
139. Meloty-Kapella, L., Shergill, B., Kuon, J., Botvinick, E. & Weinmaster, G. Notch ligand endocytosis generates mechanical pulling force dependent on dynamin, epsins, and actin. *Develop. Cell* **2012**, *22*, 1299-1312.
140. Rand, M.D. et al. Calcium depletion dissociates and activates heterodimeric Notch receptors. *Mol. Cell. Biol.* **2000**, *20*, 1825-1835.

141. Sun, X. & Artavanis-Tsakonas, S. Secreted forms of DELTA and SERRATE define antagonists of Notch signaling in *Drosophila*. *Development* **1997**, *124*, 3439-3448.
142. Narui, Y. & Salaita, K. Membrane tethered Delta activates Notch and reveals a role for spatio-mechanical regulation of the signaling pathway. *Biophys. J.* **2013**, *105*, 2655-2665.
143. Hicks, C. et al. A secreted Delta1-Fc fusion protein functions both as an activator and inhibitor of Notch1 signaling. *J. Neurosci. Res.* **2002**, *68*, 655-667.
144. Perez-Jimenez, R. et al. Probing the effect of force on HIV-1 receptor CD4. *ACS Nano* **2014**, *8*, 10313-10320.

Chapter 2: Visualizing mechanical tension across membrane receptors with a fluorescent sensor

Adapted from Stabley, D.R.; Jurchenko, C.; Marshall, S.S.; Salaita, K.S. Visualizing mechanical tension across membrane receptors with a fluorescent sensor. *Nat. Meth.* **2012**, *9*, 64-67, used with permission.

2.1 Development of a fluorescence-based molecular tension sensor

2.1.1 Motivation for developing a molecular mechanosensor

The interplay between physical inputs and chemical reaction cascades coordinates a diverse set of biological processes that range from epithelial cell adhesion and migration to stem cell differentiation and immune response^{1,2}. The majority of these mechanical inputs are sensed and transduced through membrane receptors that mount a signaling cascade depending on the mechanical properties of their specific cognate ligands². A major challenge to understanding the molecular mechanisms of mechanotransduction is in the development of tools that can be used to measure forces applied to specific receptors on the cell surface³.

To address this challenge, two main classes of techniques have been developed. The first class uses single-molecule force spectroscopy methods such as atomic force microscopy and optical or magnetic tweezers to measure forces at specific sites on the cell surface^{3,4}. These approaches provide key measurements for cell-surface receptors, but the inherent serial nature of single-molecule force spectroscopy methods coupled with the need for statistically significant datasets in cell biology has hampered their widespread adoption⁴. The second category of approaches developed for measuring biophysical forces in vivo is the genetically encoded protein-tension sensors⁵⁻⁷. These sensors are composed of three domains that include a pair of fluorescent proteins linked via an elastic amino-acid domain and inserted into a suitable site in a host protein. However, the vast majority of membrane proteins and many structurally sensitive cytoplasmic proteins will not regain wild-type function upon splitting and insertion of the tension sensor into the host protein. In the absence of methods for measuring mechanical

tension across the hundreds or thousands of proteins on the cell membrane or structurally sensitive soluble proteins, understanding chemo-mechanical couplings will remain a considerable challenge.

2.1.2 Design of the sensor

Here we report a molecular-tension sensor that can be used to spatially and temporally map forces exerted by cell-surface receptors. The sensor consists of a flexible linker that is covalently conjugated to a biological ligand at one terminus and anchored onto a surface (via a biotin-streptavidin interaction) such that mechanical forces do not result in sensor translocation (**Figure 2.1a, b**). We chose a linker comprised of a polyethylene glycol (PEG) polymer because of its unique properties that include: (i) well-characterized and reversible force-extension curves^{8, 9}, (ii) biocompatibility¹⁰, and (iii) minimal nonspecific interactions with other biomolecules¹¹. We functionalized the ligand and the surface with fluorophore and quencher molecules, respectively. Cellular forces exerted on the ligand extend the linker from its relaxed conformational state and remove the fluorophore from proximity to the quencher, thus resulting in increased fluorescence intensity and providing a signal to map mechanical tension transduced through specific receptor targets (**Figure 2.1b**). The approach is, in principle, noninvasive and can be used to map forces with single-molecule spatial resolution and high temporal resolution in living cells. Notably, this method only requires the use of a conventional fluorescence microscope and precludes the necessity of genetic engineering of target receptors.

2.2 Application of the sensor

As a proof of concept, we used our tension sensor to map forces associated with initial uptake and trafficking of the epidermal growth factor receptor (EGFR) upon

binding to its cognate ligand. The EGFR pathway has important roles in cell survival, proliferation and differentiation, and internalization is an important regulatory component in the normal physiology of this pathway¹²; it is one of the most widely studied experimental systems for investigating ligand-induced receptor endocytosis. Still, fundamental questions about the role and even the existence of forces in shuttling the receptor from the cell membrane to endosomal compartments remain³. It seems rational to conclude that the process of endocytosis requires the application of a force to transport the EGFR-EGF complex, but specific evidence is thus far lacking¹³.

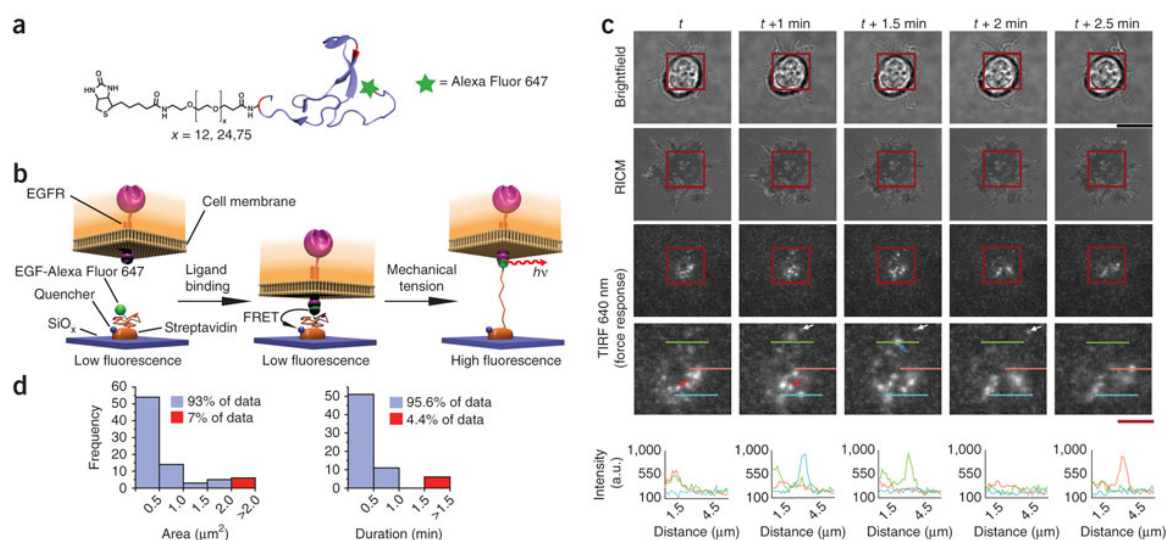


Figure 2.1 Design and response of the EGFR tension sensor. **(a)** Schematic of the EGF-PEG_x ($x = 12, 24$ or 75) tension sensor, comprised of a PEG polymer of length x that is flanked by fluorescently labeled (Alexa Fluor 647) EGF ligand and a biotin moiety for surface immobilization via streptavidin capture. EGF crystal structure adapted from Protein Data Bank [IJL9]. Residues in red in the crystal structure represent lysine and the N terminus, which are the available sites for PEG and fluorophore modification. **(b)** Schematic of the mechanism of sensor function. When EGFR exerts a force on its ligand, the flexible PEG linker extends. The displacement of the EGF ligand results in an increase in the measured fluorescence intensity, thus reporting the transmission of mechanical tension through the EGF-EGFR complex. $h\nu$, emission of a photon. **(c)** Representative brightfield, reflection interference contrast microscopy (RICM) and EGFR tension sensor TIRF response of HCC1143 cells plated onto sensor surfaces at 37 °C for the indicated time points (t represents the start of imaging). Images on the bottom show magnification of the boxed regions. Colored line scans represent 34 pixel profiles through the indicated region; the color of each line corresponds to the graph shown below

each set of frames. The white, red and blue arrows highlight fluorescent spots that persisted for 90 s, 60 s and 30 s, respectively. Black scale bar, 20 μm ; red scale bar, 4 μm . Fluorescence intensity is given in arbitrary units (a.u.). **(d)** Histograms of the areas ($n = 82$) and the durations ($n = 68$) of fluorescent points under a cell that was observed for 10 min.

2.3 Characterization of the sensor

We synthesized tension sensors that present the EGF ligand and can be used to specifically measure force transmission through the EGFR (**Figure 2.1 and Figure A2.1**). To characterize the conformation of the sensor in the resting state (in the absence of cellular forces), we tethered the EGF-PEG conjugate to a fluid supported lipid bilayer. The supported lipid bilayer surface provides a well-controlled biomimetic environment in which the protein density can be quantitatively measured and tuned¹⁴. The sensors are homogeneously displayed on the laterally mobile supported lipid bilayer surface as indicated by fluorescence recovery after photobleaching (**Figure A2.2**). Quantitative fluorescence resonance energy transfer (FRET) efficiency measurements showed that the sensor conjugates adopted a condensed mushroom-like conformation with the EGF located 5.5 ± 0.1 nm, 5.2 ± 0.2 nm and 7.0 ± 0.2 nm (mean \pm s.e.m., $n = 3$) from the surface for the EGF-PEG_x conjugates, where $x = 12, 24$ and 75 monomer units, respectively (**Figure A2.2**). These distance values suggest that the EGF-PEG₂₄ and EGF-PEG₇₅ linkers adopt their predicted Flory radii^{8, 9, 15}. Consequently, the resting-state structures of the EGF-PEG₇₅ and EGF-PEG₂₄ sensor conjugates were at $\sim 25\%$ and $\sim 57\%$ of their full contour lengths, respectively, which implies that the fluorescence intensity is expected to increase considerably as the PEG linkers are fully extended. Although the conformation of PEG polymers in solution is temperature- and solvent-dependent^{8, 15}, we found that the equilibrium conformation of the force sensor was not appreciably altered at

physiological conditions (37 °C and phosphate-buffered saline (pH 7.4)) (**Figure A2.3**). Therefore, these data, along with experimental and theoretical literature precedent investigating the force extension of PEG polymers and their protein conjugates^{8, 9, 16, 17}, predict that the dynamic range of the EGF-PEG force sensors directly depends on the length of the PEG linker. For example, the dynamic range of EGF-PEG₂₄ conjugates is expected to be 0–20 pN, and >95% of the maximum fluorescence intensity will be observed with the application of a 20 pN force (**Figure A2.4**). This range is compatible with the range of forces inherent to many biological processes^{1, 3, 5}. When we engaged immortalized human breast cancer cells (HCC1143) to the EGFR tension sensor surface, receptors expressed in the cell membrane bound to their cognate ligands. Within 20–30 min of cell spreading, we observed transient and localized increases in fluorescence intensity via time-lapse total internal reflection fluorescence (TIRF) microscopy, which exclusively probes molecules within 150 nm of the substrate (**Figure 2.1c**). The bright spots were diffraction-limited (**Figure 2.1c, d**), suggesting that the observed events were localized to punctate points that experience mechanical tension. Additional analysis revealed that the localized increases in fluorescence were short-lived, seldom persisting longer than 30 s, and that there was a range of lifetime distributions for points across the cell-substrate contact plane (**Figure 2.1c, d**). The fluorescence intensity at these spots then returned to the background amount, indicating that the fluorophore-labeled EGF remains bound to the sensor surface. We did not observe noteworthy photobleaching under these time-lapse imaging conditions during the first 20–30 frames. The recovery of the fluorescence intensity to the background level after the transient increase may be a consequence of ligand-receptor dissociation or diminished cellular pulling, and we could

not distinguish between these two events in these experiments. The mechanism of complete internalization is most likely stalled because the ligand is tethered to the substrate, and thus the measured mechanical forces are associated with the initial steps of ligand uptake.

Given that a wide array of adhesion receptors may interact with the underlying substrate, we tested the specificity of our tension sensor to EGFR using three sets of control experiments. First, we synthesized bovine serum albumin (BSA) force-sensor conjugates and plated cells on these substrates. The BSA conjugates under the cells displayed no fluorescence response as detected by TIRF imaging 30 min after plating (**Figure A2.5**). Second, we pretreated cells with 1.7 nM soluble EGF for 5 min, then plated these cells on the EGF force-sensor surfaces and also did not observe an optical response (**Figure A2.6**). Finally, to determine the role of an apposed ligand in the specificity of the force response, we incorporated a cyclic Arg-Gly-Asp (RGD) peptide ligand into the BSA-force sensor surface. Unlike the first two controls, cells strongly engaged these surfaces, as indicated by reflection interference contrast microscopy imaging, but the observed fluorescence response was negligible (**Figure A2.7**). Taken together, these experiments confirmed that the measured responses were specific to force transmission through the EGFR.

To examine the role of the PEG linker and the specific fluorophore (Alexa Fluor 647) and quencher (QSY 21) pair (Forster radius, $R_0=6.9$ nm according to the manufacturer) in the observed fluorescence response, we performed cell-tension measurements with sensors displaying short linkers (contour length of 2.2 nm) or with sensors that lacked the quencher tags. In these experiments, we quantified the force

response in single cells and normalized it to the background signal (**Figure A2.8**).

Experiments with sensor containing a 2.2 nm linker showed minimal response when compared to the 26 nm PEG₇₅ linkers (**Figure 2.2a**). Similarly, sensors that lacked the quencher did not exhibit a notable fluorescence increase (**Figure 2.2a and Figure A2.9**).

To eliminate the possibility that direct ligand-receptor binding may lead to sensor response, we treated EGF force probe surfaces with a monoclonal EGF antibody. This treatment did not result in a sensor response (**Figure A2.10**). To ensure that the biological activity of the EGF ligand was not influenced by the length (flexibility) of the different linkers, we immunostained cells with an antibody to phospho (p)Tyr1068 of EGFR to measure the relative activation. Single-cell fluorescence analysis did not indicate a marked difference in immunostaining between cells activated with tension-sensor surfaces that used 2.2 nm or 26 nm linker contour lengths, thus showing that cells were similarly activated (**Figure A2.11**). Overall, these experiments showed that the tension sensor requires a flexible linker that is appropriately matched to the Forster radius of the dye pair.

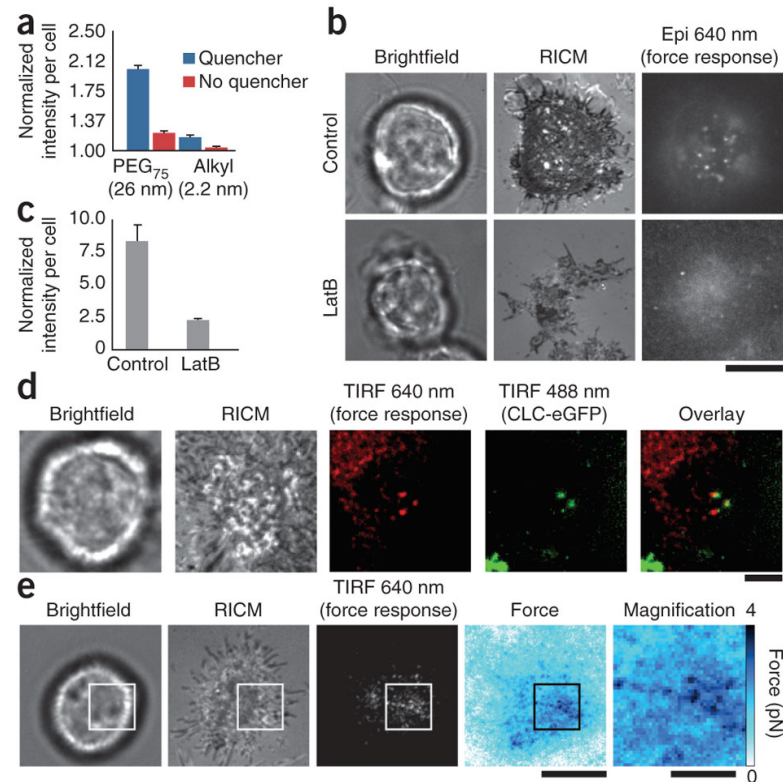


Figure 2.2 Characterization and quantification of the EGFR tension sensor. **(a)** Role of the flexible linker (alkyl, 2.2 nm or PEG₇₅, 26 nm) and the quencher in the EGFR tension sensor response. Error bars, s.e.m. ($n = 77$ cells). **(b)** Representative brightfield, reflection interference contrast microscopy (RICM) and EGFR tension sensor response (epifluorescence (epi) 640 nm) channels for cells treated with latrunculin B (LatB) or control (DMSO). Scale bar, 5 μm . **(c)** Measured EGF force response (normalized fluorescence intensity) between LatB-treated ($n = 33$ cells) and untreated ($n = 32$ cells). Error bars, s.e.m. **(d)** Representative dual channel TIRF microscopy images of a *CLC-eGFP*-transfected cell engaged to the force-sensing surface. Overlay channel shows colocalization of CLC-eGFP and the EGF-force response. Scale bar, 5 μm . **(e)** Representative brightfield, RICM and fluorescence response for a cell engaged to an EGF-PEG₂₄ force sensor surface. The sensor fluorescence response was converted into a force map by using the extended WLC model for PEG₂₄. Scale bars, 10 μm (3.2 μm in the magnified image).

2.4 Correlation of EGFR endocytosis with sensor signal

EGFR endocytosis is thought to primarily proceed through an internalization pathway that is mediated through the cytoskeleton and clathrin-coated pits¹². To look for evidence for the role of the cytoskeleton in mechanotransduction, we treated cells with

latrunculin B, a cytoskeletal inhibitor that targets the assembly of F-actin. This led to a 70% reduction in sensor response, indicating that physical tension is dependent on proper function of the cytoskeleton (**Figure 2.2b, c**). To confirm that mechanical force is associated with clathrin-coated pit invagination, we transiently transfected the HCC1143 cells with a construct encoding clathrin light chain–enhanced GFP (eGFP) (CLC-eGFP). Using live-cell dual-channel TIRF microscopy we measured the association of CLC-eGFP with the EGFR tension sensor. We observed diffraction-limited bright spots in both fluorescence channels (**Figure 2.2d**). Taken together, the average lifetimes and dimensions of the punctate points along with actin-dependence and clathrin-colocalization data all confirm that the mechanical pulling events are consistent with a clathrin-mediated EGF internalization mechanism¹⁸.

Our tension sensor design allows for precise quantification of the magnitude of the applied force required to extend the PEG linker from its resting state. We determined the physical extension of the linker from the FRET relation and then used this displacement to estimate the mechanical tension using the extended worm-like chain (WLC) model (**Figure A2.12** and Materials and Methods)^{8, 9, 16}. This conversion is possible owing to the fact that PEG is a well-behaved polymer whose force-extension profile experimentally fits the extended WLC with high accuracy (less than 1% error) in PBS buffer¹⁶. We used monolabeled EGF-PEG₂₄ conjugates because of their broad dynamic range for force quantification. We generated a representative force map for a cell that engaged the EGF tension sensor for 30 min (**Figure 2.2e**). The punctate fluorescent regions showed a peak force value of approximately 4 pN, which represents the lower-bound ensemble average force applied by the EGF receptor on that area.

Our tension sensor design provides a general method for mapping mechanical tension experienced by specific membrane proteins on the surface of living cells. These tension maps provide, to our knowledge, the first direct evidence showing that mechanical forces are associated with the initial stages of EGF ligand internalization. This method could be applied to rapidly study chemo-mechanical interactions across nearly any receptor or cell type. The inherent flexibility of the platform may also enable the investigation of mechanical force transmission across cell-cell junctions, such as those between T cells and antigen-presenting cells as well as epithelial cell junctions, which are typically not amenable to direct investigations by other methods.

2.5 Materials and methods

2.5.1 Synthesis and characterization of streptavidin-quencher conjugates

A streptavidin labeling ratio of 1 was desired to accurately use the FRET relation and determine the zero-force conformation of the sensor. Recombinant streptavidin (Rockland Immunochemicals) was labeled with quencher by mixing 300 μg of the protein in 150 μl of PBS (10 mM phosphate buffer, 137 mM NaCl, pH 7.4) with 15 μl of 1 M sodium bicarbonate and a 20-fold molar excess of QSY 21 N-hydroxysuccinimide (NHS) ester (Invitrogen). The reaction was allowed to proceed for 60 min at room temperature (23 $^{\circ}\text{C}$) on a rotating platform. Purification was performed by size-exclusion chromatography using Bio-Gel P4 resin (Bio-Rad) swollen with PBS. The final product was characterized using matrix-assisted laser desorption–time-of-flight (MALDI-TOF) mass spectrometry. The labeling ratio was determined to be 0.8 by UV-visible light absorbance measurements of the gel-purified product.

For all other experiments, recombinant streptavidin was labeled with quencher by

mixing 1 mg ml^{-1} of the protein in PBS with an excess of QSY 21 NHS ester. The reaction was allowed to proceed for 60 min at room temperature, and the tube was inverted every 15 min to ensure proper mixing. The product was purified with a Slide-a-Lyzer Mini dialysis column (Thermo Fisher) with a cutoff of $3,500 \text{ g mol}^{-1}$ following manufacturer recommendations and performing a 30 min dialysis in a 2 liter bath of PBS twice. The final product was characterized using MALDI-TOF mass spectrometry. Empirically, we found that a fivefold molar excess of QSY 21 achieved a labeling ratio of $\sim 0.9\text{--}1.1$. In contrast, a 20-fold molar excess of QSY 21 yielded streptavidin with a labeling ratio of ~ 2 when using this method, based on UV-visible light absorbance measurements.

2.5.2 Synthesis and characterization of EGF-PEG conjugates

EGF was simultaneously labeled with a flexible biotinylated PEG linker (PEG₁₂ (Thermo Scientific), PEG₂₄ (Quanta Biodesign) or PEG₇₅ (Nanocs)) and fluorescent dye (Alexa Fluor 647 (Invitrogen)) in a single pot reaction using standard NHS bioconjugation chemistry. A monolabeled product for both PEG and dye was desired for quantitative experiments. The optimal reaction concentrations were empirically determined to be $120 \text{ }\mu\text{M}$ EGF, 0.1 M sodium bicarbonate and a fivefold molar excess of both the biotin-PEG NHS ester and the Alexa Fluor 647 NHS ester. The reaction was incubated on a rotating platform at room temperature for 30 min and purified using the Bio-Gel P6 resin (Bio-Rad). MALDI-TOF mass spectrometry and UV-visible light absorbance measurements were used to determine the overall EGF:PEG:dye ratio (data not shown). Mass spectrometry indicated that the predominant product under these reaction conditions had an EGF:PEG:dye ratio of 1:1:1. Note that other EGF:PEG:dye

stoichiometries existed in the sample, the most abundant of which was dual labeled with dye but not conjugated to the biotin-PEG anchor (1:0:2) and therefore would not adhere to the streptavidin-functionalized surfaces.

In some cases, EGF was labeled with biotinylated PEG₇₅ and Alexa Fluor 647 in a step-wise fashion. First, 10 μl of 1 M sodium bicarbonate was added to 100 μl of EGF (1 mg ml^{-1}), then 20-fold molar excess of Alexa Fluor 647 NHS ester was added and the reaction was allowed to proceed for 10 min at room temperature. Subsequently, a 15-fold molar excess of biotin-PEG₇₅ NHS ester was added to the reaction mixture and allowed to incubate for an additional 30 min. The reaction was purified using Bio-Gel P6 resin (Bio-Rad). The final labeling ratio of dye:protein, as measured by UV-visible light absorbance, was 0.8. The EGF that was used for the alkyl linker controls was labeled in a single-pot reaction with NHS-sulfo-LC-biotin (LC, long chain) (Pierce) and Alexa Fluor 647 NHS ester (Invitrogen). We added 20 μl of 1 M sodium bicarbonate to 200 μl of 1 mg ml^{-1} EGF, after which a 20-fold molar excess of both biotinylated linker and dye was added. After reagent addition, the reaction was incubated for 1 h at room temperature and inverted every 15 min to ensure mixing. The reaction mixture was subsequently purified with Bio-Gel P4 resin (Bio-Rad), yielding EGF with an Alexa Fluor 647 labeling ratio of 1.9.

2.5.3 Cell culture

HCC1143 cells were cultured in RPMI 1640 medium (Mediatech) supplemented with 10% FBS (Mediatech), HEPES (9.9 mM, Sigma), sodium pyruvate (1 mM, Sigma), l-glutamine (2.1 mM, Mediatech), penicillin G (100 IU ml^{-1} , Mediatech) and streptomycin (100 $\mu\text{g ml}^{-1}$, Mediatech) and were incubated at 37 °C with 5% CO₂. Cells

were passaged at 90–100% confluency and plated at a density of 50% using standard cell culture procedures. All experiments were conducted with HCC1143 cells that had been serum-starved for ~18 h.

2.5.4 Functionalization of glass substrate biosensors

Glass coverslips were functionalized based on literature precedent¹⁹. Briefly, glass coverslips (number 2, 25 mm diameter; VWR) were sonicated in Nanopure water (18.2 mΩ) for 10 min and then etched in piranha (a 3:1 mixture of sulfuric acid (Avantor Performance Materials) and 30% hydrogen peroxide (Sigma)) for 10 min (please take caution: piranha is extremely corrosive and may explode if exposed to organics). The glass coverslips were then washed six times in a beaker of Nanopure water (18.2 mΩ) and placed into three successive wash beakers containing EtOH (Decon Labs) and left in a final fourth beaker containing 1% (3-aminopropyl)triethoxysilane (APTES, Sigma) in EtOH for 1 h. The substrates were then immersed in the EtOH three times and subsequently rinsed with EtOH and dried under nitrogen. Substrates were then baked in an oven (~100 °C) for 10 min. After cooling, the samples were incubated with NHS-biotin (Thermo Fisher) at 2 mg ml⁻¹ in DMSO (dimethyl sulfoxide, Sigma) overnight. Subsequently, the substrates were washed with EtOH and dried under nitrogen. The substrates were then washed with PBS (three 5 ml aliquots) and incubated with BSA (EMD Chemicals, 100 µg µl⁻¹, 30 min) and washed again with PBS (three 5 ml aliquots). Quencher labeled streptavidin was then added (1 µg ml⁻¹, 45 min, room temperature) followed by washing with PBS (three 5 ml aliquots) and incubating with the desired EGF construct (biotinylated linker and fluorophore labeled, 1 µg ml⁻¹, 45 min, room temperature). Substrates were then rinsed with a final wash of PBS (three 5 ml aliquots)

and used within the same day. To verify that surfaces were stable within the experimental time frame, a substrate, functionalized as described above, was imaged over two consecutive days. The fluorescence intensity of the surface did not change greatly within this time frame (**Figure A2.13**).

2.5.5 Functionalization of supported lipid bilayers

Lipids consisted of 99.9% 1,2-dioleoyl-sn-glycero-3-phosphocholine (DOPC, Avanti Polar Lipids) and 0.1% 1,2-dioleoyl-sn-glycero-3-phosphoethanolamine-N-(cap biotinyl) (sodium salt) (DPPE-biotin, Avanti Polar Lipids). After being mixed in the correct proportions in chloroform, lipids were dried with a rotary evaporator and placed under a stream of N₂ to ensure complete evaporation of the solvent. These lipid samples were then resuspended in Nanopure water and subjected to three freeze-thaw cycles by alternating immersions in an acetone and dry ice bath and a warm water bath (40 °C). To obtain small unilamellar vesicle, lipids were extruded through a high-pressure extruder with a 100 nm nanopore membrane (Whatman)²⁰.

Supported lipid bilayers were assembled by adding small unilamellar vesicles to base-etched 96-well plates with glass-bottomed wells. At the biotinylated lipid doping concentration used (0.1%), the calculated streptavidin density was 690 molecules μm^{-2} , and therefore it is expected that streptavidin bound to the surface was at sufficiently low density to avoid fluorophore self-quenching²¹. This was confirmed by measuring fluorescence intensity as a function of biotin doping concentration (data not shown). After blocking with BSA (0.1 mg ml⁻¹) for 30 min, bilayer surfaces were incubated with either unlabeled streptavidin (1 μg 400 μl^{-1}) or streptavidin QSY 21 (1 μg 400 μl^{-1}) for 1 h. Wells were rinsed three times with 5 ml of PBS, then incubated with EGF-PEG_x-

Alexa Fluor 647 (100 nM) ($x = 12, 24$ or 75) for 1 h and rinsed three times with 5 ml of PBS before imaging.

2.5.6 Characterization of the zero-force sensor confirmation

FRET efficiency was measured using equation 2.1,

$$E = \left(1 - \frac{I_{DA}}{I_D} \right) \frac{1}{f_A}$$

Eqn. 2.1

where I_{DA} refers to the intensity of the EGF-PEG_x-Alexa Fluor 647 surface containing quencher labeled streptavidin, I_D is the intensity of the EGF-PEG_x-Alexa Fluor 647 surface with unlabeled streptavidin and f_A is the labeling ratio of the acceptor²². These values were obtained by averaging the fluorescence intensity measured in five different areas for each substrate. The reported values are the average of three independent experiments. The calculated efficiency for each surface was then used to determine the average distance between fluorophore and quencher by,

$$E = \frac{1}{1 + \left(\frac{r}{R_0} \right)^6}$$

Eqn. 2.2

where R_0 is the Förster distance of the dye pair (6.9 nm according to the manufacturer) and r is the average distance between the fluorophores²². The predicted value for r was determined by adding the PEG Flory radius to the radii of the proteins that comprise the force sensor. The protein radius for EGF was estimated at 1 nm based on its crystal structure (Protein Data Bank (PDB): 2KV4), and for streptavidin the radius was estimated at 2 nm based on the crystal structure (PDB: 1SWB). The predicted r value was

then compared to the FRET measured r value and reported in **Figure A2.13**.

2.5.7 Fluorescence microscopy

Live cells were imaged in serum-free RPMI 1640 (Mediatech) medium formulated as described in the cell culture section at 37 °C, and fixed cells were imaged in 1% BSA in PBS at room temperature. During imaging, physiological temperature was maintained with a warming apparatus consisting of a sample warmer and an objective warmer (Warner Instruments 641674D and 640375). The microscope used was an Eclipse Ti driven by the Elements software package (Nikon). The microscope features an Evolve electron multiplying charge-coupled device (CCD; Photometrics), an Intensilight epifluorescence source (Nikon) a CFI Apo 100x (numerical aperture (NA) 1.49) objective (Nikon) and a TIRF launcher with two laser lines: 488 nm (10 mW) and 640 nm (20 mW). This microscope also includes the Nikon Perfect Focus System, an interferometry-based focus lock that allowed the capture of multipoint and time-lapse images without loss of focus. The microscope was equipped with the following Chroma filter cubes: TIRF 488, TIRF 640, Cy5 and reflection interference contrast microscopy (RICM).

2.5.8 Image analysis

Images from sensor experiments were processed (using a custom macro in ImageJ (US National Institutes of Health)) from a single multipoint image file into individual tiff stacks containing each imaging channel. Separate macros were then used to isolate and background subtract the Alexa Fluor 647 EGF force channel. For all images, the LUT was linear and represented the full range of data as indicated by the calibration bar accompanying each image set. Analysis of images was performed with ImageJ and Nikon Elements software packages. ND2 image processing was done with several custom

ImageJ macros in combination with the LOCI bio-formats ImageJ plugin as well as the Nikon Elements software package. Sensor spot duration analysis was performed manually with the assistance of the SpotTracker 2D²³ and Multi Measure ImageJ plugins.

2.5.9 Quantitative force maps

To determine the absolute magnitude of forces detected by the sensor, a series of image operations were performed. First, the quenching efficiency image map was derived from the background subtracted TIRF 640 sensor signal image by using equation 2.3,

$$C = 1 - \frac{A}{B}$$

Eqn. 2.3

where A is the background-subtracted TIRF 640 sensor signal image, B is the average background-subtracted TIRF 640 image of a donor-only force probe obtained from a sample lacking the quencher and C is the resulting image which is a map of the quenching efficiency. Next, an image mapping the distance between the fluorophore and quencher was obtained by rearranging the FRET relation and applying equation 2.4,

$$D = R_0 \left(\frac{1}{C} - 1 \right)^{1/6}$$

Eqn. 2.4

where R_0 is the Förster radius of the quencher-fluorophore pair, and D is the resulting distance map²². This fluorophore-quencher distance image was then used to correct for the TIRF excitation intensity because the evanescent field intensity drops off exponentially in the z axis dimension. The penetration depth of the TIRF evanescent field was determined by equation 2.5,

$$d = \frac{\lambda}{4\pi\sqrt{n_2^2 \sin^2 \theta - n_1^2}}$$

Eqn. 2.5

where d is the penetration depth of the evanescent field, n_2 is the index of refraction of glass (1.51), n_1 is the index of refraction of water (1.33), λ is the wavelength (640 nm) and θ is the incident angle of the laser ($\sim 65^\circ$)²². The penetration depth can then be used along with the distance map to determine the corrected TIRF excitation intensity at each pixel. This is accomplished by applying equation 2.6

$$S = B e^{-D/d}$$

Eqn. 2.6

where S is the scalar correction image, B is the donor only averaged image, D is the distance map image and d is the penetration depth of the evanescent field. The product of multiplying S by B gives the illumination intensity corrected distance map, E . To determine the average PEG resting conformation, the dimensions of EGF and streptavidin were subtracted from the corrected distance map, E . To calculate the extension of PEG from this resting state, the PEG resting state conformation was subtracted from the entire image. Finally, a quantitative force map was inferred by applying the extended WLC model to the distance map. The extended WLC approximation is made by applying equation 2.7 to image E

$$\langle F \rangle = \frac{k_B T}{L_p} \left(\frac{E}{L} + \frac{1}{4 \left(1 - \frac{E}{L}\right)^2} - \frac{1}{4} + \sum_{i=2}^{i=7} \alpha_i \left(\frac{E}{L}\right)^i \right)$$

Eqn. 2.7

where F is the resulting quantitative force map image, k_B is the Boltzman constant, T is the temperature, L_p is the persistence length of PEG (0.38 nm), E is the corrected distance

map and L is the end-to-end length of PEG₂₄ (8.4 nm)¹⁶.

2.5.10 Determination of EGFR phosphorylation and activation

HCC1143 cells were seeded onto the biosensor surfaces displaying EGF and incubated on the substrates for 30 min at 37 °C. Following initial imaging, the cells were fixed with 4% paraformaldehyde (Sigma) in PBS and permeabilized with 0.1% Triton X (Sigma) in PBS. Cells were then blocked overnight in 1% BSA at 4 °C. The next day, cells were incubated with a primary antibody to EGFR-pTyr1068 (Cell Signaling Technologies 3777s) at 1:200 dilution for 1 h at room temperature. The primary antibody was then washed out with PBS and the cells were incubated with Alexa Fluor 488–labeled rabbit IgG secondary antibody (Invitrogen) at 1:1,000 dilution for 45 min. The secondary antibody was then rinsed out with PBS, and the sample was imaged in TIRF mode at 488 nm as well as in the Alexa Fluor 647, brightfield and RICM channels using an epifluorescence source.

2.5.11 Actin inhibition

HCC1143 cells were serum-starved for ~18 h and split into two aliquots, one of which was treated with 4 μm latrunculin B (Sigma) for 30 min in DMSO (EMD Chemicals), and the other was treated with an equivalent amount of DMSO. Each aliquot was then plated onto an EGF-functionalized biosensor surface and incubated for 30 min at 37 °C. Cells were then imaged in the Alexa Fluor 647, brightfield and RICM channels.

2.5.12 CLC-eGFP transfection

HCC1143 cells were seeded on a 24-well plate in antibiotic-free media at a density of ~300,000 cells per well overnight. The cells were then transfected with the CLC-eGFP construct using Lipofectamine 2000 (Invitrogen) and following standard

transfection protocols. These cells were then serum-starved overnight and used for experiments as indicated within 24 h of the transfection.

2.6 References

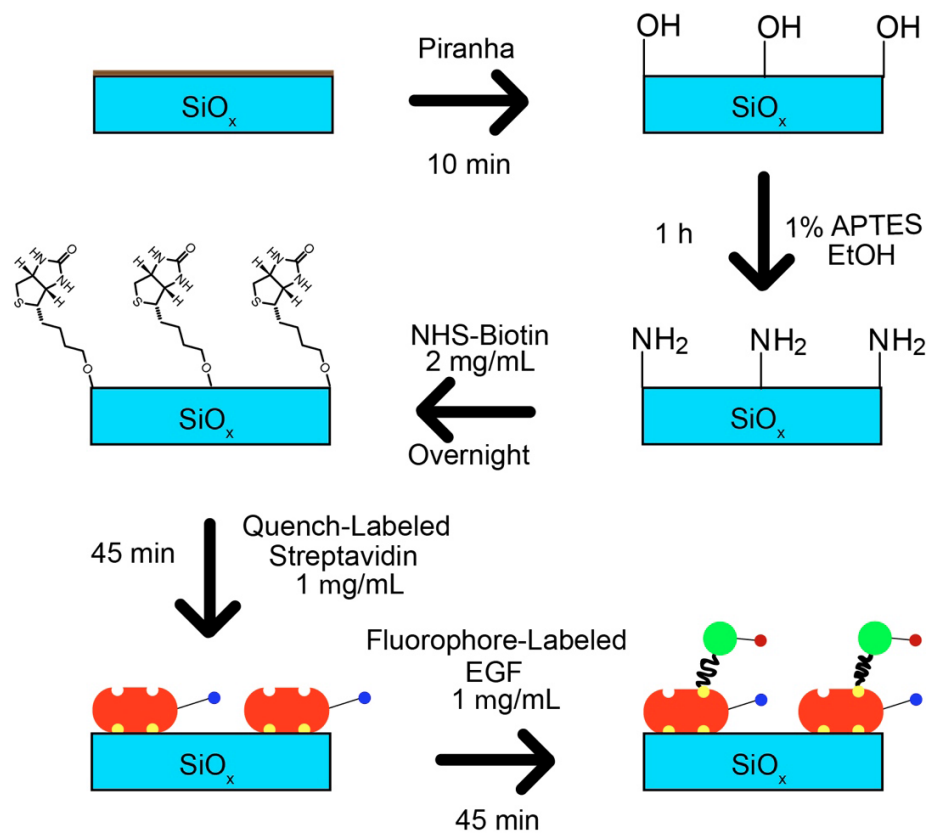
1. Vogel, V. & Sheetz, M. Local force and geometry sensing regulate cell functions. *Nat. Rev. Mol. Cell Biol.* **2006**, *7*, 265-275.
2. DuFort, C.C., Paszek, M.J. & Weaver, V.M. Balancing forces: architectural control of mechanotransduction. *Nat. Rev. Mol. Cell Biol.* **2011**, *12*, 308-319.
3. Dufrene, Y.F. et al. Five challenges to bringing single-molecule force spectroscopy into living cells. *Nat. Methods* **2011**, *8*, 123–127.
4. Muller, D.J., Helenius, J., Alsteens, D. & Dufrene, Y.F. Force probing surfaces of living cells to molecular resolution. *Nat. Chem. Biol.* **2009**, *5*, 383 - 390.
5. Grashoff, C. et al. Measuring mechanical tension across vinculin reveals regulation of focal adhesion dynamics. *Nature* **2010**, *466*, 263-266.
6. Iwai, S. & Uyeda, T.Q.P. Visualizing myosin–actin interaction with a genetically-encoded fluorescent strain sensor. *Proc. Natl. Acad. Sci. U.S.A.* **2008**, *105*, 16882-16887.
7. Meng, F. & Sachs, F. Visualizing dynamic cytoplasmic forces with a compliance-matched FRET sensor. *J. Cell Sci.* **2011**, *124*, 261-269.
8. Oesterhelt, F., Rief, M. & Gaub, H.E. Single molecule force spectroscopy by AFM indicates helical structure of poly(ethylene-glycol) in water. *New J. Phys.* **1999**, *1*, 6.1-6.11.

9. Kienberger, F. et al. Static and dynamical properties of single poly(ethylene glycol) molecules investigated by force spectroscopy. *Single Molecules* **2000**, *1*, 123-128.
10. Roberts, M.J., Bentley, M.D. & Harris, J.M. Chemistry for peptide and protein PEGylation. *Adv. Drug Deliv. Rev.* **2002**, *54*, 459-476.
11. Harder, P., Grunze, M., Dahint, R., Whitesides, G.M. & Laibinis, P.E. Molecular Conformation in Oligo(ethylene glycol)-Terminated Self-Assembled Monolayers on Gold and Silver Surfaces Determines Their Ability To Resist Protein Adsorption. *J. Phys. Chem. B* **1998**, *102*, 426–436.
12. Goh, L.K., Huang, F., Kim, W., Gygi, S. & Sorkin, A. Multiple mechanisms collectively regulate clathrin-mediated endocytosis of the epidermal growth factor receptor. *J. Cell Biol.* **2010**, *189*, 871-883.
13. Martin, A.C., Welch, M.D. & Drubin, D.G. Arp2/3 ATP hydrolysis-catalysed branch dissociation is critical for endocytic force generation. *Nat. Cell Biol.* **2006**, *8*, 826 - 833.
14. Salaita, K. et al. Restriction of Receptor Movement Alters Cellular Response: Physical Force Sensing by EphA2. *Science* **2010**, *327*, 1380-1385.
15. de Gennes, P.G. Conformations of Polymers Attached to an Interface. *Macromolecules* **1980**, *13*, 1069-1075.
16. Bouchiat, C. et al. Estimating the persistence length of a worm-like chain molecule from force-extension measurements. *Biophys. J.* **1999**, *76*, 409-413.
17. Sulchek, T.A. et al. Dynamic force spectroscopy of parallel individual Mucin1–antibody bonds. *Proc. Natl. Acad. Sci. U.S.A.* **2005**, *102*, 16638-16643.

18. Saffarian, S., Cocucci, E. & Kirchhausen, T. Distinct Dynamics of Endocytic Clathrin-Coated Pits and Coated Plaques. *PLoS Biol.* **2009**, *7*, e1000191.
19. Clack, N.G., Salaita, K. & Groves, J.T. Electrostatic readout of DNA microarrays with charged microspheres. *Nat. Biotech.* **2008**, *26*, 825-830.
20. Nair, P.M., Salaita, K., Petit, R.S. & Groves, J.T. Using patterned supported lipid membranes to investigate the role of receptor organization in intercellular signaling *Nat. Protocols* **2011**, *6*, 523-539
21. Galush, W.J., Nye, J.A. & Groves, J.T. Quantitative fluorescence microscopy using supported lipid bilayer standards. *Biophys. J.* **2008**, *95*, 2512-2519.
22. Lakowicz, J.R. Principles of Fluorescence Spectroscopy, Edn. 3rd edn. (Springer, New York; 2006).
23. Sage, D., Neumann, F.R., Hediger, F., Gasser, S.M. & Unser, M. Automatic Tracking of Individual Fluorescence Particles: Application to the Study of Chromosome Dynamics. *IEEE Trans. Image Process.* **2005**, *14*, 1372-1383.

Appendix 2

a



b

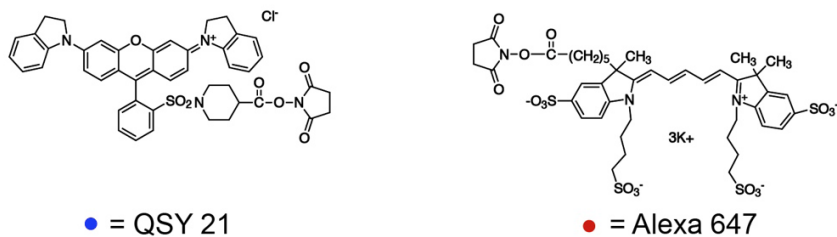


Figure A2.1 Fabrication of glass surface-functionalized force sensors.

(a) Schematic describing the steps used to generate the force biosensors. See methods section for detailed description. (b) Molecular structures of the reactive NHS esters of QSY 21 and Alexa 647.

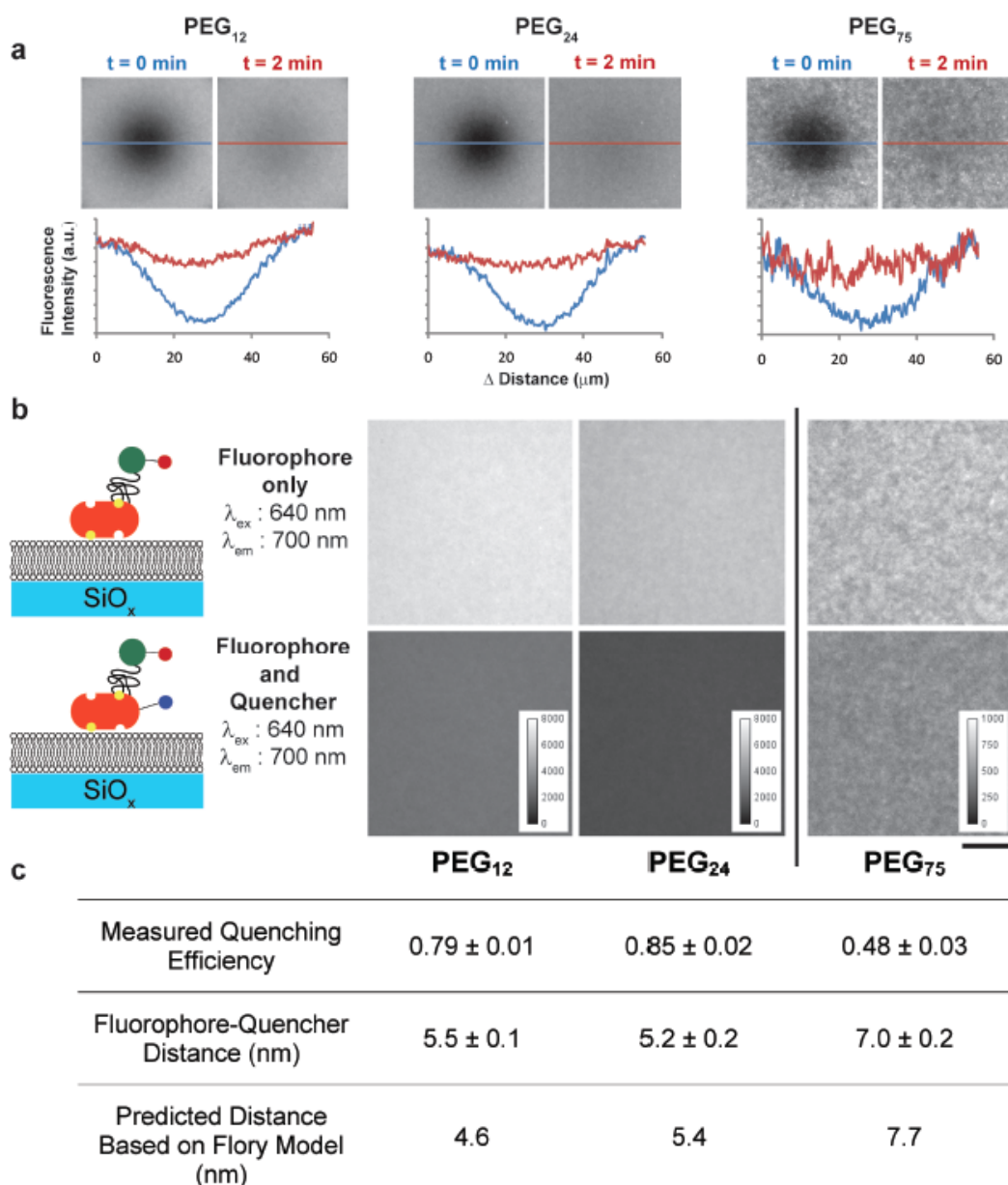


Figure A2.2 Zero-force conformation of the sensor. (a) The force sensor surfaces are laterally fluid as indicated by FRAP (fluorescence recovery after photobleaching) experiments. Line plots show the fluorescence intensity immediately after photobleaching (blue) and the fluorescence intensity after 2 min of recovery time (red). (b) The resting state of EGF-PEG₁₂, EGF-PEG₂₄, and EGF-PEG₇₅ sensors was determined by measuring the fluorescence intensity of surfaces containing the sensor in the absence (top row) and in the presence (bottom row) of the quencher. (c) The quenching efficiency for each surface was then calculated, and the experimental distance between chromophores in the resting state was determined and compared to the distance calculated from the Flory radius of each PEG polymer (see methods for calculation details). All measurements were taken in PBS at RT. Error represents s.e.m. of three independent pairs of samples ($n = 3$) that were imaged at a minimum of five different locations each. Scale bar is 10 μm .

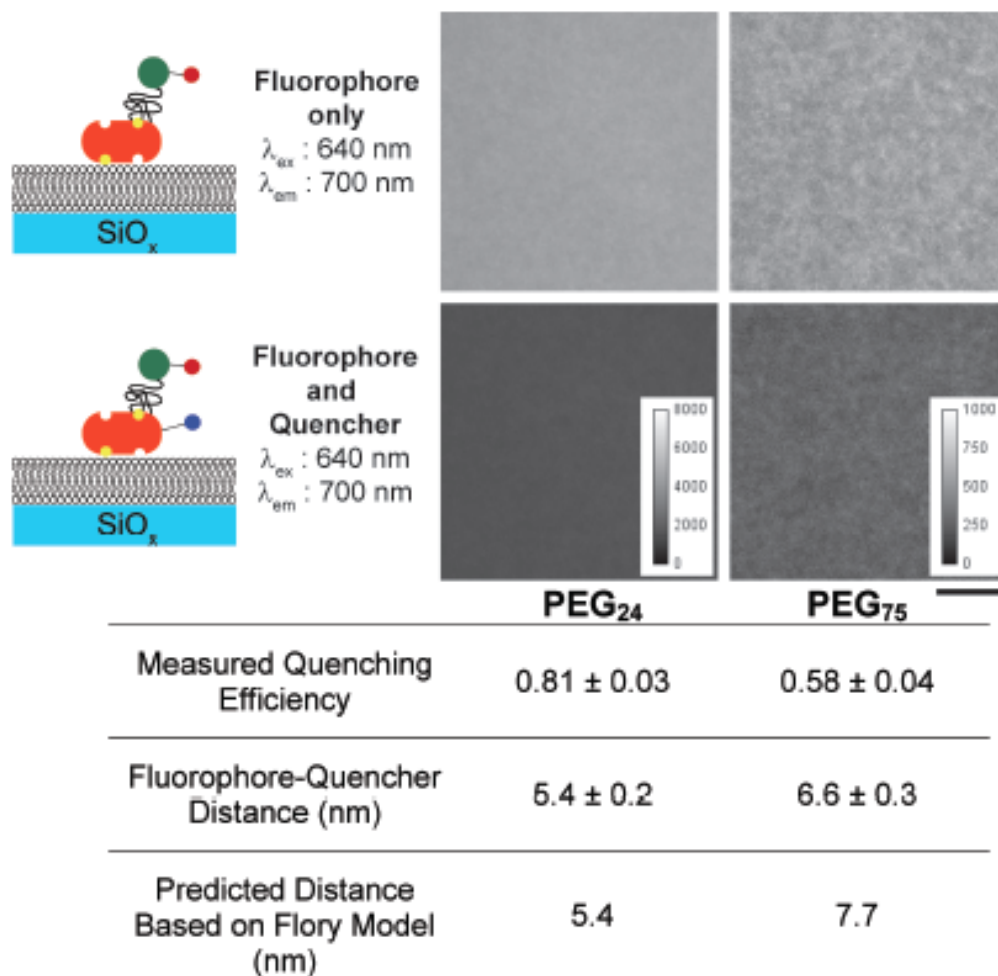


Figure A2.3 Zero-force conformation of the sensor at physiological conditions. Representative fluorescence images of the EGF-PEG₂₄ and EGF-PEG₇₅ force sensor surfaces that were generated either with labeled or unlabeled streptavidin. The PEG sensor conformation was determined using **Eqn. 2.1** and **Eqn. 2.2** as described in **Figure A2.2**. The conformation of the sensor at 37 °C is similar to that shown previously for the sensor at 25 °C (**Figure A2.2**). Error represents the standard deviation of intensity measurements from ten different areas across two separate surfaces. Scale bar is 10 μm .

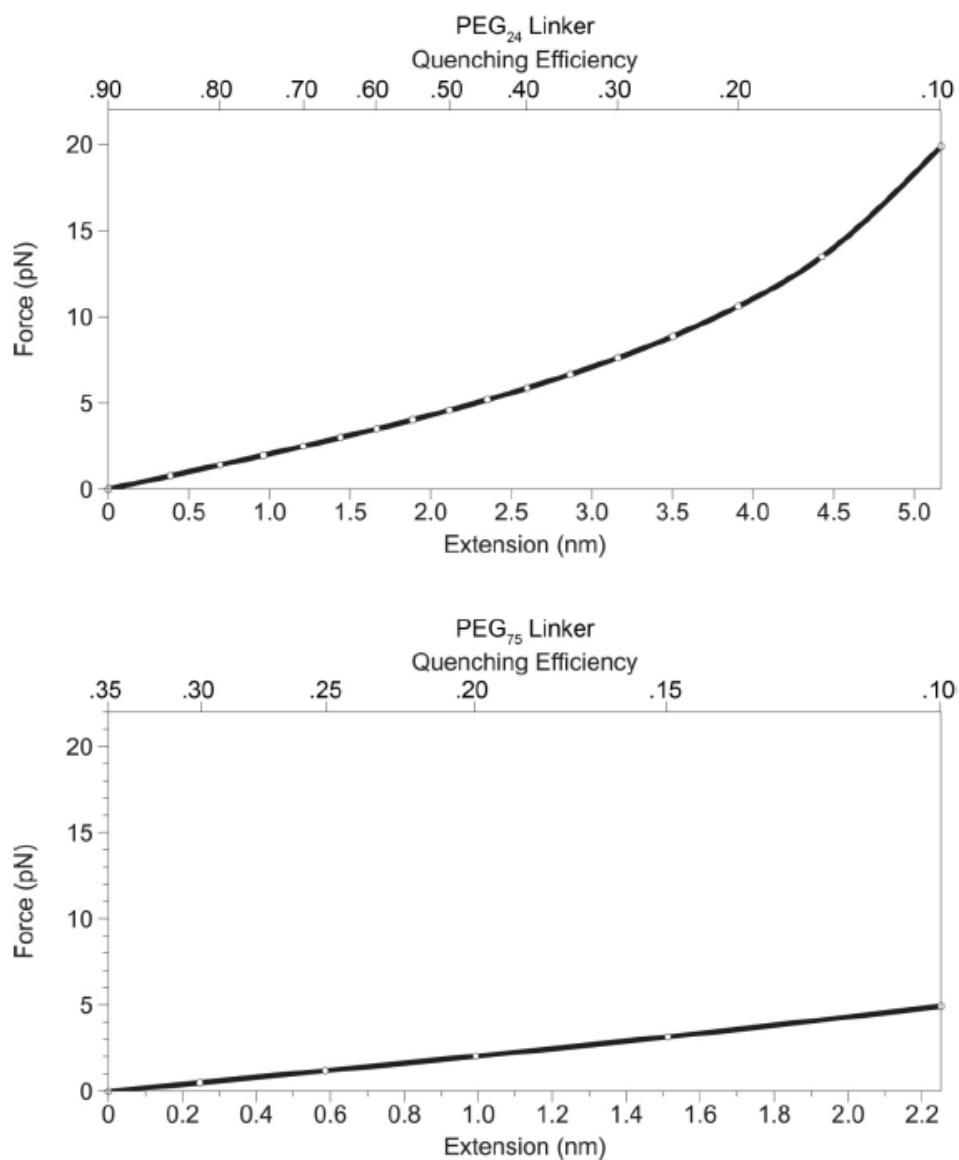


Figure A2.4 Theoretical plots of PEG₂₄ and PEG₇₅ extension and quenching efficiency as a function of applied force. The extended worm-like chain model (WLC) was used to generate a plot of the applied forces as a function of linker displacement, which is calculated from quenching efficiency (Eqn. 2.3-2.7). A range of quenching efficiencies from 10% to 90% was converted into PEG extension lengths using the FRET relation for the QSY 21 Alexa 647 quencher-fluorophore pair (Eqn. 2.4). The zero force resting state distance between the chromophores was calculated by subtracting the resting state of the polymer and the dimensions of the EGF and streptavidin proteins from the simulated distances. The resting state of the PEG₂₄ linker was determined experimentally and corresponds to the polymer length at 90% quenching efficiency, while the PEG₇₅ linker resting state was determined from the Flory model. The displacement from this resting state distance was then converted into a force using the extended WLC model. The PEG₂₄ linker displays a wider dynamic range compared to PEG₇₅ given the polymer conformations and the Förster radius of the QSY 21 and Alexa 647 pair.

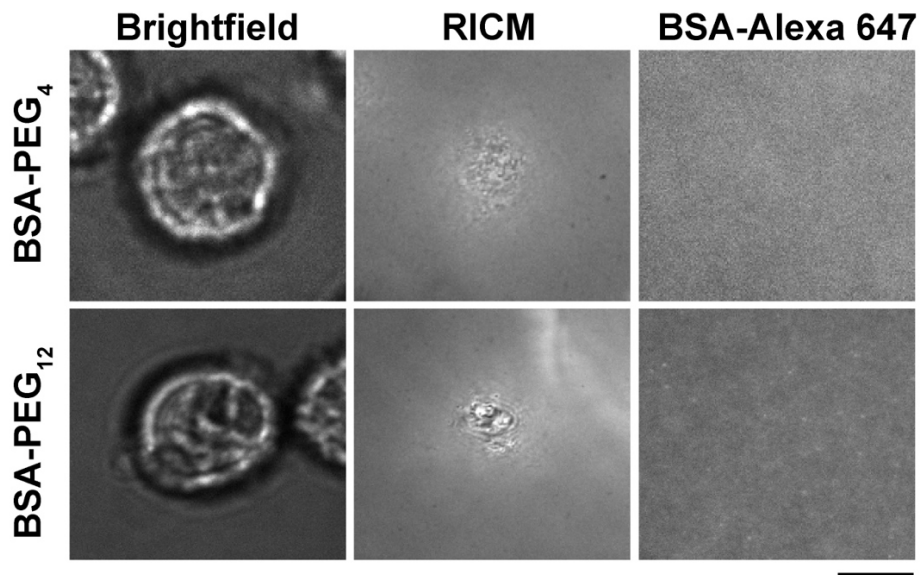


Figure A2.5 Specific EGF-EGFR interactions are required to activate the force sensor. Representative brightfield, RICM, and epifluorescence images of two cells on the indicated force sensor SLB surface (at $t = 30$ min). The fluorescence channel does not show any localized increases in signal, thus suggesting that a specific ligand-receptor interaction is necessary for force sensor activation. Scale bar is $10 \mu\text{m}$.

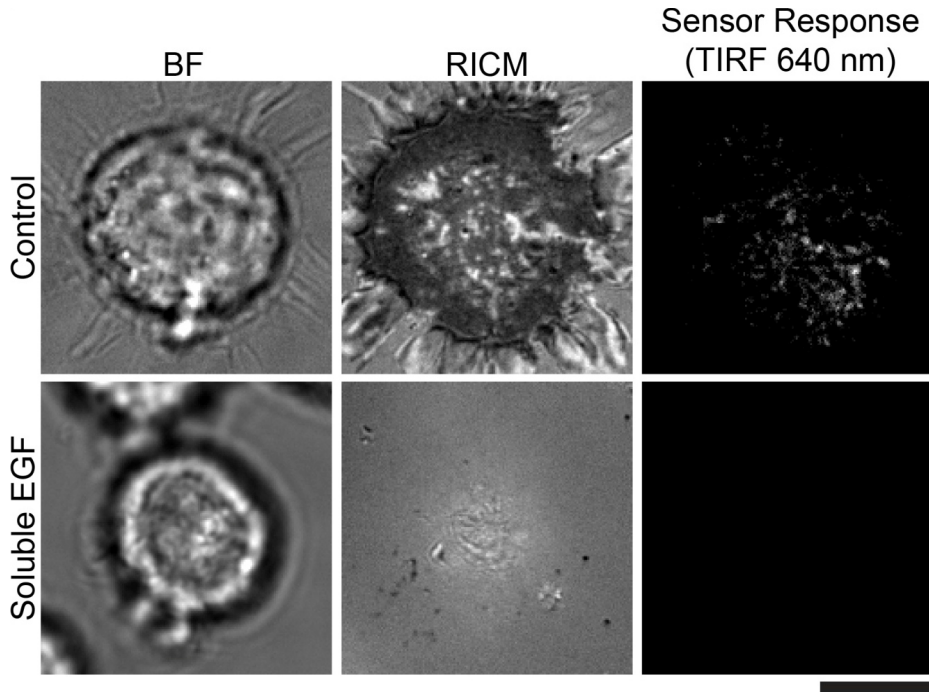


Figure A2.6 Force Sensor response requires a specific ligand-receptor interaction. Cells were plated on an EGF functionalized sensor surface either in the presence or absence of soluble EGF ligand (1.7 nM). Cells treated with soluble EGF exhibited poor adhesion to the surface and did not trigger a force sensor response, whereas control cells

adhered strongly and generated the characteristic response. This indicates that the force sensor response is primarily mediated by the EGF-EGFR interaction. Scale bar is 10 μm .

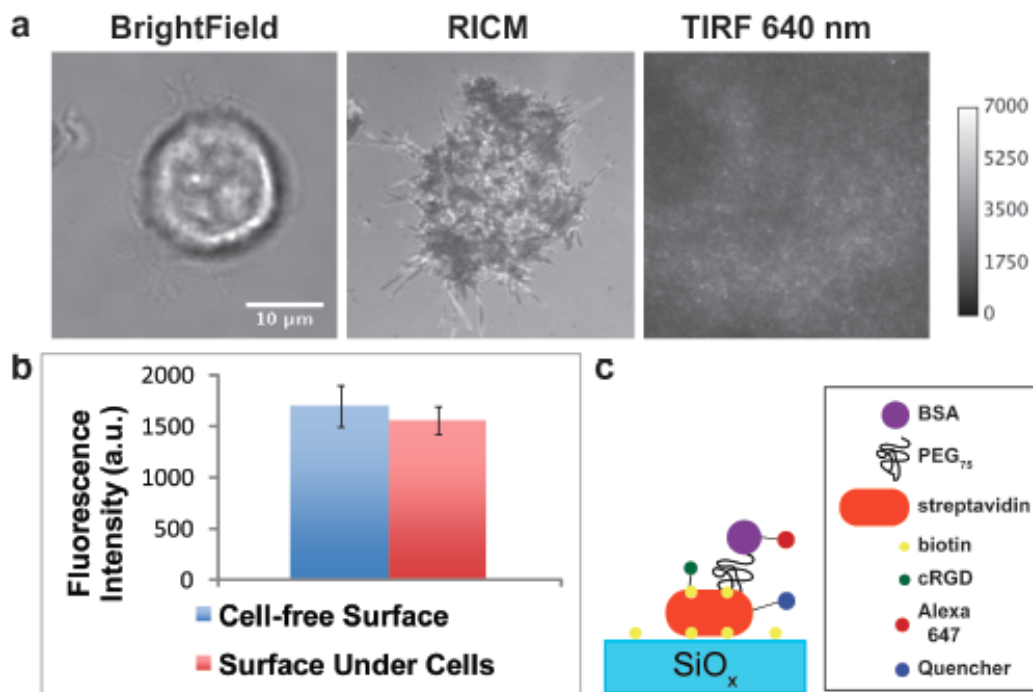


Figure A2.7 Specific EGF-EGFR interactions are required to activate the force sensor: role of apposed ligand. Brightfield, RICM, and TIRF (640 nm) images of a representative cell plated on a force sensor functionalized glass substrate. Cyclic RGD peptide (10 nM, Peptides Int'l) and BSA-PEG₇₅-Alexa 647 (15 nM) were co-adsorbed to the surface in order to provide two apposing ligands. The cRGD peptide engages integrins and enhances adhesion while the BSA provides a control force sensor ligand. The brightfield and RICM images (a) indicate that the cells are engaged to the surface. The TIRF image does not show any observable localized increases in signal, thus confirming that a specific ligand-receptor interaction is necessary for force probe response. (b) Comparison of the fluorescence intensities observed for the blank sensor surface with the area under the cells does not show a significant difference. Analysis represents the average of 10 cells. Error bars represent standard deviation. (c) Scheme depicting the BSA control force sensor.

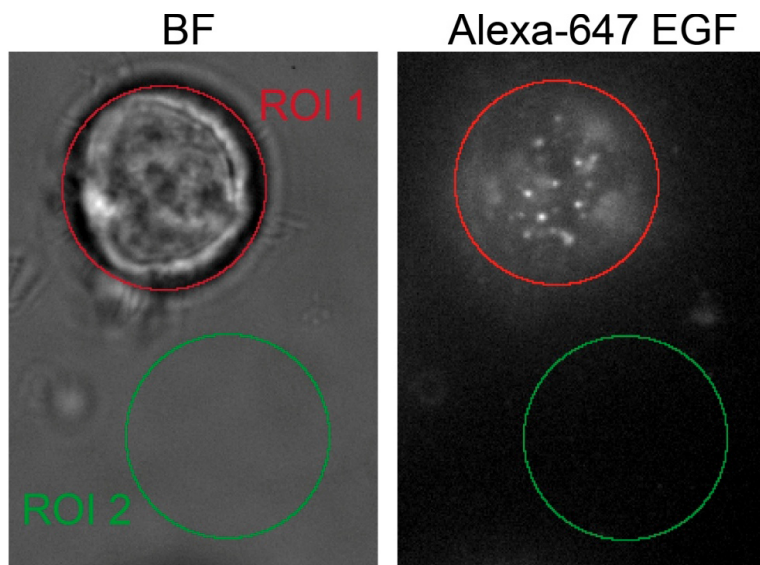


Figure A2.8 Data analysis of force sensor response.

Using the brightfield images as a guide, each Alexa 647 EGF image is analyzed by placing a circular region of interest (ROI) over the area of a cell (ROI 1 (red) in images) as well as placing an ROI over an off-cell area (ROI 2 (green) in images). The average intensity of the fluorescence signal in each ROI is measured, and the mean intensity of ROI 1 is divided by the mean intensity of ROI 2. This is repeated for many cells, and the quotients are averaged into a mean, generating the normalized fluorescence increase values used in plots. The error reported is that of the measured quotients.

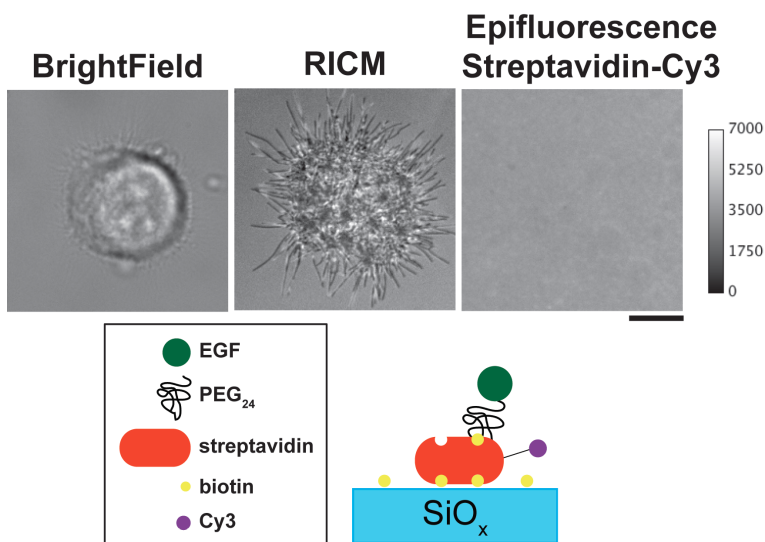


Figure A2.9 Cell binding does not induce clustering of sensor.

HCC1134 cells were incubated for 30 min on surfaces functionalized with EGF-PEG₂₄-streptavidin-Cy3. Brightfield and RICM images show that the cell engaged the surface. Fluorescence images of the Cy3 channel do not show any observable clustering, which confirms that the streptavidin is immobile on the glass substrate. Scale bar is 10 μ m.

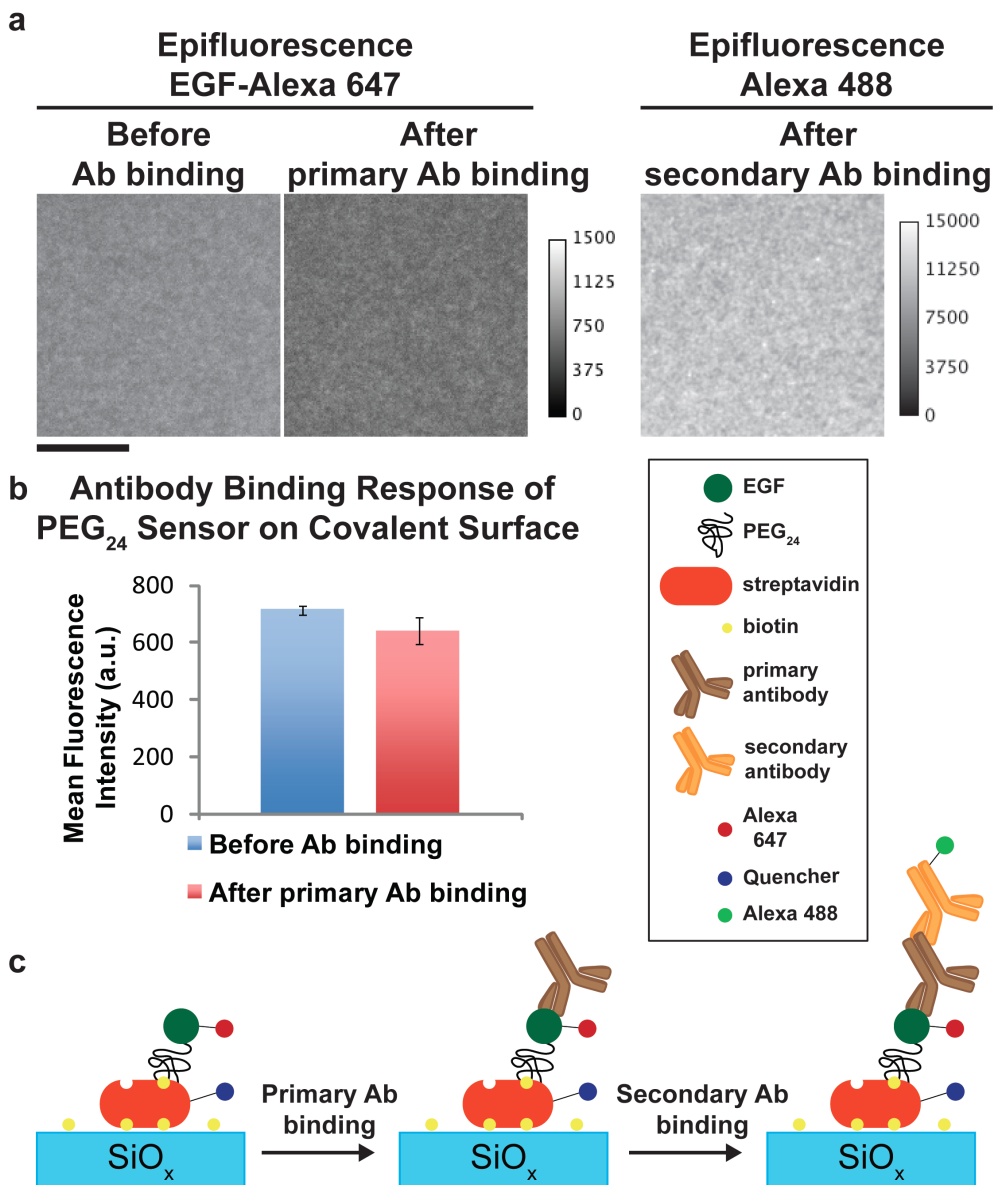


Figure A2.10 Binding of EGF antibody to EGF ligand does not trigger the force sensor. Surfaces were covalently functionalized with the force sensor containing EGF ligand as described previously. (a) Representative fluorescence images of the force sensor surface before and after binding of primary EGF antibody ($5 \mu\text{g ml}^{-1}$, R&D Systems). To confirm binding of antibody to the surface, the primary antibody surfaces were incubated with secondary IgG antibody-Alexa 488 ($2.5 \mu\text{g ml}^{-1}$, Invitrogen). Scale bar is $10 \mu\text{m}$. (b) Bar graph showing the mean fluorescence intensity of force sensor surface before (blue) and after (red) addition of the primary antibody. Error represents the standard deviation of 10 different regions on each surface. (c) Scheme depicting the predicted antibody binding to the force sensor surface.

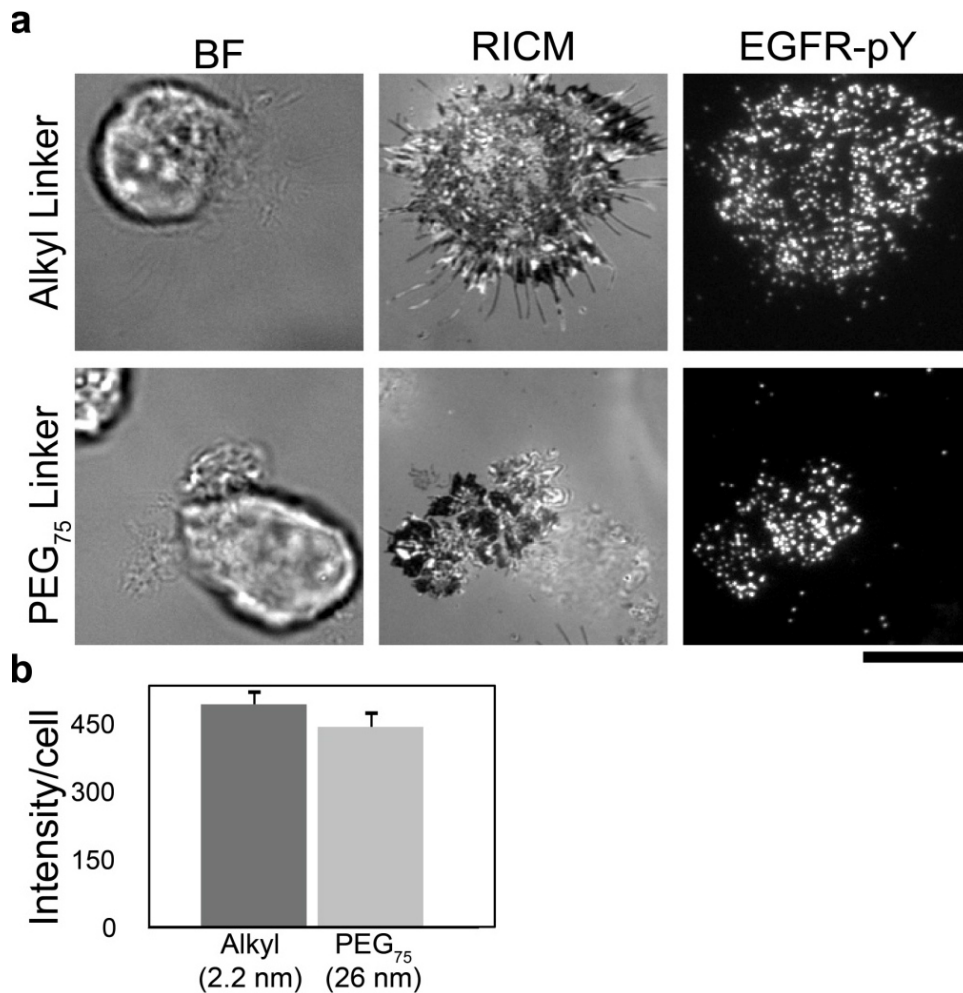


Figure A2.11 The activity of EGF ligand is independent of linker length. HCC1143 cells were serum starved for 18 h and plated onto sensor surfaces in supplemented RPMI media at 37 °C and incubated for approximately 30 min, after which cells were imaged live (see methods for imaging details). (a) Representative brightfield, images of two cells that were incubated onto the indicated sensor surface and then fixed and stained with anti-EGFR-pY 1068 antibody (Cell Signaling Technologies 3777s). Scale bar is 12 μ m. (b) Graph showing the average background-subtracted fluorescence intensity of cells immunostained for EGFR-pY 1068. Intensity indicates the level of receptor phosphorylation remains similar for both the alkyl and PEG₇₅ linkers. Error bars represent the standard error of the mean (s.e.m.), alkyl, n = 52 cells; PEG₇₅, n = 47 cells.

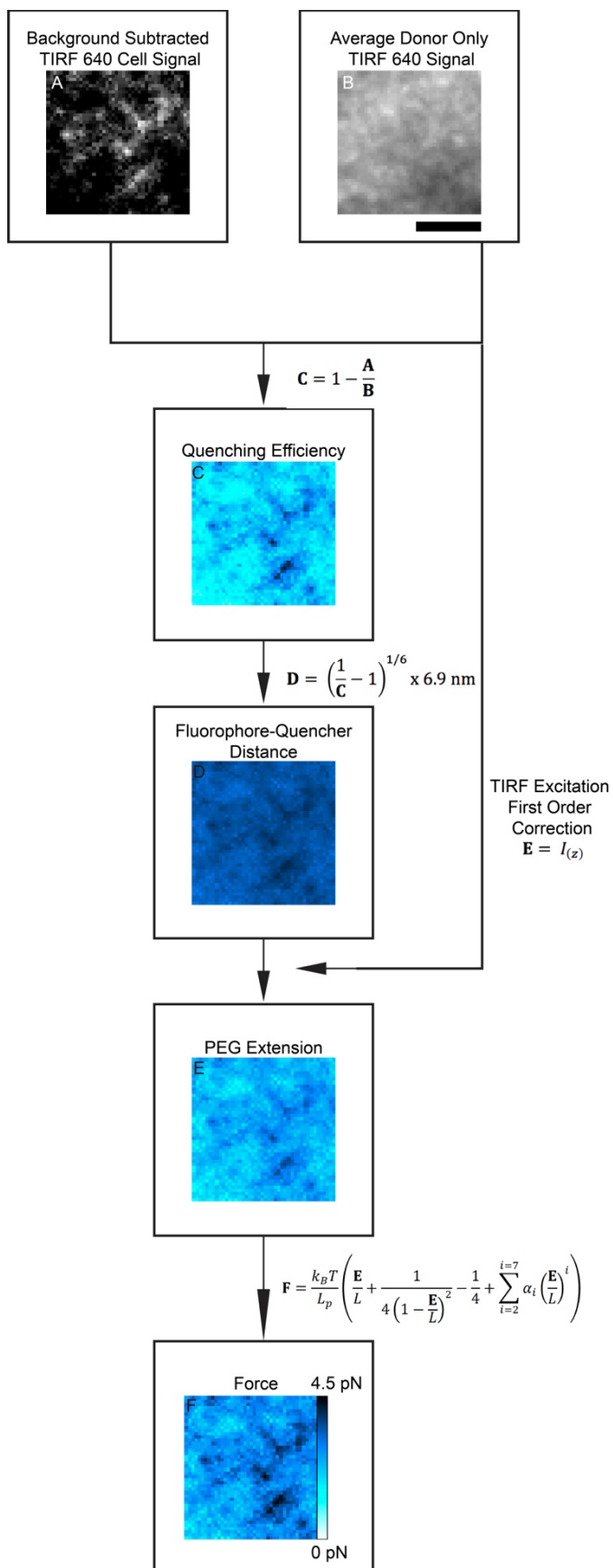


Figure A2.12 Flow chart of data analysis for converting quenching efficiency to force maps. In order to quantify the forces detected by the sensor, a series of image operations were performed. First, the background subtracted TIRF 640 image (A) was divided by a composite donor only signal image (B) to generate a quenching efficiency image map (C). Note that (B) is an average of the signal over five regions of the donor only sample. The quenching efficiency map is then converted to a distance map (D) using the FRET relationship. This distance map is then used to perform a first order correction for TIRF excitation intensity falloff (see **Eqn. 5** and **Eqn. 6** in Methods and Materials). After the dimensions of EGF, streptavidin, and the resting state of the polymer were subtracted out, the z extension of PEG was mapped (E). This extension image was then converted to force (F) using the extended WLC model (see online methods for more details). Note that the false-color intensity values represent an ensemble average force for each pixel, and that this is the lower bound of the applied force. Scale bar is 3.2 μm .

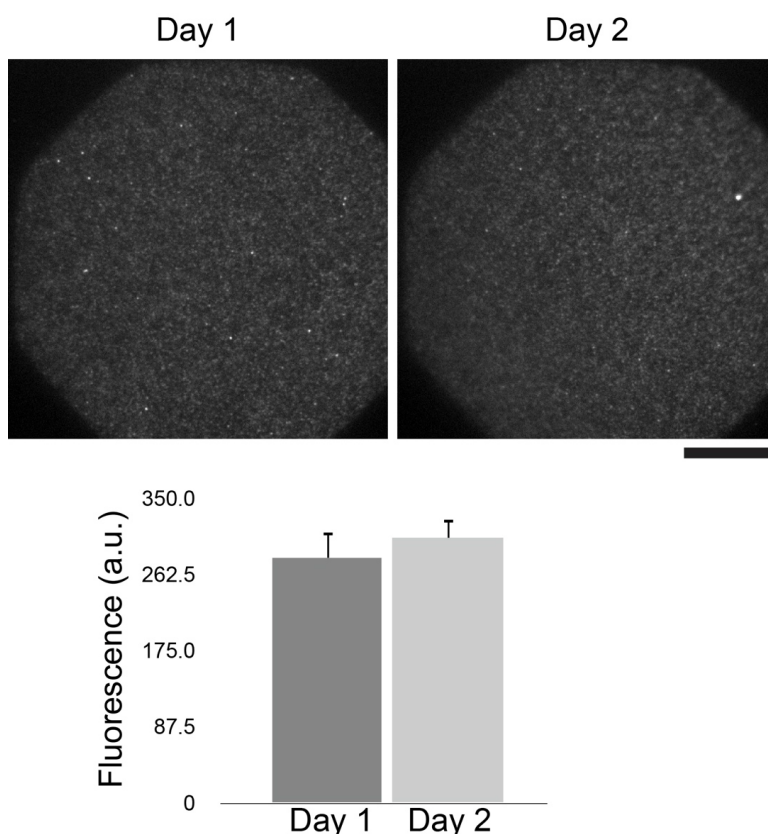


Figure A2.13 Stability of the sensor as a function of time.

A sensor surface featuring Alexa 647 labeled EGF and QSY 21 labeled streptavidin was prepared and then imaged over the course of two days. There was no significant change in the fluorescence intensity after 24 hours, indicating that the quencher is stable over the span of experimental time scales. Scale bar is 20 μm . Error represents the s.e.m. of three regions for each surface.

Chapter 3: Integrin-generated forces lead to streptavidin-biotin unbinding in cellular adhesions

Adapted from Jurchenko, C.; Chang, Y.; Narui, Y.; Salaita, K.S. Integrin-generated forces lead to streptavidin-biotin unbinding in cellular adhesions *Biophys. J.* **2014**, *106*, 1436-1446, used with permission.

3.1 Introduction

3.1.1 Mechanotransduction in the integrin pathway

In multicellular organisms, the task of sensing and transducing mechanical signals across the lipid membrane is primarily mediated through the integrin family of receptors, which are heterodimeric proteins composed of α - and β - subunits spanning the cell membrane¹. There has been intense effort aimed at better understanding how these receptor molecules probe mechanical and chemical cues within the surrounding extracellular matrix (ECM) and convert molecular tension into chemical signals². In general, integrin activation results in recruitment of adaptor proteins, such as talin and vinculin, which link the filamentous actin (F-actin) cytoskeleton to integrin receptors and trigger the formation of supramolecular focal adhesion structures responsible for signaling to downstream effectors. Increased mechanical tension generally stimulates the growth and assembly of focal adhesions³. However, tension can also lead to the disassembly of focal adhesions at the receding edge of a cell, thus allowing for processes such as cell migration⁴. Therefore, integrins display complex mechanochemical responses and, in the absence of methods to directly image single molecule tension within integrin-ligand complexes, the interplay between chemical and physical signals will remain difficult to fully understand, particularly in light of recent evidence for oscillatory force behavior within focal adhesions⁵, as well as the observation of a minimum force requirement for cell adhesions⁶.

3.1.2 Methods for studying adhesion forces

Two main methods are widely used to estimate the forces that cells generate against their surrounding matrix environment. The first, which is called traction force

microscopy, relies on culturing cells on soft compliant polymer films (polyacrylamide gels, for example) that deform under tension⁷. These deformations are then deconstructed using computational finite element analysis to calculate the lateral force vectors applied to micrometer elements. Using this method, the literature estimate for integrin tension within focal adhesions is approximately 2-3 pN per receptor⁸. This is a computationally intensive and challenging approach given the uncertainty of deformation in the regions between each element. A second approach uses arrays of polydimethylsiloxane polymer microneedles, with known spring constant, that bend in response to lateral cell forces⁹. In these methods, optical microscopy tracks microscopic substrate deformations to generate lateral force maps across entire cells, thus enabling the vast majority of quantitative measurements of cell-matrix interactions. Nonetheless, quantifying substrate deformation is indirect and the inherent bulk nature of these probes obscures the molecular, temporal, and spatial details of integrin tension that underpin biochemical signaling. Given that tension is exerted through individual integrin receptors, molecular force sensors with pN sensitivity are needed to better characterize mechanotransduction pathways in living cells¹⁰.

We recently invented a technique termed molecular tension-based fluorescence microscopy (MTFM) to image the forces exerted by cell surface receptors¹¹. MTFM uses a probe molecule composed of a discrete polyethylene glycol (PEG) linker flanked by a fluorophore and a quencher that undergo fluorescence resonance energy transfer (FRET), or nanosurface energy transfer, and thus report on the overall conformation of the PEG linker. The surface grafted PEG chain adopts a predictable and quantifiable mushroom conformation¹², and whereas one terminus is anchored to a surface, the other

terminus is modified with a ligand that binds to a specific cell surface receptor. Consequently, the PEG chain will reversibly extend from its relaxed conformation in response to mechanical tension exerted by receptor molecules. In its initial proof-of-concept demonstration, the head of the MTFM PEG chain was conjugated to the epidermal growth factor, which was fluorescently tagged, whereas the PEG tail was anchored to a surface using biotin bound to quencher-modified streptavidin. Because the fluorophore concentration remains fixed and is non-mobile, FRET efficiency values are determined solely by the donor emission intensity in the presence and absence of acceptor. Therefore, only a conventional fluorescence microscope is needed to visualize the forces applied between a specific receptor and its cognate ligand. More recently, we demonstrated the flexibility of MTFM by tethering the probes to the surface of gold nanoparticles and employed nanosurface energy transfer readout to image integrin cell traction forces¹³. To the best of our knowledge, MTFM¹¹ and recently reported variants^{13, 14} provide the only reported method to visualize pN molecular forces exerted between cell surface receptors and their ligands.

In this chapter, we investigate the use of FRET-based MTFM to image integrin receptor-mediated tension in living cells (**Figure 3.1a**). By generating three different MTFM integrin probes and running an array of controls, we found that integrin receptors exert forces sufficient to dissociate streptavidin-biotin complexes, the highest affinity noncovalent interaction in nature¹⁵. These findings are important because a), to the best of our knowledge, this is the first report of a protein-ligand interaction that is apparently stronger than the streptavidin-biotin association; b), it suggests that integrin receptors exert molecular forces much larger than had been predicted or reported previously; and

c), these results show that isolated single molecule measurements can drastically diverge from results obtained using biomolecules within their native supramolecular environment. In general, these results underscore the need for using MTFM to study the diverse cellular and mechanoregulatory processes that occur at the cell membrane.

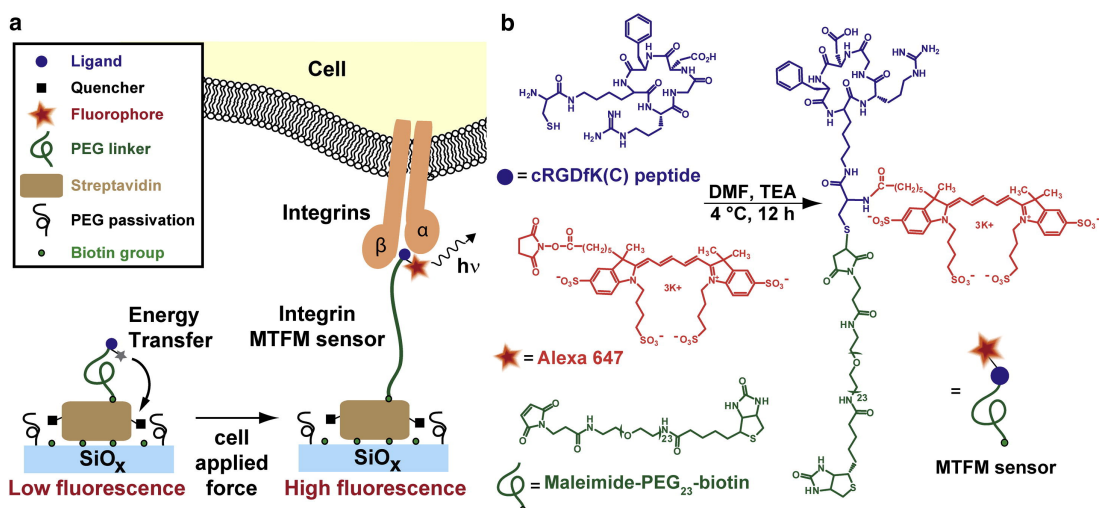


Figure 3.1 (a) Schematic of the MTFM integrin force sensor, which is composed of a PEG polymer flanked by a peptide and the fluorophore Alexa 647 at one terminus, and a quencher-modified streptavidin protein at the other terminus. In principle, we anticipated that mechanical tension applied through integrin receptors would extend the PEG linker and increase fluorescence. (b) Synthetic scheme showing the preparation of the cRGDfK(C)-A647-PEG₂₃-biotin conjugate.

3.2 Design and synthesis of MTFM sensor

To measure mechanical tension across the integrin receptor, we synthesized and characterized an integrin-specific MTFM sensor (**Figure 3.1a**). First, a cRGDfK(C) peptide, a common motif in ECM proteins, which shows high affinity ($K_D \sim \text{nM}$) toward the $\alpha_v\beta_3$ integrin receptor ($\alpha_v\beta_3 \gg \alpha_5\beta_1, \alpha_v\beta_5$)^{16, 17} was custom synthesized to include a cysteine residue bound to the ϵ -amine of lysine. Addition of the cysteine allowed orthogonal conjugation of a 23 unit PEG-biotin through a maleimide group via Michael addition and an Alexa 647 fluorescent dye via standard NHS ester chemistry (**Figure**

3.1b). The cRGDfK(C)-A647-PEG₂₃-biotin final product was purified and characterized by RP-HPLC and MALDI-TOF mass spectrometry (**Figure A3.1**). Of importance, this general strategy may be used for orthogonal and site-specific conjugation of a vast array of peptide and small molecule ligands, thus allowing one to investigate biophysical forces exerted by many receptors of interest.

3.3 Surface characterization and density calibration

Given that a sufficient ligand density is required for receptor clustering and activation¹⁸, and polymer density influences the MTFM sensor conformation (and thus sensor response), it was important that we first measure and tune the surface density of the cRGDfK(C) MTFM sensors. To measure the donor only and donor-acceptor intensity from identical surfaces, we synthesized a cRGDfK(C)-QSY21-PEG₂₃-biotin conjugate (**Figure A3.2**) and anchored this to a streptavidin-Alexa 647 monolayer that was immobilized onto a standard glass coverslip (**Figure A3.3**). The peptide surface density was controlled by modifying glass coverslips with binary mixtures of APTES and mPEG, where the terminal amine group of APTES was reacted with an NHS-ester biotin to capture streptavidin-Alexa 647, whereas the mPEG passivates the surface against nonspecific protein adsorption. To confirm the strength of binding between streptavidin and the biotinylated MTFM probes, the k_{off} of biotin dissociation in the presence of free biotin was measured (**Figure A3.4**) and was found to be similar to that reported in the literature^{19,20}. Moreover, we determined that nonspecific binding of streptavidin and the PEG ligand contributed <0.5% of total bound MTFM probes (**Figure A3.5**), thus confirming that the MTFM sensor was immobilized specifically through streptavidin-biotin interactions. To quantify the molecular surface density, we calibrated the Alexa

647 fluorescence intensity using a standard set of supported lipid membranes (**Figure A3.6** and Methods)^{21,22}. Based on this quantitative fluorescence calibration, we found that APTES:mPEG ratios of 1:0, 1:1, 1:10, 1:100, and 1:1000 resulted in streptavidin surface densities of 5300, 4600, 4400, 520, and 17 molecules/ μm^2 , respectively (**Figure 3.2a**). Note that on average streptavidin was conjugated to approximately one cRGDfK(C) peptide force sensor when estimated to the nearest integer value using a quantitative fluorescence calibration (see *Methods 3.8.5*).

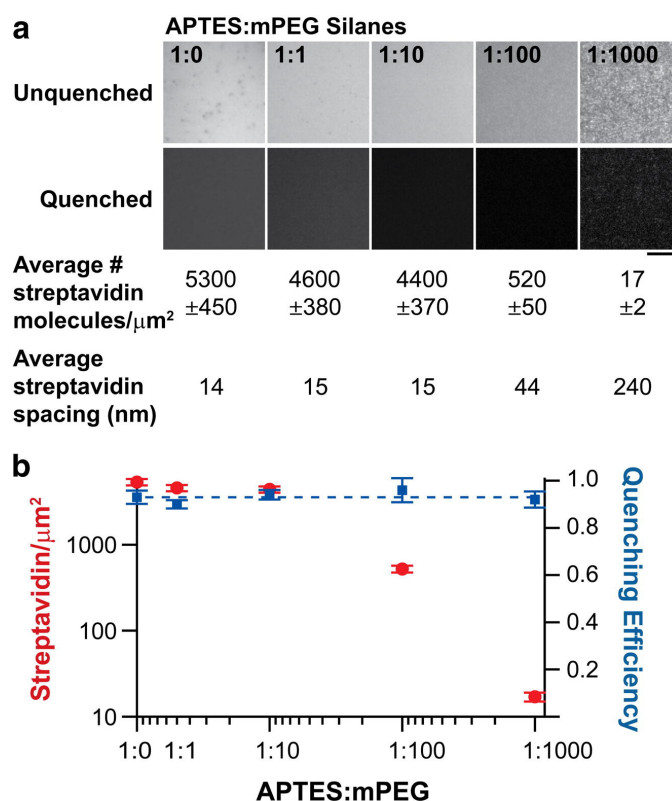


Figure 3.2 (a) Representative fluorescence images of MTFM sensor surfaces generated with a range of densities and the corresponding mean streptavidin intermolecular distance. Scale bar is 10 μm . (b) Plot showing the measured streptavidin surface density and the cRGD-peptide quenching efficiency as a function of the molar ratio of APTES/mPEG silane.

Because the dynamic range and sensitivity of the MTFM probe, and its affinity to the integrin receptor depends on its average equilibrium conformation on the surface, we measured the average fluorophore-quencher distance (polymer extension) using the FRET relation. For these experiments, we synthesized cRGDfK(C)-PEG₂₃ probes that lacked the quencher (donor only), and compared surface fluorescence intensity to that of the tension sensor modified surfaces (donor and acceptor) (**Figure 3.2a**). We found that the average quenching efficiency was 0.93 ± 0.02 (**Figure 3.2b**), thus indicating that the fluorophore-quencher distance ranges from 4.2 to 4.7 nm based on two independent methods that estimate R_0 at 6.4 ± 0.2 nm and 7.2 ± 0.2 nm (Methods and **Figure A3.7** and **Figure A3.8**) and assuming a κ^2 value of $2/3$. This fluorophore-quencher distance is in agreement with the predicted Flory radius of a 23 unit PEG (Flory radius is calculated to be 2.3 nm)¹², in addition to the radius of streptavidin (radius ~ 2 nm, as estimated from the crystal structure (PDB:3ry1)). Based on theoretical models and experimental force spectroscopy measurements of PEG, the dynamic range of this integrin tension sensor is expected to be ~ 1 – 30 pN for FRET efficiency values ranging from 0.9 to 0.1²³⁻²⁵.

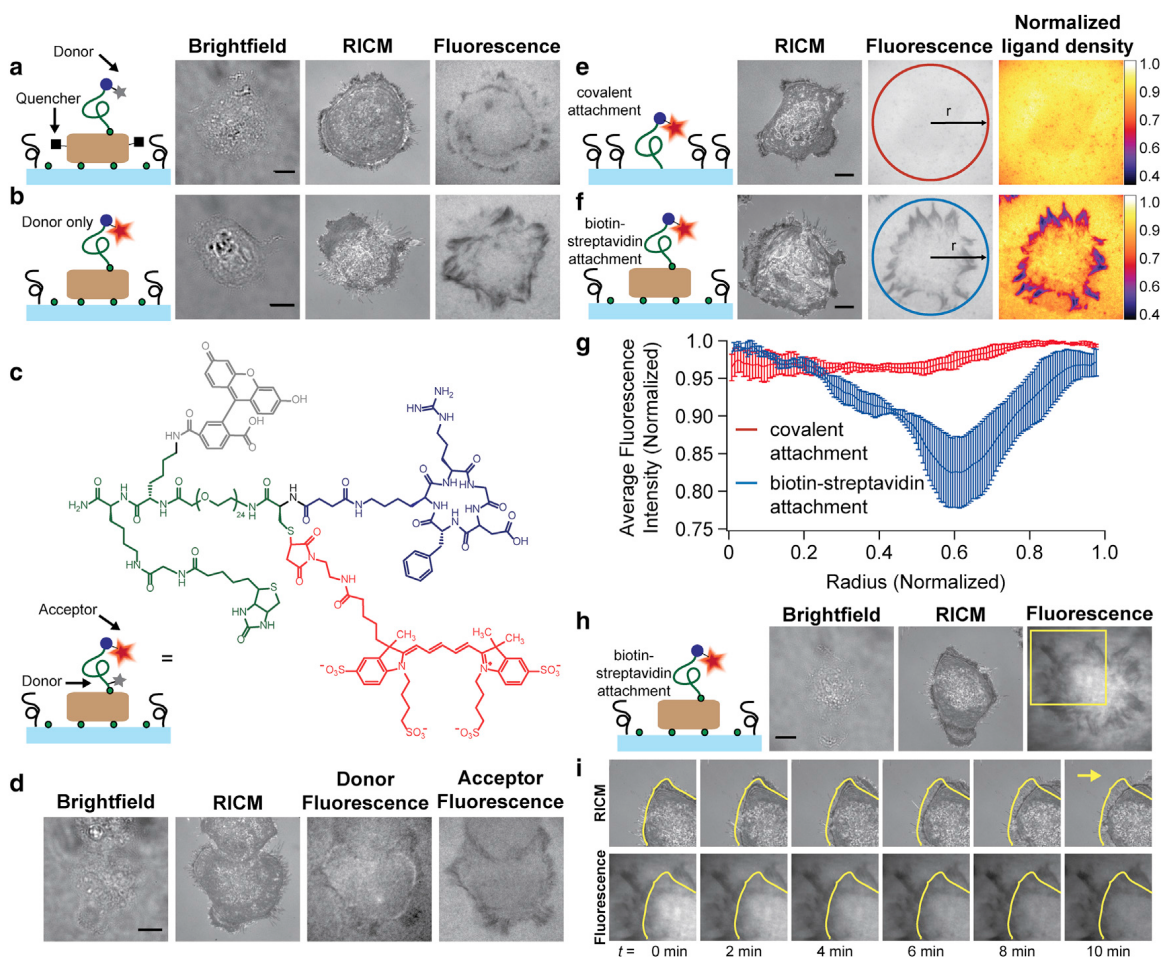


Figure 3.3 Cells incubated on the biotin-immobilized MTFM sensors exhibit negative signal suggesting streptavidin-biotin dissociation. Representative brightfield, RICM, and fluorescence images of a cell incubated on a streptavidin-biotin functionalized surface with a donor-quencher construct (a) and donor only construct (b). A decrease in donor signal is observed under the cell perimeter in both (a) and (b). (c) Schematic and chemical structure of the dual-tagged FRET MTFM sensor. (d) Cells incubated on this dual-tagged FRET surface generally showed a decrease in fluorescence intensity in both the donor and acceptor channels. A slight increase in donor emission at the proximal side of the cell perimeter was observed. (e and f) Representative RICM and fluorescence images of cells incubated on surfaces with ligands that are covalently anchored (e), or immobilized with streptavidin-biotin (f). Pseudocolored images represent the normalized ligand density, and highlight the fraction of ligand lost under each cell within 1 h of cell seeding. (g) Radial distribution functions of fluorescence under cells that were seeded on covalently anchored ligand surfaces (red, such as e), and tethered via streptavidin-biotin linkage (blue, such as f). Error bars represent the standard deviation of signals averaged from three cells. (h) Representative brightfield, RICM, and fluorescence images of HCC1143 cells adhered to cRGDfK(C)-A647-PEG₂₃-biotin peptide anchored to the surface by streptavidin. (i) Time-lapse images of the cell region highlighted in yellow (h). Outline of initial cell position (yellow) reveals the migration of the cell over time (yellow arrow indicates direction of cell motion). Note the negative signal remains constant

despite the translocation of cell edge. All scale bars represent 10 μm .

Moreover, the surface density measurements validate the FRET-determined polymer conformation, and indicate that the average distance (ranging from 14 to 240 nm) between streptavidin molecules is larger than the Flory radius. Taken together, the data indicate that the cRGDfK(C)-QSY21-PEG₂₃-biotin probe adopts the relaxed mushroom conformation on these surfaces, remains highly quenched (> 0.9), and is predicted to support cell binding and focal adhesion formation for APTES:mPEG ratios of 1:0, 1:1, 1:10, and 1:100.

3.4 Integrin forces lead to MTFM sensor dissociation

In initial experiments, we incubated HCC 1143 immortalized breast cancer cells on surfaces that contained quencher-modified streptavidin and the cRGDfK(C)-A647-PEG₂₃-biotin peptide conjugate. Previously, our work has shown that cells do not engage or spread when streptavidin-modified surfaces lack RGD or other cell adhesion ligands^{11, 13}. Cells were incubated on the higher density peptide surfaces (4400 ± 370 streptavidin molecules/ μm^2) for ~ 60 min at 37 °C and 5% CO₂, and then imaged using brightfield, RICM, and fluorescence microscopy. Unexpectedly, we found that the fluorescence signal intensity under the perimeter of most cells was negative (**Figure 3.3a**) and colocalized with vinculin, a focal adhesion marker (**Figure A3.9**). This observation was also confirmed on cRGDfK(C)-A647-PEG₂₃-biotin surfaces that lacked the quencher (**Figure 3b**), suggesting that the dark areas were not related to the presence of the quencher or to polymer conformation. To verify that the PEG ligand was intact, the MTFM sensor was redesigned such that the termini of the polymer were tagged with a dye pair (fluorescein and Alexa 647) that undergoes FRET (**Figure 3.3, c – d**). This was

achieved by generating the sensor using solid-phase peptide synthesis, which was then purified and characterized by RP-HPLC and MALDI-TOF mass spectrometry (**Figure A3.10** and **Figure A3.11**). Cells incubated on these surfaces generally revealed areas of reduced fluorescence in both the donor and the acceptor channels. In contrast to the donor-quencher system (**Figure 3.3a**), some regions of a subset of cells displayed a positive fluorescence signal in the donor channel (**Figure 3.3d**), which typically corresponded to the proximal side of the cell perimeter. The slight increase (~10%) in donor intensity is likely due to extension of the polymer, and this signal may be more readily observed due to the FRET sensitivity when the dyes are directly conjugated to the PEG chain, rather than randomly tagged to streptavidin. In the acceptor channel (**Figure 3.3d**), the decrease in fluorescence signal is similar to that observed in **Figure 3.3a, b**. In all cases, we start observing a net reduction in fluorescence intensity at the edges of this epithelial cell type by the 30 min time point, thus suggesting biotin dissociation. This could occur through dissociation of the streptavidin complex from the surface or dissociation of the biotinylated PEG tension probe from immobilized streptavidin. Further experiments indicated that under these conditions streptavidin remains immobilized, whereas the biotinylated PEG tension probes are dissociated from the surface (*vide infra*).

In some cases, fluorophores display spectral shifts and changes in quantum yield as a result of integrin receptor binding²⁶. To measure this contribution to the fluorescence emission intensity, we generated cRGDfK(C)-A647-PEG₂₄ surfaces that were covalently attached to the substrate. We rationalized that changes to the dye emission intensity on these surfaces would be due to integrin binding. In these experiments, the mean

fluorescence intensity of the surface under each cell showed a ~3% decrease when compared to the background (**Figure 3.3e**). This decrease was uniform across the entire cell contact region. In contrast, streptavidin-biotin anchored ligands showed a decrease of ~30 to 60% at the cell perimeter, which could be clearly visualized when fluorescence images were normalized and displayed as heat maps that represented the fraction of MTFM ligand removed (**Figure 3.3f**). The ligand loss appeared to occur in regions that resembled focal adhesion contacts. The fluorescence intensity of the regions under cells where the ligand was covalently attached or attached via streptavidin-biotin was plotted as a radial distribution function from the cell center (**Figure 3.3g**). The results indicate that the fluorescence intensity under cells incubated on surfaces with ligand anchored by streptavidin-biotin attachment is 10- to 20-fold lower than that observed on surfaces with covalently tethered ligand.

Further evidence of biotin dissociation is revealed by the irreversible nature of the observed negative signal. We collected time-lapse images of a single cell after 90 min of incubation on a streptavidin-biotin surface containing only the donor cRGDfK(C)-A647-PEG₂₃-biotin conjugate (**Figure 3.3h**). As the cell moves toward the right corner of the image and outside the field of view, the negative signal remains unchanged (**Figure 3.3i**). This experiment suggests that loss of donor intensity is irreversible. Controls using pharmacological inhibitors of F-actin and myosin show that biotin dissociation is dependent on the cytoskeleton. We found that cells pretreated with the non-muscle myosin inhibitor blebbistatin for 15 min adhered to the surface, but completely failed to dissociate the streptavidin-anchored MTFM sensor (**Figure A3.12**). Cells treated with latrunculin B (LatB), an F-actin inhibitor, 30 min after adhering to a surface failed to

show any reversibility in signal (**Figure A3.12**). Furthermore, cells treated with soluble cRGD peptide dissociate from the surface but the negative signal remains despite the absence of the cell (**Figure A3.13**). Taken together, these results unambiguously show that the majority of the signal decrease is due to irreversible, cytoskeleton-dependent, and focal-adhesion-dependent biotin dissociation.

Integrin driven biotin dissociation is unexpected given that the streptavidin-biotin interaction is often described as the strongest noncovalent association in nature with an absolute free energy of binding of ~ -18 kcal/mol^{27, 28}. In support of this, experimentally measured rupture forces for streptavidin- biotin were reported at ~ 260 pN using atomic force microscopy²⁸. It should be noted, however, that rupture forces are dependent on the loading rate and temperature. For example, mean streptavidin-biotin rupture forces (at 25 °C) have been recorded at ~ 120 pN and ~ 200 pN at loading rates of 198, and 2300 pN/s, respectively²⁹. Given this remarkable stability, streptavidin-biotin association is commonly used in the field of single molecule biophysics to measure the rupture force and bond lifetime between receptors and their ligands^{30, 31}, including cell surface integrins and ligands derived from the ECM³². It is of interest to note that one report described streptavidin-biotin dissociation at low force regimes (~ 5 pN), but this was shown to occur due to brief (μ s-ms) molecular encounters that do not allow the interaction to reach equilibrium^{33, 34}. In our experiments, the biotin-tagged ligand is incubated with streptavidin for ~ 1 h during MTFM sensor preparation and is therefore at, or near, equilibrium.

The free energy binding of $\alpha_v\beta_3$ integrins with the linear GRGDSP peptide was measured at -3.10 kcal/mol³⁵. Accordingly, single molecule rupture force for integrin-

ligand associations have been reported in the range of ~40 to 90 pN depending on the loading rate, the type of ligand (using RGD peptides and various fibronectin fragments), the type of integrin receptor ($\alpha_v\beta_3$ or $\alpha_5\beta_1$), and the activation state (conformation) of the receptor^{36, 37}. Therefore, literature precedent indicates that integrin-ligand interactions are more likely to dissociate under mechanical load when compared to streptavidin-biotin.

To quantify the likelihood of streptavidin-biotin dissociation over integrin-ligand dissociation when the two bonds are in series, we used published values of k_{off} for both bonds^{19, 20}, and applied the analysis developed by Neuert et al.³⁸ (**Figure A3.14**).

Assuming that both bonds in the series have similar potential widths (Δx), we found that the probability of streptavidin-biotin dissociation under integrin-mediated tension is $\sim 2.8 \times 10^{-5}$. If Δx of streptavidin-biotin is greater than that of the integrin-ligand bond (which is likely), the analysis becomes more complex, as the change in k_{off} becomes loading rate and force dependent. Nonetheless, the k_{off} values differ by orders of magnitude and the streptavidin-biotin bond should survive under integrin-mediated forces.

One of the molecular mechanisms that may contribute to the observed integrin-ligand bond strengthening includes force-induced stabilization of the high-affinity state of integrin receptors^{39, 40}. Kong et al.⁴¹ observed that the $\alpha_5\beta_1$ integrin-ligand bond lifetime can be enhanced by 100-fold upon application of cyclic forces, and termed this phenomenon cyclic mechanical reinforcement. This is likely important given that recent work reported the existence of low frequency (~ 0.1 Hz) traction force oscillations within focal adhesions⁵. Moreover, integrin clustering and focal adhesion maturation leading to the formation of parallel and multivalent ligand-receptor bonds may also contribute to increasing the effective lifetime of the integrin-ligand interaction⁴². These supramolecular

complexes only form at ECM-integrin interfaces that allow for clustering¹⁸. Therefore, single-molecule force spectroscopy experiments performed on the surface of living cells are unable to recapitulate the ligand-receptor stabilization mechanisms that likely occur within focal adhesions. Consequently, the stabilization of integrin-ligand bonds over streptavidin-biotin may not be present in typical single-molecule force-extension experiments. Further evidence supporting our observation of enhanced integrin-ligand affinity comes from a recent report showing that focal adhesion formation requires integrin ligands that can withstand $\sim 50\text{--}60$ pN of tension (as defined by the rupture force under steady-state tension over a duration of < 2 s)⁶. Our own recent MTFM work also shows that integrin receptors can apply 15 pN of tension within some focal adhesions¹³. Therefore, integrin-ligand association must be sufficiently stabilized to withstand these large mechanical loads for extended durations, suggesting a mechanism of integrin-ligand affinity enhancement within functional cell adhesions. Interestingly, these reported magnitudes of tension are likely sufficient to dissociate streptavidin-biotin associations in our experiments. For example, based on the Bell model, loading rates of ~ 0.1 pN/s at 37 °C would lead to a mean streptavidin-biotin rupture force of ~ 57 pN^{29, 43} and the average lifetime of streptavidin-biotin association is on the order of 10^2 s when placed under 40 pN of constant tension^{33, 44}. Therefore, it is feasible that biotin dissociates from streptavidin under the integrin-mediated tension; however, the enhanced stability of the integrin-ligand interaction remains unexpected and is likely related to focal adhesion formation.

3.5 Imaging integrin force dynamics

Given that integrin tension may lead to polymer extension as well as biotin

dissociation, the MTFM sensor was redesigned such that both events result in a positive turn-on fluorescence signal. In this design, the quencher was conjugated to the ligand, whereas the streptavidin was labeled with the Alexa 647 fluorophore (**Figure 3.4a**). Moreover, we expected that upon dissociation this signal would be irreversible, remaining even after dampening of the mechanical load.

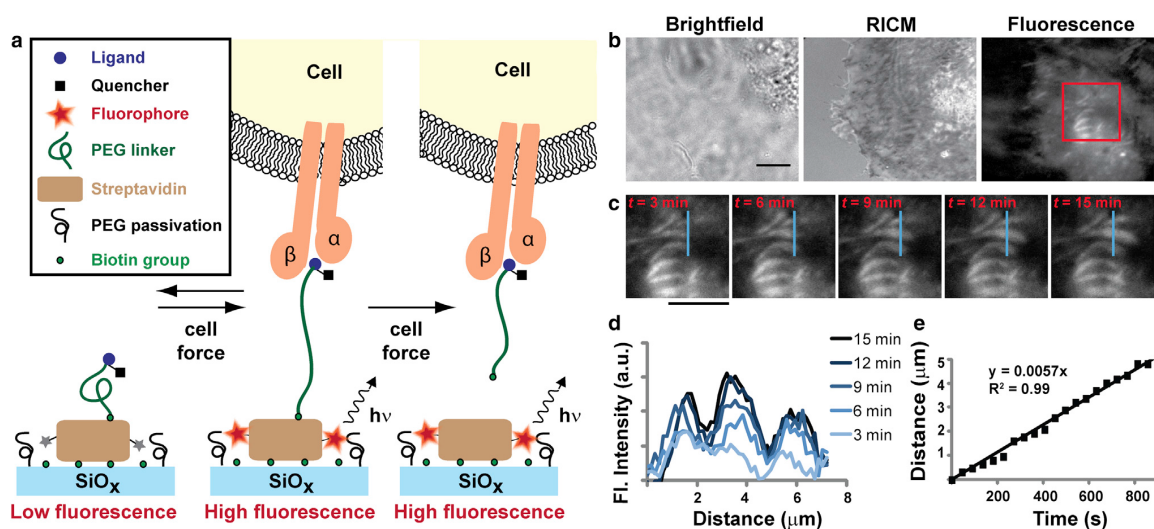


Figure 3.4 Integrin tension imaging in cells incubated on the redesigned MTFM sensor surface. (a) Schematic description showing the response of the redesigned MTFM integrin sensor and its corresponding fluorescence intensity. Integrin tension that is below ~ 30 pN is expected to lead to reversible extension of the MTFM sensor (within 1 h of cell seeding). In contrast, larger forces are expected to lead to irreversible dissociation of biotin from the immobilized streptavidin. Since the fluorophore is conjugated to streptavidin, both force regimes lead to an increase in signal intensity. (b) Representative brightfield, RICM, and integrin MTFM response for a cell that is spreading over the surface (density $\cdot 4600$ streptavidin/mm²). (c) A time-lapse series of images from the noted region of interest (red box) (*t* represents the start of imaging). (d) Line scans represent profiles through the indicated region in (c) as a function of time. (e) Plot showing the translocation of the force region as a function of time. Scale bars represent 10 μ m.

Fluorescence images of cells adhered to surfaces coated with this version of the sensor show subcellular regions with increased fluorescence intensity. This observation indicates that integrin-mediated mechanical tension leads to cRGDfK(C)-QSY21-PEG₂₃ - biotin polymer extension and unbinding from streptavidin (**Figure 3.4b, c**). Some of the

areas appear punctate, whereas others show highly elongated, fiber-like structures that generally run parallel to each other, in agreement with typical chemical staining of focal adhesions⁴⁵. However, due to the irreversibility of the MTFM probe signal, these structures may represent elongated, mature focal adhesions or punctate adhesions that have translocated. Time-lapse total-internal reflection fluorescence microscopy imaging collected over a 15 min time duration revealed the rate of growth of regions of high integrin tension (**Figure 3.4c – e**). The linear rate of integrin tension over this region was ~340 nm/min, which is in agreement, within an order of magnitude, with the reported rate of focal adhesion elongation in NIH 3T3 cells (**Figure 3.4e**)⁴⁶. These images also reveal that biotin unbinding occurs primarily between the sensor and streptavidin rather than at the streptavidin-glass interface. Dissociation of the fluorophore-modified streptavidin from the surface would result in dark regions, which are not observed under these conditions. This is likely due to the high surface density of biotin, which provides multivalent attachment for streptavidin. Low-density biotin surfaces, though, may present streptavidin that is primarily anchored through single biotin attachment, and thus may be prone to surface dissociation. We are unable to verify this, however, due to the low fluorescence signal on surfaces presenting low biotin densities.

3.6 Generality of integrin-driven biotin dissociation and relationship to focal adhesions

To verify that the MTFM signal (and streptavidin-biotin dissociation) is applicable beyond the HCC 1143 cell line and that integrin tension was correlated with focal adhesion formation, HEK 293 cells (**Figure 3.5a**) and NIH 3T3 fibroblasts (**Figure 3.5b**) were incubated on sensor surfaces for 60 min and then fixed and immunostained for vinculin, a common component of focal adhesion complexes. An overlay of the

immunostained images with the MTFM response showed that tension and biotin dissociation is colocalized to focal adhesion formation. It is also important to note that a

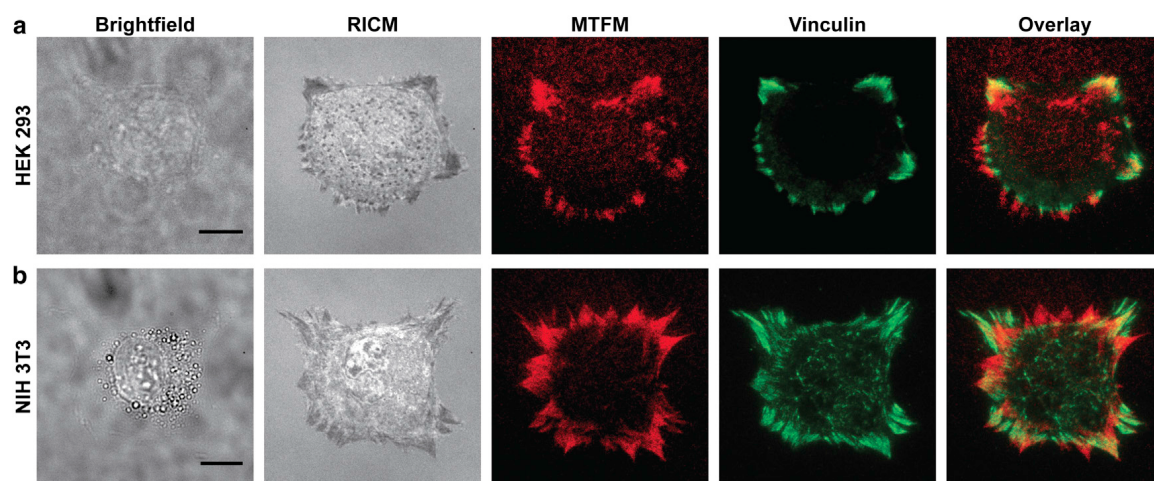


Figure 3.5 Cells immunostained for focal adhesion markers. Representative HEK 293 (a), and NIH 3T3 (b) cells are imaged using brightfield, RICM, MTFM (red), and immunostained for vinculin (green). The final panel shows an overlay of both fluorescence channels (MTFM and vinculin). Scale bar is 10 μm .

portion of the tension signal is not directly colocalized with vinculin, likely due to the irreversibility of the signal. For example, some of the observed MTFM signal represents areas where cells engaged the substrate and dissociated ligand molecules before imaging. Moreover, if allowed to incubate on the MTFM sensor surface for long durations (5 h), large regions of fluorescence increase were observed under nearly all cells on the surface (**Figure A3.15**). Therefore, these data confirm that the MTFM sensor can be used to observe tension applied by a broad range of cell types.

3.7 Conclusion

In conclusion, we found that streptavidin-biotin tethered integrin ligand molecules dissociate from the surface due to cell-driven forces. This finding indicates that single molecule measurements almost certainly underestimate the stability of integrin-ligand interactions within functional focal adhesions. Many mechanoregulatory processes in the

cell involve multiprotein complexes, and thus kinetic and thermodynamic parameters derived from single molecule techniques applied to individual ligand-receptor pairs may not accurately depict the biological context of the crowded cell environment.

Furthermore, we conclude that integrin-ligand tension is likely one to two orders of magnitude larger than had previously been estimated using microscopic averaging methods, such as traction force microscopy⁷. Our force estimate is derived from experiments and calculations that indicate that a steady state tension of ~10-20 pN is needed to reduce the biotin-streptavidin bond lifetime to approximately 10^3 seconds^{33, 44}. Interestingly, Dunn and colleagues recently reported the development of a recombinant protein-based tension probe to investigate integrin forces within focal adhesions¹⁴. These probes employ streptavidin-biotin to tether the force sensor, and the results indicate that integrin-generated forces are approximately 1-5 pN per receptor. While our tension estimates are significantly greater than these reported values, it is plausible that the linear RGD peptide used in the recombinant probes sustains lower forces than the cyclized RGD peptide used in our system. Moreover, spikes in integrin-generated forces may be transient in nature.

Overall, our results are significant because the streptavidin-biotin association is widely used to display small molecules and peptides to screen for cues that trigger cell signaling pathways⁴⁷. Therefore, these results suggest that more robust immobilization strategies are needed to exclude the possibility of cell-based dissociation of surface ligands and remodeling of the surface, which may obscure results.

MTFM is technically facile; however, due to the unexpected dissociation of streptavidin-biotin, the signal presented by the sensor is not easily interpreted as an

average force. Instead, it provides lower bound estimates of integrin-driven tension and this lower bound estimate vastly exceeds what has previously been predicted. We anticipate that the next generation of covalently immobilized MTFM force probes will address existing gaps in our understanding of mechanotransduction pathways during cellular processes such as migration, mitosis, and wound healing.

3.8 Materials and methods

3.8.1 Reagents

Unless otherwise stated, all starting materials and reagents were purchased from Sigma-Aldrich (St. Louis, MO) and used without further purification. All buffers were made with Nanopure water (18.2 MU) and passed through a 0.2 μm filtration system.

3.8.2 Synthesis of cRGDfK(C)-QSY21-PEG₂₃-biotin and cRGDfK(C)-A647-PEG₂₃-biotin

The cyclic Arg-Gly-Asp-D-Phe-Lys(Cys) (cRGDfK(C)) peptide was custom synthesized and reverse-phase HPLC (RP-HPLC) purified by Peptides International (Louisville, KY). Peptide purity was verified by electrospray ionization mass spectrometry and reported to be 98.4% pure (based on HPLC). The QSY21 N-hydroxysuccinimidyl (NHS) ester and Alexa Fluor 647 NHS ester were obtained from Life Technologies (Carlsbad, CA). The biotin-PEG₂₃-maleimide was obtained from Quanta Biodesign (Powell, OH). A 7 mM solution of Alexa 647-NHS ester (or QSY21-NHS ester) and biotin-PEG₂₃-maleimide were typically reacted with a 1.4 mM solution of cRGDfK(C) in DMF (anhydrous grade; EMD Chemicals, Billerica, MA). A 1.5 molar excess of triethylamine (reagent grade, 99%; Fisher Scientific, Pittsburgh, PA) relative to the molar amount of cRGDfK(C) was added to maintain a basic pH, and this reaction was

allowed to proceed overnight at r.t. A RP-HPLC equipped with a binary pump system and a linear diode array detector (Agilent 1100) with monitoring at 220 and 647 or 660 nm was used to purify the final product (**Figure A3.1 and A3.2**). The reaction mixture was injected through a 5 μ m, 4.6 x 250 mm C18 column at a flow rate of 1 ml/min with a linear gradient of 10–60% B over 50 min (A: aqueous 0.05% trifluoroacetic acid (HPLC grade, EMD Chemicals) buffer; B: 0.05% trifluoroacetic acid in acetonitrile (LC-MS Chromasolv, R99.9%; Fluka). This elution gradient was followed by a second gradient of 60–100% B over 10 min to collect the more hydrophobic fractions.

HPLC fractions were collected and analyzed by a matrix-assisted laser desorption/ionization time of flight (MALDI-TOF) mass spectrometer (Voyager-STR) to characterize the final product (**Figure A3.1 and A3.2**). Fractions were mixed with a saturated 2,5-dihydroxybenzoic acid solution (1:1 ethanol:Nanopure water, 0.1% trifluoroacetic acid) at a 1:1 ratio by volume.

3.8.3 Streptavidin labeling

Recombinant streptavidin (Rockland Immunochemicals, Gilbertsville, PA) was labeled with either QSY21 or Alexa 647 by mixing 100 μ g of the protein in phosphate buffered saline (PBS) (10 mM phosphate buffer, 137 mM NaCl, 2.7 mM KCl, pH 7.4) with 10 μ l of 1 M sodium bicarbonate (GR ACS, EMD Chemicals) and a fivefold molar excess of Alexa 647-NHS ester. The reaction was allowed to proceed for 25–30 min at r.t. on a rotating platform. Purification was performed by size-exclusion chromatography using Bio-Gel P4 resin (Bio-Rad, Hercules, CA) swollen with PBS, pH 7.4. The average labeling ratio of the final product was determined by UV-vis absorbance.

3.8.4 Biotin functionalization of glass substrates

The glass substrates were covalently functionalized with biotin following literature precedent^{11, 48}. Briefly, glass coverslips (number 2, 25 mm diameter; VWR, Radnor, PA) were sonicated in Nanopure water for 15 min and etched in piranha (3:1 mixture of sulfuric acid (AR ACS, Macron Chemicals, Center Valley, PA) and 30% hydrogen peroxide) for 15 min. **Warning:** piranha is extremely corrosive and may explode if exposed to organics. The coverslips were thoroughly rinsed with Nanopure water and then placed into three successive wash beakers containing ethyl alcohol (200 proof, Decon Labs, King of Prussia, PA). Next, coverslips were placed into a beaker containing 43 mM silane solution in ethanol. To vary the surface density of terminal amines (**Figure A3.3**), the surfaces were exposed to binary mixtures of silanes, 3-aminopropyltriethoxysilane (APTES), and $\text{CH}_3(\text{CH}_2\text{CH}_2\text{O})_{9-12}(\text{CH}_2)_3\text{Si}(\text{OCH}_3)_3$ (mPEG, Gelest, Morrisville, PA). The molar ratios of the two silanes were 1:1, 1:10, 1:100, and 1:1000. Note that the total silane concentration remained constant at 43 mM. After 1 h immersion in the binary silane solution, slides were submerged in three separate beakers filled with ethanol, rinsed with additional ethanol, and then dried under a stream of ultrahigh purity N_2 . Substrates were then baked in an oven at $\sim 100^\circ\text{C}$ for 15–30 min. After cooling, the slides were incubated with NHS-biotin (Thermo Fisher) at 2 mg/ml in DMSO overnight at r.t. Substrates were then rinsed with ethanol, dried under N_2 , and stored at r.t. until used for sensor preparation.

3.8.5 Surface density quantification

This procedure was adapted from Galush et al.²¹. DOPE-Alexa 647 lipids were used to create a calibration curve (**Figure A3.6**) in which the number of DOPE-Alexa 647 molecules was correlated to the fluorescence intensity of a supported lipid bilayer

(SLB) surface. The SLB was composed of 1,2-dioleoyl-sn-glycero-3-phosphocholine (DOPC) (Avanti Polar Lipids) doped with DOPE-Alexa 647 at concentrations that ranged from 0.016 mol percent to 0.24 mol percent.

DOPE (1,2-di-(9Z-octadecenoyl)-sn-glycero-3-phosphoethanolamine) lipids were purchased from Avanti Polar Lipids. For the DOPE Alexa 647 synthesis, the limiting reagent was the reactive Alexa Fluor 647 NHS ester; therefore the reaction was carried out at a 1:1 ratio of fluorophore to lipid molecule. From a 10 mg/ml DOPE solution in chloroform, 38.9 μ l (MW=743.5 g/mol, 523 nmol) was transferred to a 2 ml glass vial. The organic solvent was evaporated off under a stream of ultrapure N₂ for ~15 min. The dry lipid film was redissolved in 38.9 μ l of dry DMF. A 0.1 M solution of triethylamine in DMF was prepared and 1.5 fold molar excess (7.86 μ l) was added to the lipid solution. The reactive dye (0.5 mg, 523 nmol) was resuspended in 5 μ l of DMF and slowly added to the lipid mixture. A small teflon stirbar was added to the reaction, which was capped, protected from light and allowed to stir overnight at room temperature.

After 16 h, the solution was transferred to a 1.5 ml microcentrifuge tube and spun down to dryness on a Speedvac. The reaction mixture was resuspended in chloroform and transferred to a 20 ml glass vial; both the free dye and the lipid-dye conjugate are soluble in chloroform. The solution was then dried on a rotovap and resuspended in 2 ml of hexane (HPLC grade). The mixture was sonicated briefly (2-3 seconds) until all components were in solution and allowed to sit on the bench undisturbed for 10-15 min as the unreacted dye precipitated out of solution. The soluble fraction containing the lipid-dye conjugate was collected and transferred into a clean 20 ml glass vial, and this process was repeated 3 times. During the fourth repeat, the hexane mixture was placed on

ice for 1.5 h to promote precipitation of any remaining free dye. The solution was then dried down on a rotary evaporator and resuspended in 500 μl of chloroform for further use.

After each transfer, TLC was used to check for the presence of free dye. A solvent mixture of chloroform/methanol/water/concentrated ammonium hydroxide (6/3.4/0.55/0.05) was used for analysis. The final solution showed no visible trace of free dye as seen in the image of the TLC plate (below). The final mass of the product (1584 amu) was observed in MALDI-TOF using negative ion mode with 0.5 M dihydroxybenzoic acid in methanol as the matrix. The yield ranged from 5-10 nmol of DOPE-Alexa 647 (according to $\epsilon_{650} = 239,000 \text{ cm}^{-1} \text{ M}^{-1}$) resulting in a 1-2% overall yield. After synthesis and purification of the final product, the lipids were extruded through a 0.1 μm filter using a Mini-Extruder (Avanti Polar Lipids).

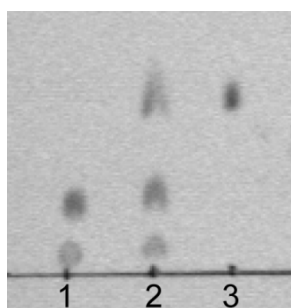


Figure 3.6 Photograph of TLC plate collected after the final stage of purification indicating no free dye present in the final lipid-dye product. Lane 1 = free dye, lane 2 = co-spot (free dye and lipid-dye conjugate), lane 3 = lipid-dye conjugate.

Once a series of SLB surfaces were made using DOPE-Alexa 647 at concentrations varying from 0.016 mol percent to 0.24 mol percent, the calibration curve was created and an F-factor (Eqn. 1) was determined where $I_{\text{soln}(\text{protein conj.})}$ is the fluorescence intensity in bulk solution of the streptavidin- Alexa 647 conjugate and

$I_{soln(lipid\ conj.)}$ is the intensity of an equal concentration of DOPE-Alexa 647 in solution.

Eqn. 3.1

$$F = \frac{I_{soln(protein\ conj.)}}{I_{soln(lipid\ conjugate)}}$$

The F-factor corrects for any change that may occur in the fluorophore intensity as a result of the conjugation and therefore allows the density of streptavidin-Alexa 647 on the surface to be determined using the DOPE-Alexa 647 calibration. A second F-factor was also measured for a cRGDfK(C)-Alexa 647-PEG₂₄-biotin conjugate in order to compare the fluorescence intensity of surfaces with Alexa 647 labeled cRGD to Alexa 647 labeled streptavidin surfaces and thereby determine a binding ratio of the sensor conjugate to surface streptavidin.

The fluorescence intensity of the sample was then calibrated using Eqn. 2,

Eqn. 3.2

$$I_{cal} = \frac{I_{sample}}{F}$$

where I_{sample} is the fluorescence intensity of the biotin functionalized surfaces containing streptavidin-Alexa 647 and F is the F-factor.

The calibrated sample intensity (I_{cal}) was then converted to number of fluorescent molecules on the sample surface by dividing it by the slope of the DOPE- Alexa 647 calibration curve (**Figure A3.6**).

3.8.6 Determination of Förster distance between Alexa 647 and QSY21

To verify the R_0 value between Alexa 647 and QSY21 we designed two calibration experiments (A and B). In the first set of experiments (Calibration A), the quencher was conjugated to streptavidin that was anchored to a supported lipid bilayer. The fluorophore was conjugated to the 5' terminus of a DNA duplex that was then bound

to the streptavidin surface through a biotin group at the second 5' terminus. The distance between Alexa 647 and QSY21 was adjusted by changing the length (number of base pairs) of the DNA duplex (**Figure A3.7**). Note that the base pair composition of the 5' ends of the duplex were maintained (GCC or CAC) throughout each duplex such that the local dye environment remained relatively constant⁴⁹.

The fluorophore-quencher distance was determined using the following equation,

Eqn. 3.3 $\text{Distance (r)} = 0.34(N - 1) + L$

where N represents the number of base pairs in the DNA duplex, and L is the distance added by the fluorophore and biotin attachment linkers at the 5' ends of the DNA strands^{50, 51} as well as the streptavidin radius (as estimated by the crystal structure PDB: 1SWB). The final value of L was estimated to be 3.3 nm with 1.3 nm estimated for the combined linker lengths and 2 nm for the streptavidin radius.

In calibration B, the Förster radius (R_0) of Alexa 647 and QSY21 was determined using DNA hairpin structures of varying lengths (**Figure A3.8**). Each hairpin strand was converted from the closed state (high quenching efficiency) to the open state (decreased quenching efficiency) by adding the complementary strand. The distance between fluorophore and quencher was calculated using Eqn. 3, where L in this case represents the theoretical distance parallel to the DNA helical axis separating Alexa 647 and QSY21 for the case that $n=1$. The final value of L was estimated to be 1.3 nm for the combined fluorophore linker lengths^{50, 51}.

The R_0 values obtained from the two calibrations were then averaged to get a final R_0 value of 6.8 nm. This value is close to the 6.9 nm Förster distance reported by the manufacturer.

3.8.6.1 Calibration A to obtain the Förster distance of Alexa 647

and QSY21

The following DNA oligonucleotides were purchased from Integrated DNA

Technologies (Coralville, IA):

12 mer

5'- /5Biosg/ GCC AGA GCA GTG -3'

5'- /5AmMC6/ CAC TGC TCT GGC -3'

16 mer

5'- /5Biosg/ GCC TAG AGC ATC AGT G -3'

5'- /5AmMC6/ CAC TGA TGC TCT AGG C -3'

21 mer

5'- /5Biosg/ GCC TAT GAA TGA GCT TCA GTG -3'

5'- /5AmMC6/ CAC TGA AGC TCA TTC ATA GGC -3'

33 mer

5'- /5Biosg/ GCC TAT ATA GTC ATC AGC CGT ATA GCA TCA GTG -3'

5'- /5AmMC6/ CAC TGA TGC TAT ACG GCT GAT GAC TAT ATA GGC -3'

Each of the amine functionalized oligonucleotides were labeled with Alexa 647 by adding 2.5 μ l of 10x PBS and 2.5 μ l of 1 M sodium bicarbonate to 20 μ l of 1 mM DNA. An 8-fold molar excess of Alexa 647 NHS ester was then resuspended in 5 μ l of dimethylformamide and added to the DNA mixture. The reaction was placed on a shaker (300 r.p.m.) and allowed to shake overnight at room temperature. The final product was purified by reverse phase HPLC with monitoring at 260 and 647 nm. The reaction mixture was injected through a 5 μ m, 4.6 by 250 mm C₁₈ column at a flow rate of 1 ml/min with a linear gradient of 10 – 60% B over 50 min (A: aqueous 0.1 M triethylammonium acetate buffer; B: acetonitrile (LC-MS Chromasolv, \geq 99.9%; Fluka). This elution gradient was followed by a second gradient of 60 – 100 % B over 10 min to collect the more hydrophobic fractions.

Recombinant streptavidin was labeled with QSY21 by mixing 100 µg of the protein (2 mg/ml) in PBS (10 mM phosphate buffer, 137 mM NaCl, pH 7.4) with 5 µl of 1 M sodium bicarbonate and a 5-fold molar excess of QSY 21 NHS ester (Life Technologies). The reaction was allowed to proceed for 30 min at room temperature on a rotating platform. Purification was performed using a Slide-a-Lyzer Mini dialysis column (Thermo Fisher) with a MW cutoff of 3,500 g/mol. The average labeling ratio of the final product was determined to be 1.7 by UV-visible absorbance measurement.

In order to generate supported lipid bilayers, we prepared a lipid mixture consisting of 99.9% 1,2-dioleoyl-sn-glycero-3-phosphocholine (DOPC, Avanti Polar Lipids) and 0.1% 1,2-dioleoyl-sn-glycero-3-phosphoethanolamine-N-(cap biotinyl) (sodium salt) (DPPEbiotin, Avanti Polar Lipids). After mixing the lipids in the correct proportions in chloroform, the solution was dried with a rotary evaporator and placed under a stream of N₂ to ensure complete evaporation of the solvent. These lipid samples were then resuspended in Nanopure water and subjected to 3 freeze/thaw cycles by alternating immersions in an acetone and dry ice bath and a warm water bath (40 °C). To obtain small unilamellar vesicles (SUV's), lipids were extruded through a high pressure extruder with a 100 nm nanopore membrane (Whatman).

Supported lipid bilayers were assembled by adding SUV's to base etched 96 well plates with glass-bottomed wells. After blocking with BSA (0.1 mg/mL) for 60 min, bilayer surfaces were incubated with either unlabeled streptavidin (1 µg/400 µL) or streptavidin-QSY21 (1 µg/400 µL) for 1 h. Wells were rinsed 3 times with 5 mL of PBS, then incubated with the appropriate DNA-Alexa 647 labeled duplex (200 nM) for 1 h and rinsed 3 times with 5 mL of PBS before imaging.

3.8.6.2 Calibration B to obtain the Förster distance of Alexa 647

and QSY21

Six different DNA hairpin sequences and complementary strands were designed and custom synthesized by Integrated DNA Technologies. The DNA sequence information is listed below:

Oligos	Hairpin Sequence	Complementary Sequence
QSY21 strand (contains biotin for anchoring via biotin-streptavidin and an amine for QSY21-NHS coupling)	5'-/5AmMC6/-CGC ATC TGT GCG GTA TTT CAC TTT - /3BioTEG/-3'	
Alexa 647 strand (contains amine for Alexa 647-NHS coupling)	5'- TTT GCT GGG CTA CGT GGC GCT CTT-/3AmMO/-3	
18mer	5'-GTG AAA TAC CGC ACA GAT GCG <u>TTT- CAT CTT TTG</u> ATG -TTT AAG AGC GCC ACG <u>TAG CCC AGC -3'</u>	5'- AAA CAT CAA AAG ATG AAA -3'
21mer	5'-GTG AAA TAC CGC ACA GAT GCG <u>TTT- CAT ACT TTT</u> TGT ATG -TTT AAG AGC GCC <u>ACG TAG CCC AGC -3'</u>	5'-AAA CAT ACA AAA AGT ATG AAA-3'
24mer	5'-GTG AAA TAC CGC ACA GAT GCG <u>TTT-GCT AGT TTT</u> TTT TCT AGC -TTT AAG AGC <u>GCC ACG TAG CCC AGC -3'</u>	5'-AAA GCT AGA AAA AAA ACT AGC AAA-3'
27mer	5'-GTG AAA TAC CGC ACA GAT GCG <u>TTT-CAG ACT TTT</u> TTT TTT TGT CTG-TTT AAG <u>AGC GCC ACG TAG CCC AGC -3'</u>	5'-AAA CAG ACA AAA AAA AAA AGT CTG AAA- 3'
37mer	5'-GTG AAA TAC CGC ACA GAT GCG <u>TTT-CGA TAC TTT</u> <u>TTT TTT TTT TTT TTT TGT</u> <u>ATC G-TTT AAG AGC GCC</u> <u>ACG TAG CCC AGC -3'</u>	5'-AAA CGA TAC AAA AAA AAA AAA AAA AAA AGT ATC GAA A-3'
45mer	5'-GTG AAA TAC CGC ACA GAT GCG <u>TTT- CGA TAA CTT</u> <u>TTT TTT TTT TTT TTT TTT</u> <u>TTG TTA TCG -TTT AAG AGC</u> <u>GCC ACG TAG CCC AGC -3'</u>	5'- AAA CGA TAA CAA AAA AAA AAA AAA AAA AAA AAA AAG TTA TCG AAA-3'

*Three thymine bases were added as a linker at the end of hairpin stem to increase the flexibility. The complementary strand hybridizes to both the 3-T linkers as well as the hairpin sequence.

The anchor arm was labeled with QSY21 and the upper arm was labeled with Alexa 647 (**Figure A3.8**) by adding 1 µl of 1 mM DNA and 1 µl of 1 M sodium bicarbonate to 7 µl of PBS. Then, 1 µl of 10 mM Alexa 647-NHS ester (10-fold molar excess) was added to the DNA mixture. The reaction was allowed to incubate at room

temperature overnight.

All the hairpins were anchored on the lipid membrane surface through a biotin-streptavidin interaction in 96-well plates with glass-bottomed wells. Supported lipid bilayers were assembled by adding small unilamellar vesicles (see above for synthesis) to base-etched 96-well plates. After blocking with BSA (0.1 mg/ml) for 30 min, bilayer surfaces were incubated with streptavidin (0.4 μ g per well) for 1 h. Wells were then rinsed 3 times with 5 ml of PBS and incubated with the hairpin structure for 1 h. Finally, wells were rinsed 3 times with 5 ml PBS and imaged.

Quenching of the closed hairpin: In order to verify that the quenching of the fluorophore occurred when the hairpin was in the closed conformation, a solution fluorescence experiment was performed using the 37mer hairpin structure. The hairpin was formed and folded in 50 μ l PBS at a concentration of 50 nM and the complementary strand was in 10-fold molar excess (500nM) to open the hairpin.

Denaturation step: 75 °C, 5 min

Renaturation step: temperature was allowed to return to room temperature at a rate of 4 °C every 3 min.

When the hairpin hybridized with the complementary strand, we observed an increase in fluorescence signal (data not shown).

Förster distance of Alexa 647 and QSY21 calibration curve. The six hairpins were formed and folded in 50 μ l PBS at 100 nM and the complementary strand was added in 10-fold molar excess (1000 nM) to open the hairpin.

Denaturation step: 75 °C, 5 min

Renaturation step: temperature was allowed to return to room temperature at a rate of 4

°C every 3 min.

In this experiment, the longest hairpin (45mer, 15.38 nm) was used to determine the donor only intensity (the 0% energy transfer efficiency) in the calibration experiment.

3.8.7 cRGDfK(C)-peptide conjugate immobilization with streptavidin-biotin

The biotin functionalized slides (described previously) were placed into cell chambers (attofluor chambers, Life Technologies), rinsed with 50 ml of Nanopure water, and then 50 ml of PBS, pH 7.4. To minimize nonspecific protein adsorption, surfaces were incubated with 100 µg/ml bovine serum albumin (BSA) (OmniPur BSA, Fraction V; EMD Chemicals) at room temperature for 1 h. The chamber was rinsed with 50 ml PBS, pH 7.4 and streptavidin conjugated with either QSY21 or Alexa 647 was added to a final concentration of 47 nM. After 1 h incubation, the chamber was rinsed with 50 ml PBS, pH 7.4, and the cRGDfK(C)-peptide conjugate was added at a concentration of 100 nM to the chamber and incubated for 1 h. The chamber was finally rinsed with 50 ml of PBS before imaging and plating cells.

3.8.8 Synthesis of cRGDfK α -thioester, 1

Synthesis of 1 was based upon the solid-phase synthesis of cyclic RGD derivatives reported by Xiao et al.⁵². The resulting peptide thioester 1 was then purified by RP-HPLC and characterized by MALDI-TOF MS (data not shown).

3.8.9 Synthesis of fluorescein-PEG₂₄-biotin conjugate, 2

This precursor was generated using solid-phase peptide synthesis and on-resin dye labeling. The sensor was cleaved from the resin with 95% trifluoroacetic acid with triisopropylsilane as a scavenger. Compound 2 was characterized by RP-HPLC and

MALDI-TOF MS (data not shown).

3.8.10 Conjugation of 1 and 2 to generate cRGDfK-Alexa 647-PEG24-fluorescein-biotin, 4

Native chemical ligation was used to conjugate 1 and 2 by mixing 5 mM of 1 and 10 mM of 2 in 20 mM sodium phosphate buffer (pH 7.5) containing 5 mM betaine and 30 mM sodium 2-mercaptoethanesulfonic acid (MPAA) (**Figure A3.10**). The reaction mixture was incubated for 24 h at room temperature to form compound 3. Finally, the Alexa 647-maleimide was coupled to the cysteine thiol group in 3 through Michael addition. The reaction mixture was incubated in DMF with N,N-diisopropylethylamine for 6 h. The product 4 was then purified by RP-HPLC and analyzed by MALDI-TOF MS (**Figure A3.11**).

3.8.11 Covalent conjugation of cRGDfK(C)-A647-PEG₂₄ to substrate

This procedure was adapted from Ha et al.⁵³ and Roy et al.⁵⁴. Briefly, glass coverslips were functionalized with 100% APTES (as described previously). They were then incubated in a PBS solution containing 5% w/v of methoxy capped PEG-NHS ester (MW: 2000, Nanocs, New York, NY), 0.2% w/v NHS-PEG₂₄-maleimide (Quanta Biodesign), and 0.1 M NaHCO₃ to adjust the pH. After 3 h, slides were thoroughly rinsed with Nanopure water followed by neat ethanol and dried under N₂. A 20 μM solution of the cRGDfK(C)-A647 peptide in PBS (pH 7.4) was then incubated on the surface and allowed to react with the maleimide-presenting PEG polymer for 3 h. Slides were rinsed with Nanopure water and used with live cells within 24 h of functionalization.

3.8.12 Cell culture

HCC 1143 cells were cultured in RPMI 1640 medium (Mediatech, Manassas,

VA) supplemented with 10% fetal bovine serum (FBS) (Mediatech), HEPES (10 mM, Sigma), sodium pyruvate (1 mM, Sigma), L-glutamine (2.5 mM, Mediatech), penicillin G (100 IU/ml, Mediatech), and streptomycin (100 mg/ml, Mediatech). NIH 3T3 fibroblasts were cultured in Dulbecco's modified Eagle's medium (Mediatech) supplemented with 10% Cosmic Calf serum (Mediatech), L-glutamine (2.5 mM, Mediatech), penicillin G (100 IU/ml, Mediatech), and streptomycin (100 mg/ml, Mediatech). HEK 293 cells were cultured in EMEM (Mediatech) supplemented with 10% FBS (Mediatech), nonessential amino acids (1%), penicillin G (100 IU/ml, Mediatech), and streptomycin (100 mg/ml, Mediatech). All cells were incubated at 37 °C with 5% CO₂ and passaged at 70–80% confluency.

3.8.13 Live cell fluorescence microscopy imaging

The plated cells were maintained at 37 °C during imaging by using a warming apparatus consisting of a sample warmer and an objective warmer (Warner Instruments 641674D and 640375). An Eclipse Ti microscope driven by the Elements software package (Nikon) was used for all imaging experiments. The microscope features an Evolve electron multiplying charge-coupled device (EMCCD; Photometrics), an Intensilight epifluorescence source (Nikon), a CFI Apo 100 (numerical aperture (NA) . 1.49) objective (Nikon), and a total-internal reflection fluorescence (TIRF) launcher with two laser lines (Coherent): 488 nm (10 mW) and 640 nm (20 mW). This microscope also includes the Nikon Perfect Focus System, an interferometry-based focus lock that allowed the capture of multipoint and time-lapse images without loss of focus. The microscope was equipped with the following Chroma filter sets: TIRF 488, TIRF 640, Cy5, TRITC, and reflection interference contrast microscopy (RICM).

3.8.14 Immunostaining protocols

Cells were fixed with 4% paraformaldehyde for 12 min, treated with 0.1% Triton X for 5 min, and rinsed with 1% BSA in PBS, pH 7.4. Cells were left in BSA blocking for 4 h or overnight at 4 °C and then immunostained with FITC-conjugated mouse anti-vinculin monoclonal antibody (clone hVIN-1, Sigma) according to manufacturer's protocol. A final rinse of 5 mL of 1% BSA in PBS, pH 7.4 was performed three times before imaging.

3.9 References

1. Hynes, R.O. Integrins: bidirectional, allosteric signaling machines. *Cell* **2002**, *110*, 673-687.
2. Puklin-Faucher, E. & Sheetz, M.P. The mechanical integrin cycle. *J. Cell Sci.* **2009**, *122*, 179-186.
3. Riveline, D. et al. Focal contacts as mechanosensors: externally applied local mechanical force induces growth of focal contacts by an mDia1-dependent and ROCK-independent mechanism. *J. Cell Biol.* **2001**, *153*, 1175-1186.
4. Grashoff, C. et al. Measuring mechanical tension across vinculin reveals regulation of focal adhesion dynamics. *Nature* **2010**, *466*, 263-266.
5. Plotnikov, S.V., Pasapera, A.M., Sabass, B. & Waterman, C.M. Force fluctuations within focal adhesions mediate ECM-rigidity sensing to guide directed cell migration. *Cell* **2012**, *151*, 1513-1527.
6. Wang, X. & Ha, T. Defining single molecular forces required to activate integrin and Notch signaling. *Science* **2013**, *340*, 991-994.

7. Sabass, B., Gardel, M.L., Waterman, C.M. & Schwarz, U.S. High resolution traction force microscopy based on experimental and computational advances. *Biophys. J.* **2008**, *94*, 201-220.
8. Schwarz, U.S. et al. Calculation of forces at focal adhesions from elastic substrate data: The effect of localized force and the need for regularization. *Biophys. J.* **2002**, *83*, 1380-1394.
9. Tan, J.L. et al. Cells lying on a bed of microneedles: An approach to isolate mechanical force. *Proc. Natl. Acad. Sci. U.S.A.* **2003**, *100*, 1484-1489.
10. Dufrene, Y.F. et al. Five challenges to bringing single-molecule force spectroscopy into living cells. *Nat. Methods* **2011**, *8*, 123–127.
11. Stabley, D.R., Jurchenko, C., Marshall, S.S. & Salaita, K.S. Visualizing mechanical tension across membrane receptors with a fluorescent sensor. *Nat. Methods* **2012**, *9*, 64-67.
12. de Gennes, P.G. Conformations of Polymers Attached to an Interface. *Macromolecules* **1980**, *13*, 1069-1075.
13. Liu, Y., Yehl, K., Narui, Y. & Salaita, K. Tension sensing nanoparticles for mechano-imaging at the living/nonliving interface. *J. Am. Chem. Soc.* **2013**, *135*, 5320-5323.
14. Morimatsu, M., Mekhdjian, A.H., Adhikari, A.S. & Dunn, A.R. Molecular tension sensors report forces generated by single integrin molecules in living cells. *Nano Lett.* **2013**, *13*, 3985-3989.
15. Green, N.M. Avidin and Streptavidin. *Methods Enzymol.* **1990**, *184*, 51-67.

16. Englund, E.A. et al. Programmable multivalent display of receptor ligands using peptide nucleic acid nanoscaffolds. *Nat. Commun.* **2012**, *3*, 614.
17. Schottelius, M., Laufer, B., Kessler, H. & Wester, H.-J. Ligands for mapping $\alpha\beta3$ -integrin expression in vivo. *Acc. Chem. Res.* **2009**, *42*, 969-980.
18. Huang, J. et al. Impact of order and disorder in RGD nanopatterns on cell adhesion. *Nano Letters* **2009**, *9*, 1111-1116.
19. Deng, L., Kitova, E.N. & Klassen, J.S. Dissociation kinetics of the streptavidin-biotin interaction measured using direct electrospray ionization mass spectrometry analysis. *J. Am. Mass Spectrom.* **2013**, *24*, 49-56.
20. Klumb, L.A.C., V.; Stayton, P.S. Energetic roles of hydrogen bonds at the ureido oxygen binding pocket in the streptavidin-biotin complex. *Biochemistry* **1998**, *37*, 7657-7663.
21. Galush, W.J., Nye, J.A. & Groves, J.T. Quantitative fluorescence microscopy using supported lipid bilayer standards. *Biophys. J.* **2008**, *95*, 2512-2519.
22. Narui, Y. & Salaita, K. Dip-pen nanolithography of optically transparent cationic polymers to manipulate spatial organization of proteolipid membranes. *Chem. Sci.* **2012**, *3*, 794-799.
23. Marko, J.F. & Siggia, E.D. Bending and twisting elasticity of DNA. *Macromolecules* **1994**, *27*, 981-988.
24. Bouchiat, C. et al. Estimating the persistence length of a worm-like chain molecule from force-extension measurements. *Biophys. J.* **1999**, *76*, 409-413.

25. Kienberger, F. et al. Static and dynamical properties of single poly(ethylene glycol) molecules investigated by force spectroscopy. *Single Molecules* **2000**, *1*, 123-128.
26. Shi, H., Liu, J., Geng, J., Tang, B.Z. & Liu, B. Specific detection of integrin $\alpha v\beta 3$ by light-up bioprobe with aggregation-induced emission characteristics. *J. Am. Chem. Soc.* **2012**, *134*, 9569-9572.
27. General, I.J., Dragomirova, R. & Meirovitch, H. Absolute free energy binding of avidin/biotin, revisited. *J. Phys. Chem. B* **2012**, *116*, 6628-6636.
28. Moy, V.T., Florin, E.L. & Gaub, H.E. Intermolecular forces and energies between ligands and receptors. *Science* **1994**, *266*, 257-259.
29. Yuan, C., Chen, A., Kolb, P. & Moy, V.T. Energy landscape of streptavidin-biotin complexes measured by atomic force microscopy. *Biochemistry* **2000**, *39*, 10219-10223.
30. Smith, S.B., Finzi, L. & Bustamante, C. Direct mechanical measurements of the elasticity of single DNA molecules by using magnetic beads. *Science* **1992**, *258*, 1122-1126.
31. Hohng, S. et al. Fluorescence-force spectroscopy maps two-dimensional reaction landscape of the Holliday junction. *Science* **2007**, *318*, 279-283.
32. Yu, C., Law, J.B.K., Suryana, M., Low, H.Y. & Sheetz, M.P. Early integrin binding to Arg-Gly-Asp peptide activates actin polymerization and contractile movement that stimulates outward translocation. *Proc. Natl. Acad. Sci. U.S.A.* **2011**, *108*, 20585.

33. Pincet, F. & Husson, J. The solution to the streptavidin-biotin paradox: The influence of history on the strength of single molecular bonds. *Biophys. J.* **2005**, *89*, 4374-4381.
34. Merkel, R., Nassoy, P., Leung, A., Ritchie, K. & Evans, E. Energy landscapes of receptor-ligand bonds explored with dynamic force spectroscopy. *Nature* **1999**, *397*, 50-53.
35. Choi, Y., Kim, E., Lee, Y., Han, M.H. & Kang, I.-C. Site-specific inhibition of integrin $\alpha\text{v}\beta\text{3}$ -vitronectin association by a ser-asp-val sequence through an arg-gly-asp-binding site of the integrin. *Proteomics* **2010**, *10*, 72-80.
36. Lehenkari, P.P. & Horton, M.A. Single integrin molecule adhesion forces in intact cells measured by atomic force spectroscopy. *Biochem. Biophys. Res. Comm.* **1999**, *259*, 645-650.
37. Li, F., Redick, S.D., Erickson, H.P. & Moy, V.T. Force measurements of the $\alpha\text{5}\beta\text{1}$ integrin-fibronectin interaction. *Biophys. J.* **2003**, *84*, 1252-1262.
38. Neuert, G., Albrecht, C.H. & Gaub, H.E. Predicting the rupture probabilities of molecular bonds in series. *Biophys. J.* **2007**, *93*, 1215-1223.
39. Friedland, J.C., Lee, M.H. & Boettiger, D. Mechanically activated integrin switch controls $\alpha\text{5}\beta\text{1}$ function. *Science* **2009**, *323*, 642-644.
40. Kong, F., Garcia, A.J., Mould, A.P., Humphries, M.J. & Zhu, C. Demonstration of catch bonds between an integrin and its ligand. *J. Cell Biol.* **2009**, *185*, 1275-1284.
41. Kong, F. et al. Cyclic mechanical reinforcement of integrin-ligand interactions. *Mol. Cell* **2013**, *49*, 1060-1068.

42. Schoen, I., Pruitt, B. & Vogel, V. The yin-yang of rigidity sensing: how forces and mechanical properties regulate the cellular response to materials. *Annu. Rev. Mater. Res.* **2013**, *43*, 6.1-6.30.
43. Bell, G.I. Models for the specific adhesion of cells to cells. *Science* **1978**, *200*, 618-627.
44. Tabard-Cossa, V. et al. Single-molecule bonds characterized by solid-state nanopore force spectroscopy. *ACS Nano* **2009**, *3*, 3009-3014.
45. Singer, I.I. Association of fibronectin and vinculin with focal contacts and stress fibers in stationary hamster fibroblasts. *J. Cell Biol.* **1982**, *92*, 398-408.
46. Stricker, J., Aratyn-Schaus, Y., Oakes, P.W. & Gardel, M.L. Spatiotemporal constraints on the force-dependent growth of focal adhesions. *Biophys. J.* **2011**, *100*, 2883-2893.
47. Klim, J.R. et al. Small-molecule-modified surfaces engage cells through the $\alpha\beta3$ integrin. *ACS Chem. Biol.* **2012**, *7*, 518-525.
48. Clack, N.G., Salaita, K. & Groves, J.T. Electrostatic readout of DNA microarrays with charged microspheres. *Nat. Biotech.* **2008**, *26*, 825-830.
49. Yun, C.S. et al. Nanometal surface energy transfer in optical rulers, breaking the FRET barrier. *J. Am. Chem. Soc.* **2005**, *127*, 3115-3119.
50. Clegg, R.M., Murchie, A.I.H., Zechel, A. & Lilley, D.M.J. Observing the helical geometry of double-stranded DNA in solution by fluorescence resonance energy transfer. *Proc. Natl. Acad. Sci. U.S.A.* **1993**, *90*, 2994-2998.

51. Norman, D.G., Grainger, R.J., Uhrin, D. & Lilley, D.M.J. Location of cyanine-3 on double-stranded DNA: Importance for fluorescence resonance energy transfer studies. *Biochemistry* **2000**, *39*, 6317-6324.
52. Xiao, J., Chen, R., Pawlicki, M.A. & Tolbert, T.J. Targeting a homogenously glycosylated antibody Fc to bind cancer cells using a synthetic receptor ligand. *J. Am. Chem. Soc.* **2009**, *131*, 13616-13618.
53. Ha, T. et al. Initiation and re-initiation of DNA unwinding by the *Escherichia coli* Rep helicase. *Nature* **2002**, *419*, 638-641.
54. Roy, R., Hohng, S. & Ha, T. A practical guide to single-molecule FRET. *Nat. Methods* **2008**, *5*, 507-516.
55. Jamali, Y., Jamali, T. & Mofrad, R.R.K. An agent based model of integrin clustering: Exploring the role of ligand clustering, integrin homo-oligomerization, integrin-ligand affinity, membrane crowdedness and ligand mobility. *J. Comp. Phys.* **2013**, *244*, 264-278.
56. Goldmann, W.H. Kinetic determination of focal adhesion protein formation. *Biochem. Biophys. Res. Comm.* **2000**, *271*, 553-557.

Appendix 3

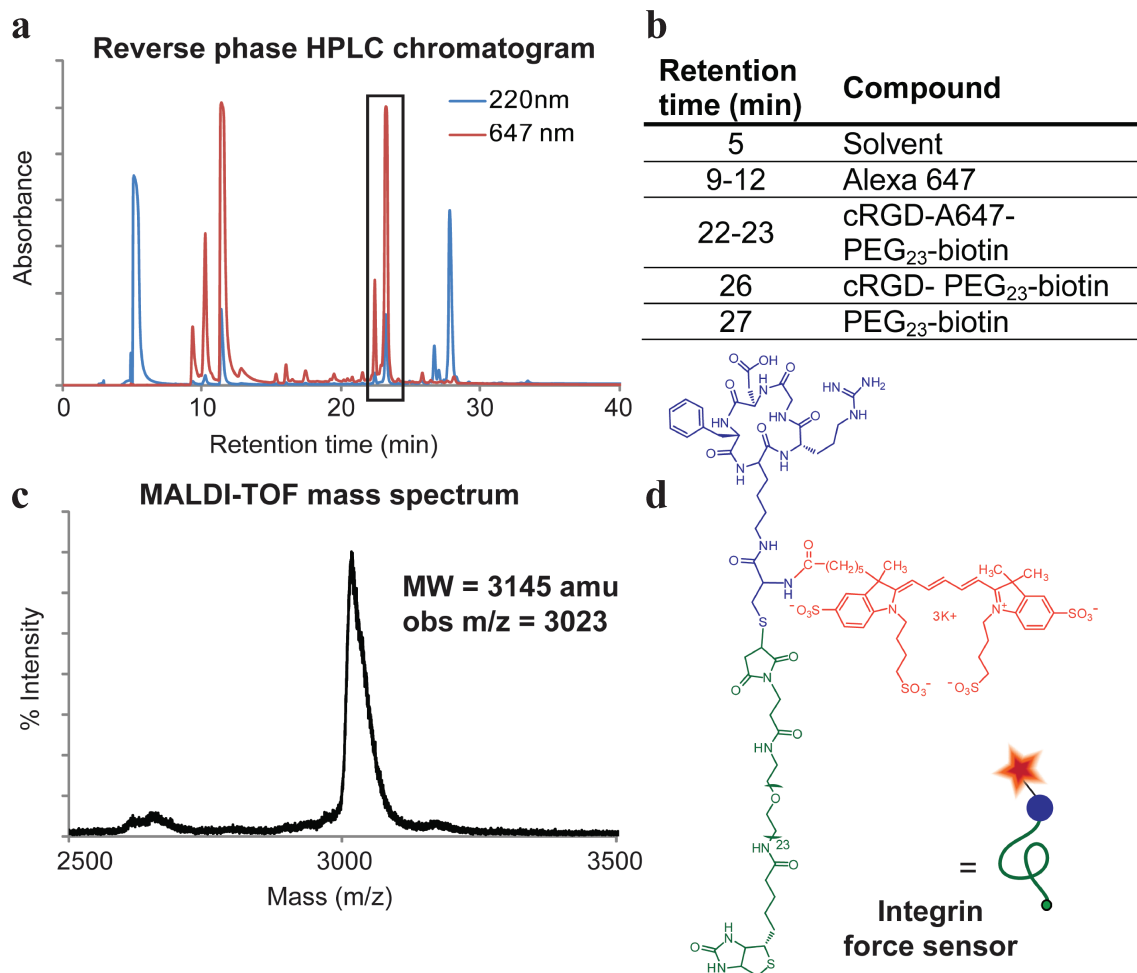


Figure A3.1 Purification and characterization of the cRGDfK(C)-A647-PEG₂₃-biotin conjugate. (a, b) Reverse phase HPLC chromatogram of the Alexa 647 NHS, cRGDfK(C), and biotin-PEG₂₃-maleimide reaction mixture. The absorbance was measured at 220 and 647 nm. 1 ml fractions were collected as they eluted off the column (flow rate = 1 ml/min). The peaks were characterized by MALDI-TOF MS (c) and the final integrin force sensor product ($MW_{\text{obs}} = 3023$; $MW_{\text{expected}} = 3145$) was found to elute at 22-23 min. (d) Structure of the final product.

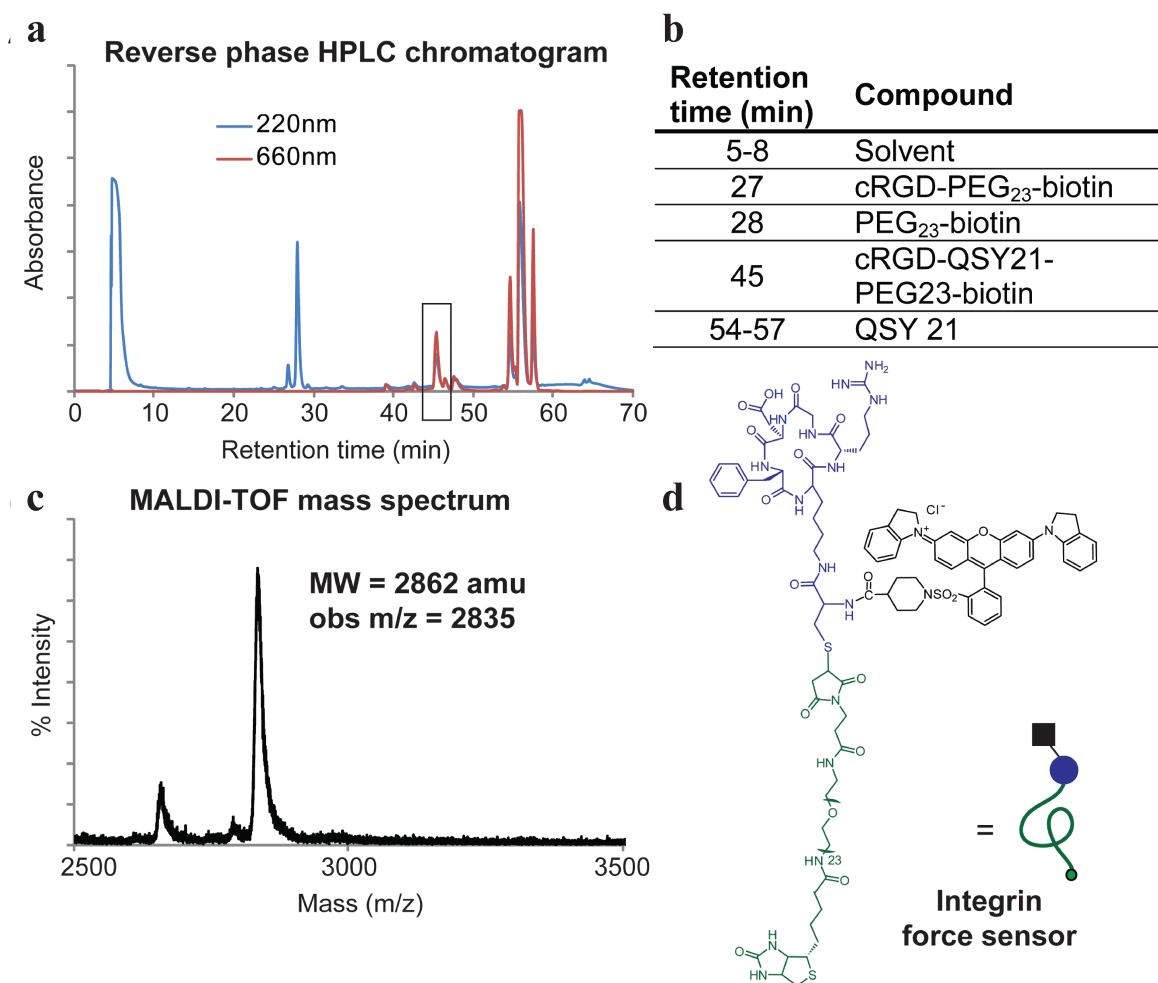


Figure A3.2 Purification and characterization of the cRGDfK(C)-QSY21-PEG₂₃-biotin conjugate. (a, b) Reverse phase HPLC chromatogram of the QSY21 NHS, cRGDfK(C), and biotin-PEG₂₃-maleimide reaction mixture. The absorbance was measured at 220 and 660 nm. 1 ml fractions were collected as they eluted off the column (flow rate = 1 ml/min). The peaks were characterized by MALDI-TOF MS (c) and the final integrin force sensor product ($MW_{\text{obs}} = 2835$; $MW_{\text{expected}} = 2862$) was found to elute at 45 min. (d) Structure of the final product.

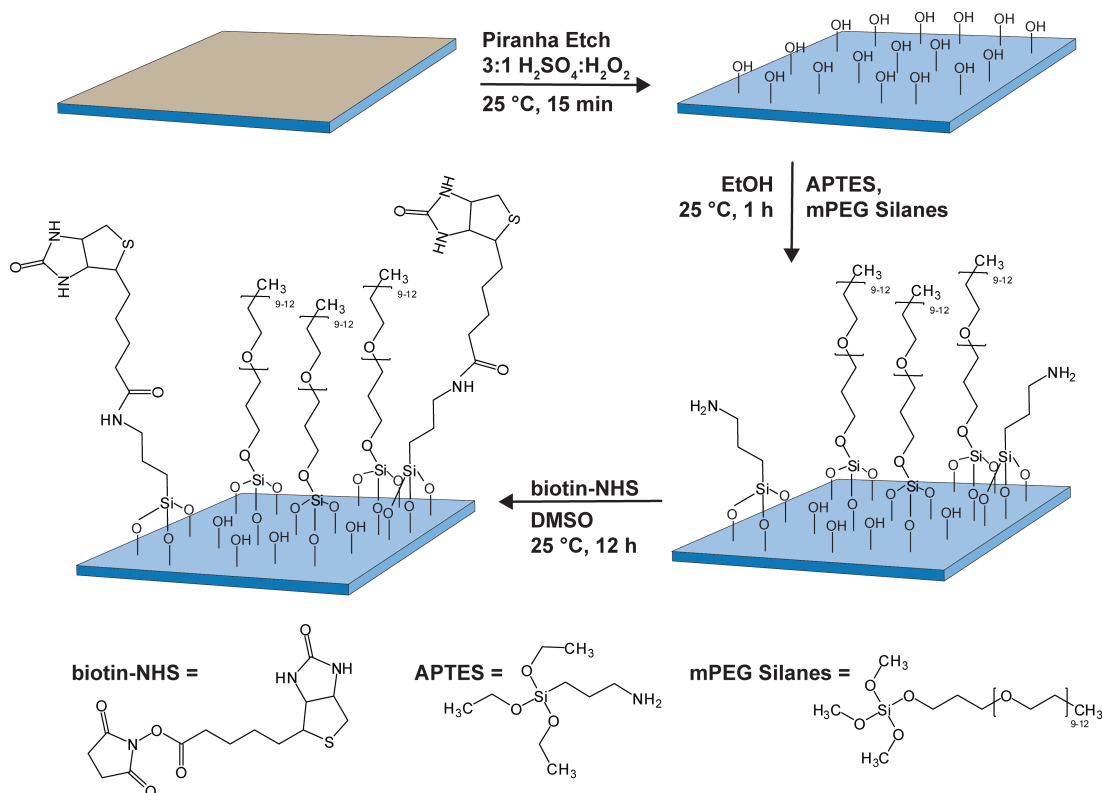


Figure A3.3 Scheme depicting the covalent biotin-functionalization of glass surfaces. Glass coverslips (as described in Materials and Methods) were piranha-etched in order to produce a clean glass surface containing free terminal hydroxyl groups. A binary mixture of APTES and mPEG silane at different ratios was coupled to the hydroxyl surface groups of the glass coverslip to generate varying ratios of reactive amine and passivating mPEG groups. In the final reaction step, biotin containing a reactive N-hydroxysuccinimide ester was coupled to the free amines on the surface.

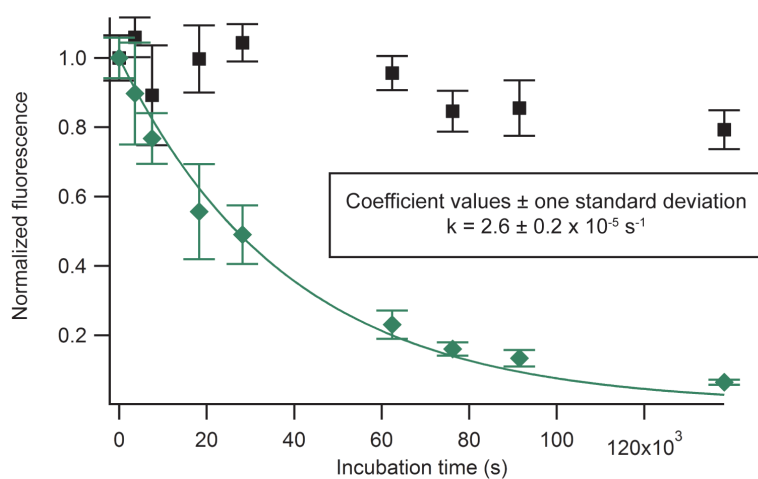


Figure A3.4 Determination of streptavidin-biotin dissociation rate. To determine the rate of biotin dissociation in our experiments, streptavidin modified surfaces (green

diamonds) were functionalized with Alexa 488-PEG₂₃-biotin conjugates and then incubated with free biotin (50 nM) and imaged over a period of 33 hrs at 37 °C. Surfaces covalently functionalized with Alexa 488 (black squares) were also prepared and imaged as a control. Plot shows the fluorescence intensity of surfaces as a function of time. Error bars represent the standard deviation of fluorescence intensity from either over 40 regions across two substrates (covalent surfaces, black squares) or over 60 regions across three substrates (streptavidin-biotin surfaces, green diamonds). We used a surface preparation that was identical to the protocols described in the methods section of the manuscript. The fluorescence decay was fit to the mono-exponential function $f(t) = \exp(-kt)$ using IGOR, and yielded values of $k_{\text{off}} = 2.6 \pm 0.2 \times 10^{-5} \text{ s}^{-1}$, where the error in the k_{off} value represents the error in the fit. These values are both in agreement with rate constants reported by Deng, et al.¹⁹ ($k_{\text{off}} = 5.0 \pm 0.2 \text{ s}^{-1} \times 10^{-5}$) and Klumb, et al.²⁰ ($k_{\text{off}} = 4.1 \pm 0.3 \times 10^{-5} \text{ s}^{-1}$) at 37 °C.

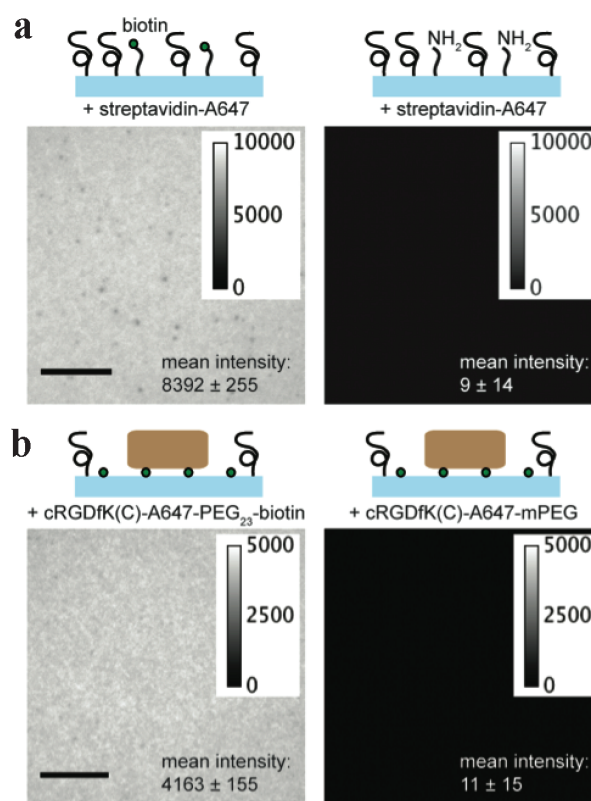


Figure A3.5 Force sensor conjugates are immobilized through biotin-specific interactions. a) Glass coverslips were functionalized with 1:10 amine:mPEG silanes (as described in the manuscript). The positive control surface was treated with NHS-biotin to covalently immobilize biotin, while the negative control substrate was not coupled to biotin. Both types of substrates were then incubated with streptavidin-Alexa 647 and imaged to quantify non-specific binding. This experiment showed that 99.9% of streptavidin binding occurs through specific streptavidin-biotin interaction. Mean intensities are background subtracted. b) To determine cRGDfK(C)-A647-PEG₂₃-biotin non-specific binding, surfaces were covalently modified with biotin and then incubated with unlabeled streptavidin (as described in the manuscript). Surfaces were incubated

with cRGDfK(C)-A647-PEG₂₃ force reporter constructs that either included or lacked the biotin group and then were washed and imaged to determine non-specific binding of the tension reporter. This was found to be less than 0.3%. Mean intensities are background subtracted. Scale bars represent 10 μm .

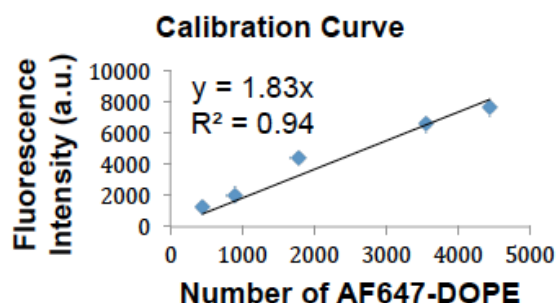


Figure A3.6 Quantitative fluorescence calibration to measure surface density of streptavidin and peptide mechanophore. Calibration showing the fluorescence intensity of DOPE-Alexa 647 doped DOPC supported lipid membrane (see Methods and Materials).

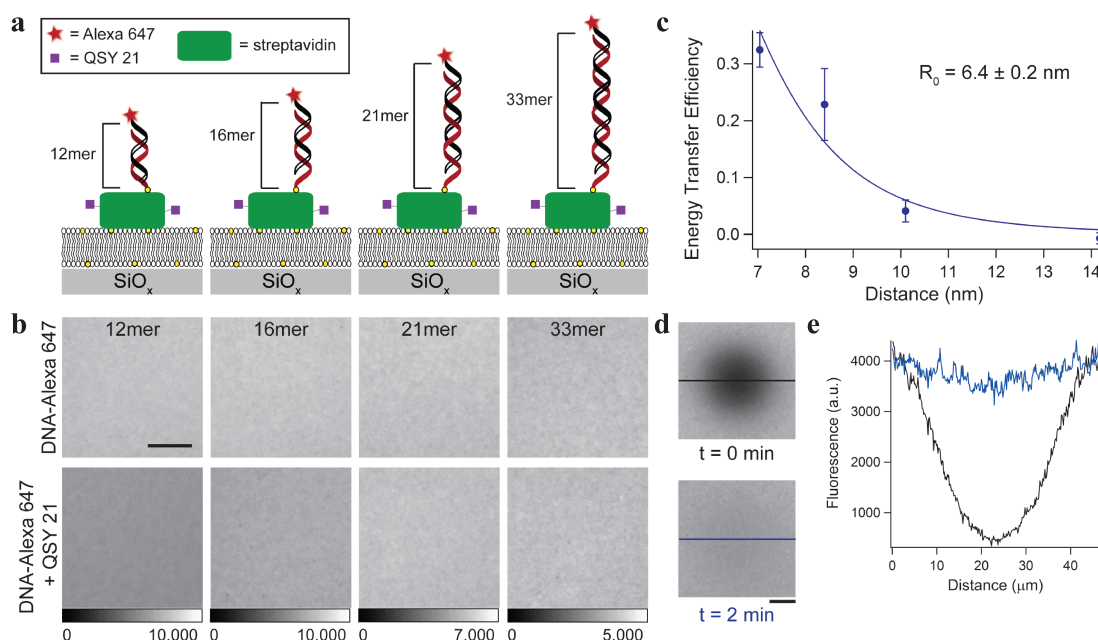


Figure A3.7 Calibration A to obtain the Förster distance of Alexa 647 and QSY21. Four lipid bilayer surfaces (a) were functionalized with QSY21 labeled streptavidin and then incubated with Alexa 647 labeled dsDNA of different lengths. The average fluorescence intensity for donor only surfaces (b, top row) was compared to the fluorescence intensity of surfaces containing both donor and acceptor (b, bottom row) in order to determine the quenching efficiency of the surfaces with varying fluorophore to quencher distances. The resulting efficiencies were then plotted against the known distances (c) and fit to the standard FRET equation to determine a Förster distance (R_0) of $6.4 \pm 0.2 \text{ nm}$. All bilayer

surfaces were tested for lateral mobility using FRAP experiments (d, e). Both scale bars represent 10 μm .

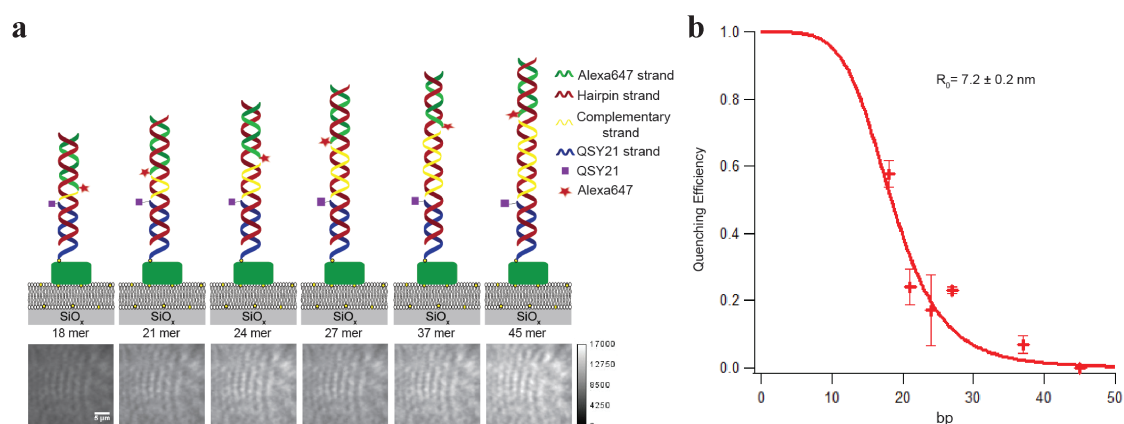


Figure A3.8 Calibration B to obtain the Förster distance of Alexa 647 and QSY21. (a) Scheme of calibration experiment and representative TIRF microscopy images of the six different hairpin oligonucleotides that were hybridized to their complementary strands. (b) Calibration curve showing the quenching efficiency as a function of the number of base pairs separating the fluorophore from the quencher. The data fit an R_0 value of $7.2 \pm 0.2 \text{ nm}$.

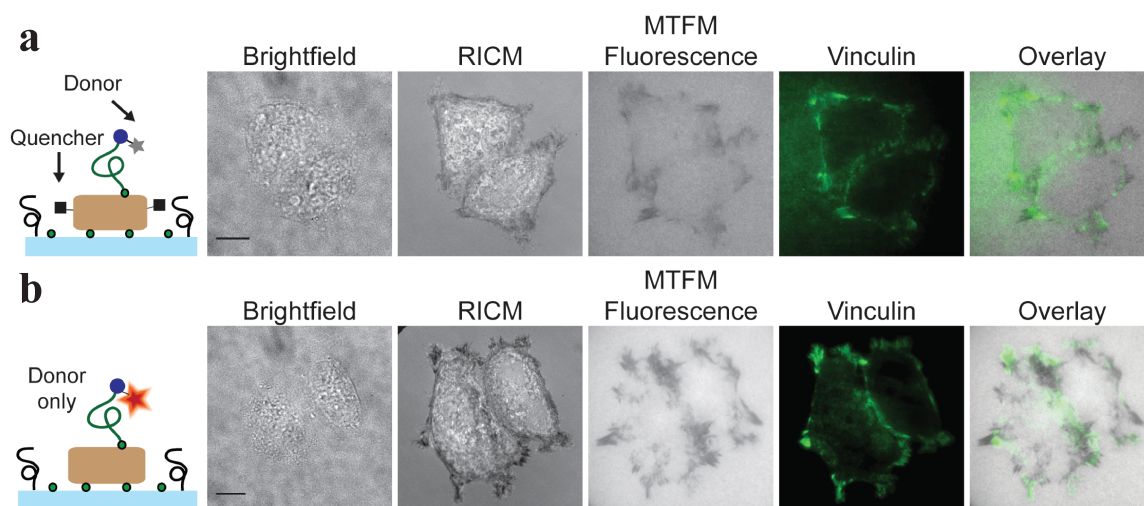


Figure A3.9 Areas of decreased MTFM fluorescence colocalize with focal adhesion proteins. HCC 1143 cells were incubated for 60 min on surfaces (1:1 ratio of APTES:mPEG; 4600 streptavidin molecules/ μm^2) containing streptavidin-QSY21 and cRGDfK(C)-A647-PEG₂₃-biotin and were subsequently fixed and immunostained for the focal adhesion protein vinculin. Scale bars represent 10 μm .

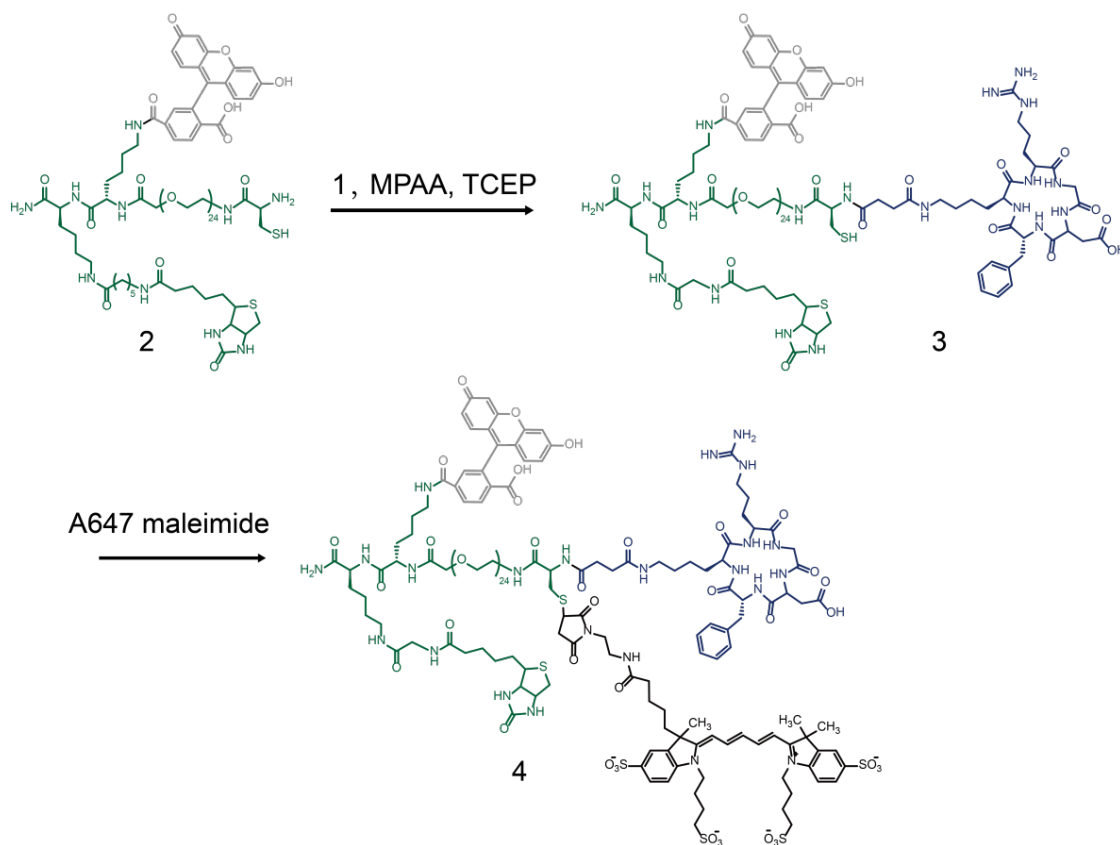


Figure A3.10 Conjugation of cRGDfK α -thioester with fluorescein-PEG₂₄-biotin conjugate and coupling of Alexa 647 as the acceptor fluorophore. Full synthesis is described in the Materials and Methods section.

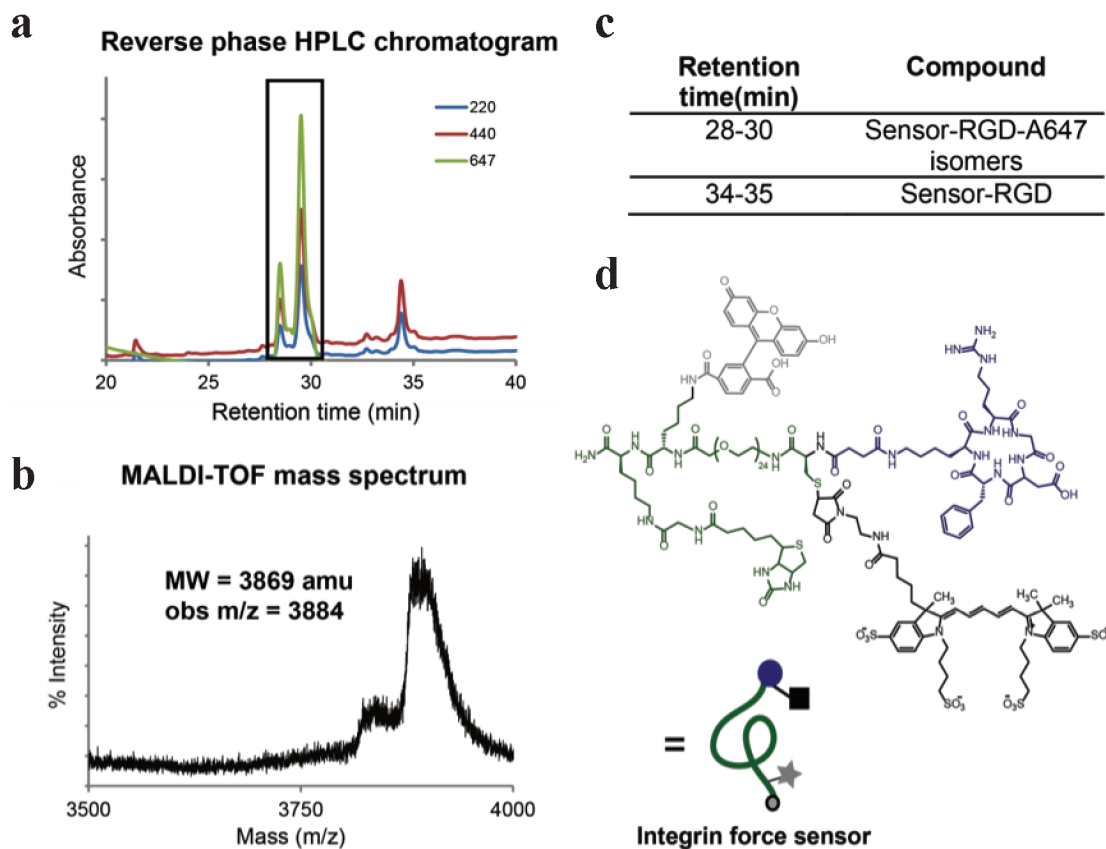


Figure A3.11 Purification and characterization of the cRGDfK-Alexa647-PEG₂₄-fluorescein-biotin conjugate. (a) Reverse phase HPLC chromatogram of the cRGDfK-biotin-PEG₂₄-cysteine, A647 reaction mixture. The absorbance was measured at 220, 440 and 647 nm. 1 ml fractions were collected as they eluted off the column (flow rate = 1 mL/min). The peaks were characterized by MALDI-TOF MS (b) and the final integrin force sensor product ($MW_{\text{obs}} = 3869$; $MW_{\text{expected}} = 3884$) was found to elute at 28-30 min (c). (d) Structure of the final product.

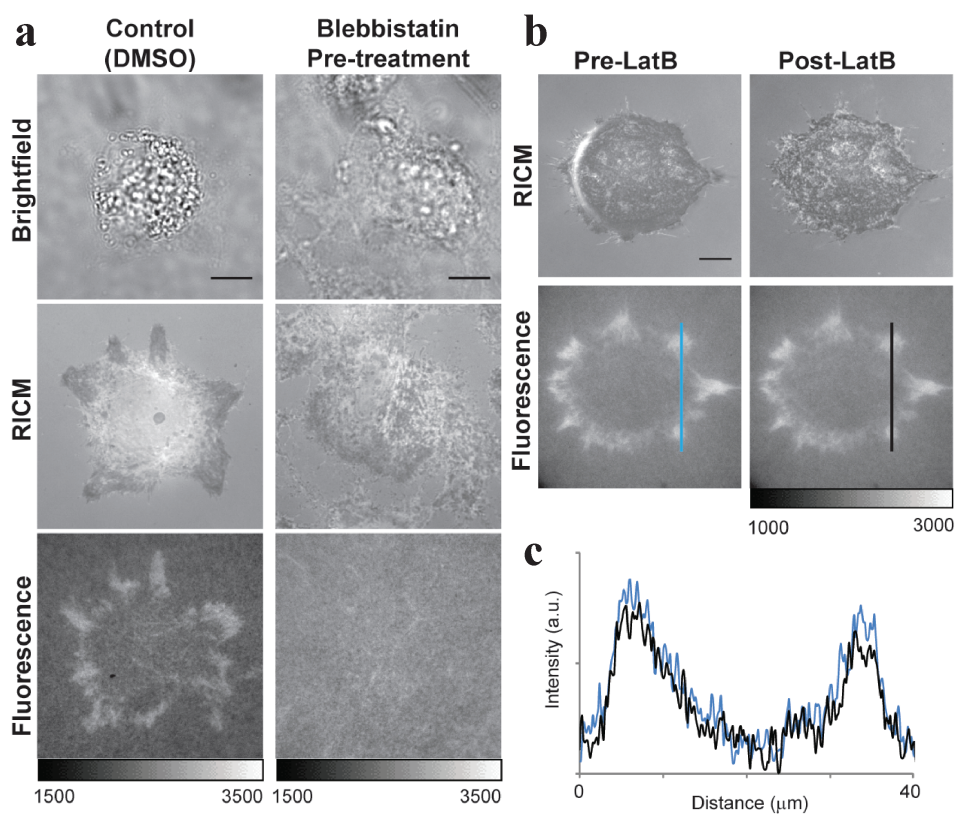


Figure A3.12 Biotin dissociation requires myosin and f-actin. (a) Representative brightfield, RICM, and fluorescence images of cells treated with blebbistatin ($10\ \mu\text{M}$) and incubated on cRGDfK(C)-QSY21-PEG₂₃-biotin MTFM surface for 1 h prior to being fixed and imaged. Control cells incubated with an amount of DMSO equal to that used to add blebbistatin to the treated cells. (b) Representative images of cells allowed to incubate on cRGDfK(C)-QSY21-PEG₂₃-biotin MTFM surface for 30 min, imaged and then treated with $20\ \mu\text{M}$ latrunculinB for 10 min. (c) Intensity profile of cell in (b) before (blue) and after (black) LatB treatment. Scale bars represent $10\ \mu\text{m}$.

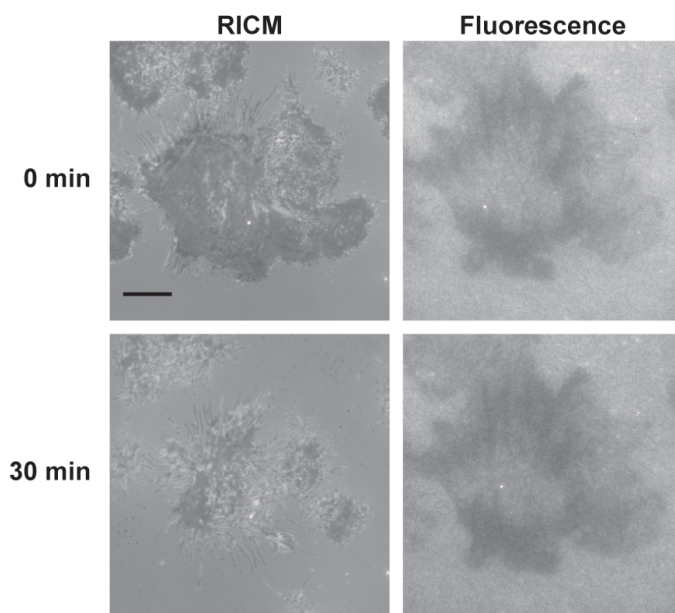


Figure A3.13 Cell dissociation does not reverse negative MTFM signal. Representative RICM and fluorescence images of cells incubated on a cRGDfK-Alexa647-PEG₂₄-fluorescein-biotin MTFM sensor surface (see Figure S8) taken prior to adding soluble cRGD peptide and 30 min after addition. RICM images indicate that cell-surface adhesion is reduced, while the negative MTFM signal remains and even decreases further during the cRGD ligand incubation. Scale bar represents 10 μm .

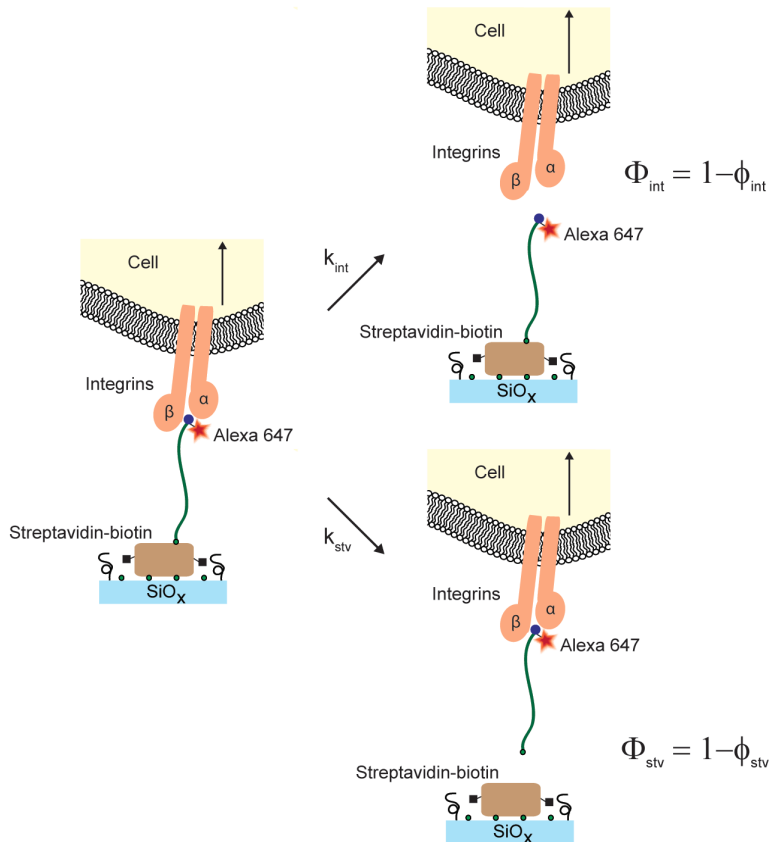


Figure A3.14 When two bonds are found in a series and subjected to an external mechanical load, it is expected that the weaker bond will be more likely to dissociate. The probability of a single bond rupture event primarily depends on two parameters, the k_{off} rate at zero force and the distance required to displace the bond from its equilibrium bound state to the transition state, Δx . Likewise, when two bonds are placed in a series, the probability of weaker bond rupture will depend on the relative values of k_{off} (force = 0) and Δx . In order to more quantitatively calculate the probability of single bond dissociation when two bonds, such as streptavidin-biotin and integrin-ligand, are found in a series and placed under tension, we followed an in depth analysis originally developed by Neuert et al.³⁸. First, we define the survival probability of each bond over time as follows,

Eqn. 4
$$\Phi_{\text{stv}}(t) = 1 - \varphi_{\text{stv}}(t)$$

Eqn. 5
$$\Phi_{\text{int}}(t) = 1 - \varphi_{\text{int}}(t)$$

where Φ_{stv} and Φ_{int} are the probabilities of streptavidin-biotin and integrin-ligand bond survival, respectively, and φ_{stv} and φ_{int} are the probabilities of the respective bonds rupturing. In order to describe bond survivability under force, the Bell model⁴³, is used to reflect the k_{off} rates of the bonds under force,

$$\text{Eqn. 6} \quad k_{\text{int}}(f) = k_{\text{int}}(f = 0) \times e^{f \Delta x_{\text{int}} / k_{\text{B}} T}$$

$$\text{Eqn. 7} \quad k_{\text{stv}}(f) = k_{\text{stv}}(f = 0) \times e^{f \Delta x_{\text{stv}} / k_{\text{B}} T}$$

where f refers to the applied force, Δx_{stv} and Δx_{int} are the distances between the bound state and the transition state for streptavidin-biotin and integrin-ligand association, respectively. k_{stv} and k_{int} are the k_{off} rates for streptavidin-biotin and integrin ligand bonds, respectively. k_{B} is the Boltzmann constant and T is the absolute temperature. **Equations 4** and **5** can then, as described in Neuert et al., be combined with **Equations 6** and **7** to yield a mathematical model to describe the likelihood of bond dissociation under force.

In our case, the two bonds are highly asymmetric where $k_{\text{int}} = 0.072 \text{ s}^{-1}$ ⁵⁵ and $k_{\text{stv}} = \sim 3 \times 10^{-5}$ at $37 \text{ }^\circ\text{C}$ ^{19,20} (**Figure A3.4**). Since the two bonds are linked, both bonds equally experience the applied tension, f . Furthermore, if we assume that $\Delta x_{\text{int}} = \Delta x_{\text{stv}}$, then the likelihood of bond dissociation is force and loading rate independent. In this case, the ratio $k_{\text{stv}}/k_{\text{int}}$ remains constant for all values of f based on **Equations 6** and **7**. Therefore, we can compare the k_{off} values under zero force and determine the probability of bond dissociation under integrin-mediated tension. Using the ratio of the reported off rates, the probability of streptavidin-biotin dissociation while maintaining integrin-ligand association is ~ 0.00003 . This suggests that streptavidin-biotin would need to experience hundreds of thousands of cycles of mechanical force to dissociate through integrin-ligand mediated tension, which is unlikely based on the expected k_{on} values^{55,56} and the reported force oscillation frequency of 0.1 Hz ⁵.

In the situation where Δx of streptavidin-biotin is larger than that of the integrin-ligand bond (which is likely the case), the analysis becomes more complex, as the change in k_{off} becomes loading rate and force dependent. In general, large loading rates and greater magnitudes of tension favor the bond with smaller values of Δx . Nonetheless, in our case, the k_{off} values differ by orders of magnitude and will likely dominate Φ_{stv} .

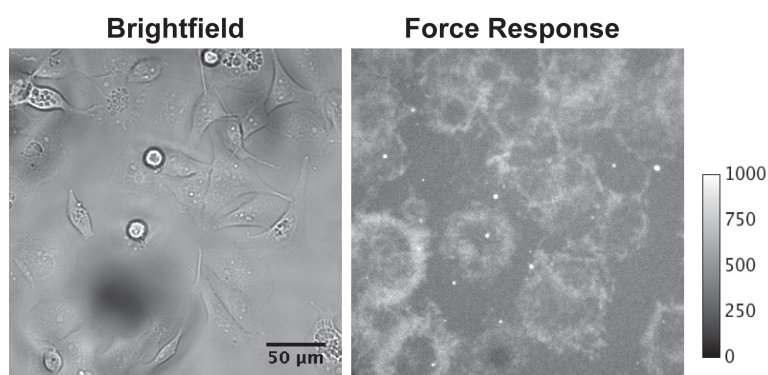


Figure A3.15 Global cell response to integrin MTFM sensor surface for 5 h. HCC 1143 cells were incubated on cRGDFK(C)-QSY21-PEG₂₃-biotin surfaces for 5 h (1:100 ratio of APTES:mPEG; 520 streptavidin molecules/ μm^2) and then imaged at 40x magnification in brightfield and epifluorescence. Fluorescence patterns at the cell edge represent regions of biotin dissociation over time.

Chapter 4: Exploring the mechanotransduction model of Notch receptor activation

4.1 Brief overview of the Notch-Delta system

The Notch receptor is a single-pass transmembrane receptor ubiquitous in multicellular life. It plays a critical role in cellular differentiation both during development and throughout adult life. Notch receptor or ligand mutations can lead to congenital conditions such as Alagille syndrome and are associated with certain forms of cancer, such as T-cell acute lymphoblastic leukemia^{1,2}. Despite the importance and ubiquitous nature of the receptor, the mechanism by which it is activated is still not fully understood.

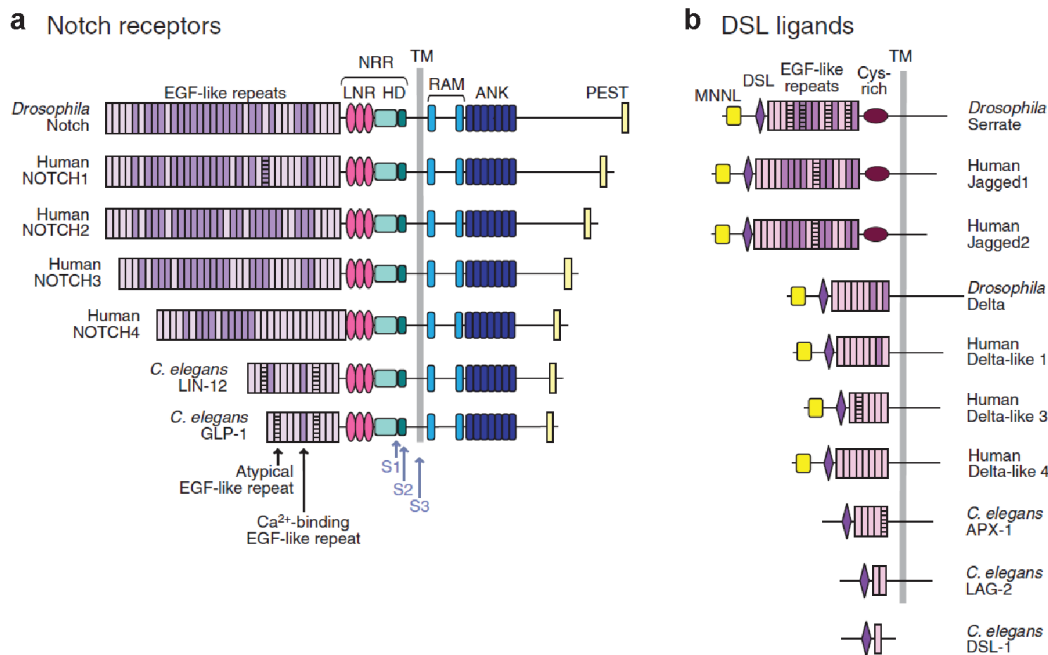


Figure 4.1 Notch receptors and ligands found in *D. melanogaster*, *H. sapiens*, and *C. elegans*. Reproduced with permission from reference 3.

4.1.1 Description of the Notch receptor and its ligands

Notch receptors consist of an intracellular domain (NICD), a transmembrane domain (TM), and an extracellular domain (NECD) (**Figure 4.1a**)³⁻⁵. The NICD includes a RAM domain, a series of seven ankyrin (ANK) repeats, and a PEST domain. The RAM and ankyrin regions play a role in the nucleus after Notch activation and the PEST

domain is responsible for degradation and recycling of the receptor. The TM domain is where the receptor transverses the cell membrane. The NECD is composed of a series of EGF-like repeats, the number of which is dependent on the species and specific Notch homologue. Human Notch1 and 2 and the *Drosophila* Notch receptor contain 36 EGF-like repeats. The portion of the NECD closest to the membrane is referred to as the negative regulatory region (NRR). This region encompasses two metalloprotease cleavage sites (S1 and S2), three Lin-12-Notch (LNR) repeats, three Ca²⁺ binding sites, and a hydrophobic heterodimerization domain (HD) (**Figure 4.2a**).

Notch undergoes several post-translational modifications prior to arrival in the cell membrane. The first of these is the furin-mediated cleavage at S1 that turns Notch into a heterodimeric protein. Additionally, Notch is modified by several *O*- and *N*-glycans along the NECD⁶.

Notch ligands contain a DSL (Delta, Serrate, Lag) domain for Notch binding and, like Notch receptors, they contain at least one EGF-like repeat (**Figure 4.1b**)³⁻⁵. In addition (with the exception of *C. elegans*) Notch ligands contain a module at the N-terminus (MNNL) of the extracellular portion of the ligand. This conserved module has recently been reported to bind to phospholipids and affect Notch activation⁷. Ligands also contain an intracellular PDZ domain, which allows them to bind and interact with the cytoskeleton⁸. Notch ligands are generally divided into two categories, Delta or Delta-like and Jagged/Serrate. The two types of ligands can be differentiated by the cysteine-rich region in the extracellular domain proximal to the membrane that is found only in Jagged/Serrate type ligands.

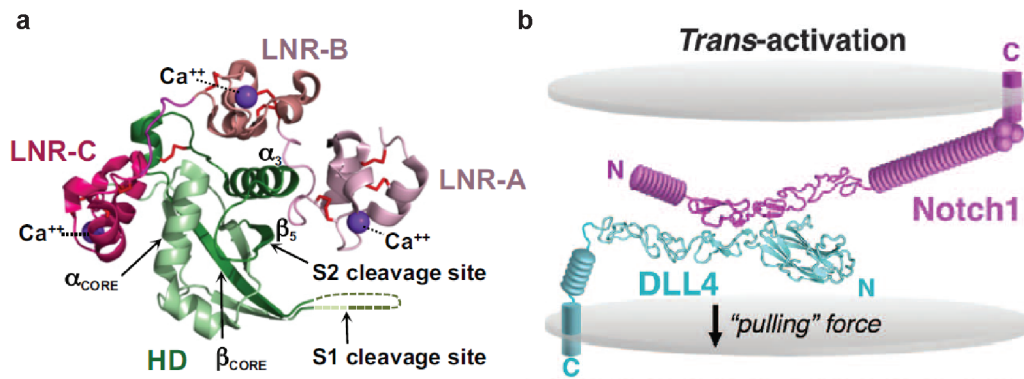


Figure 4.2 Structural aspects of the Notch pathway. a) Crystal structure of Notch NRR. Reproduced from Tiyanont, et al.⁹ and used with permission. b) Structure of Dll4-Notch1 complex showing direction of proposed pulling force on the ligand-bound Notch receptor exerted by ligand expressing cells. Reproduced with permission from reference 18.

4.1.2 Events leading to Notch activation and translocation to the nucleus

It has been well established that Notch-ligand binding is dependent on several structural motifs in the proteins. The Notch-ligand binding site is located on EGF-like repeats 11 and 12 of the NECD. Furthermore *O*-fucose and *O*-glucose modifications on the Notch receptor are known to be necessary for Notch activity by modulating ligand binding affinity⁶. However, regulation of the Notch pathway through receptor glycosylation is complex. For example *O*-fucose modification of the *Drosophila* NECD by OFUT1 (*O*-fucosyltransferase 1) increases the ability of Notch to bind to Serrate, but decreases binding to Delta¹⁰. In contrast, the glycosyltransferase Fringe, known to attach N-acetylglucosamine (GlcNAc) moieties to *O*-fucose modifications on Notch, modulates ligand binding by increasing Notch affinity for Delta and decreasing binding to Serrate¹¹⁻¹³. Furthermore, the effect of GlcNAc modification mediated by the fringe family of glycosyltransferases on Notch receptors also depends on which specific Notch receptor is modified (Notch1 vs Notch2)¹⁴.

On the ligand, side, binding is mediated by the DSL domain. Notch-ligand binding affinity (K_d) ranges are reported from ~ 0.7 nM to $130 \mu\text{M}$ ¹⁵⁻¹⁷. These studies employed different Notch ligands and NECD constructs of different sizes, suggesting that in addition to EGF repeats 11 and 12 other portions of the NECD also contribute to ligand binding. This reportedly low binding affinity motivated the development of a mutant variant of Dll4 in order to obtain a crystal structure of Notch1 bound to Dll4 (**Figure 4.2b**)¹⁸. One aim of this study was to determine whether sugar modifications affect binding by direct interactions at the Notch-ligand binding site or through allosteric changes in the protein structure. The Notch1-Dll4 crystal structure revealed two *O*-linked glycosylations of Notch1 that directly contact the Notch1-Dll4 binding site and two *O*-linked glycosylations distant to the binding interface. Glycosylations found distant from the binding site are thought to enhance receptor susceptibility to metalloprotease cleavage¹⁹. These results indicate that sugar modifications modulate Notch activation in different ways. Interestingly, another finding of this report was that the Notch1-Dll4 crystal complexes tend to form 2:2 dimers, possibly suggesting a role for receptor-ligand oligomerization. However, using light-scattering analysis, Notch1-Dll4 binding in solution was found to be in a 1:1 ratio. Which of these configurations is more biologically relevant will require further experiments.

After ligand binding, Notch is cleaved by an ADAM (a disintegrin and metalloprotease) family metalloprotease at the cell membrane (S2). This cleavage then is followed by a third cleavage by the γ -secretase complex at S3. This final cleavage releases the NICD from the cell membrane and allows it to translocate to the nucleus, where it joins the DNA binding protein CSL (C-promoter-binding factor/Suppressor of

hairless/LAG-1) and the co-activating protein MAM (Mastermind) to form a complex that releases transcriptional inhibition of Notch target genes, such as *Hes-1* and *Hey-1* (Figure 4.3).

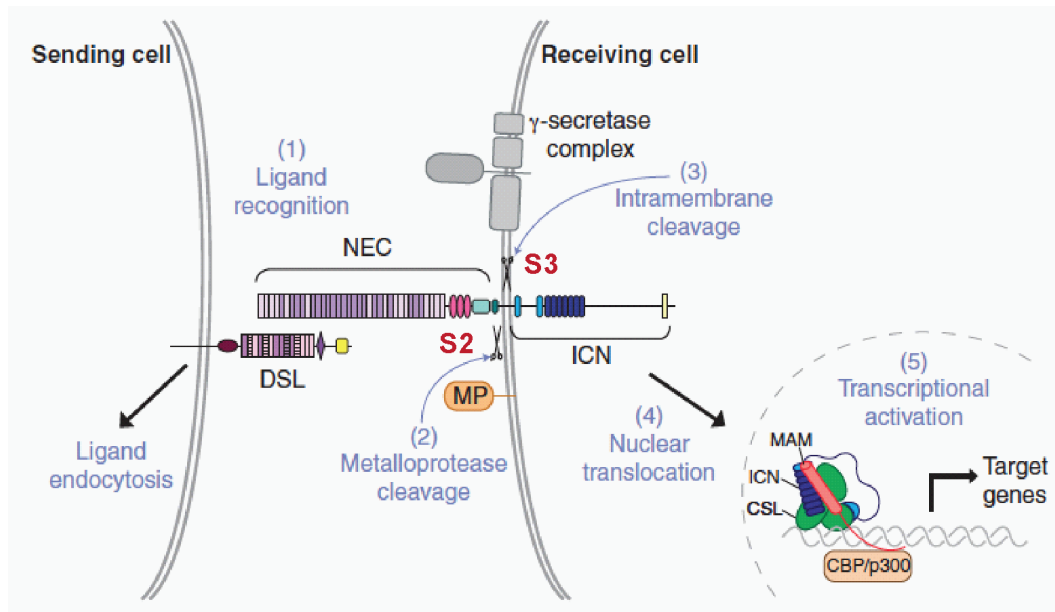


Figure 4.3 Series of events leading to Notch activation and translocation to the nucleus. Activation of the receptor is initiated when the extracellular portion of Notch (NEC) binds to the DSL region of the ligand. This leads to cleavage at S2 by an ADAM family metalloprotease and is followed by a second cleavage at S3 in the membrane by the γ -secretase complex, which releases the intracellular portion of Notch (ICN). The ICN, or NICD, is then translocated to the nucleus where it joins MAM and CSL to relieve transcriptional inhibition of Notch target genes. Note that S1, which is not depicted, occurs before Notch reaches the cell membrane. Adapted from Gordon, et al.³ and used with permission.

4.2 Discussion of proposed mechanisms of Notch activation

There are two proposed models to explain how Notch-ligand interactions lead to Notch activation. Both of these models were developed to explain the finding that endocytosis of ligand-bound Notch by the ligand-expressing cell is a requirement for Notch activation²⁰. It should also be noted that these two models are not mutually exclusive. The first model proposes that ligand recycling through the endocytic pathway

is required to create a mature ligand capable of efficient Notch binding^{21, 22}. The second model proposes that transendocytosis of the Notch-ligand complex by the ligand-expressing cell exerts force on the Notch receptor which results in force-mediated opening of the NRR. This stretching of the NRR unmasks the cleavage site (S2), allowing it to be accessed by the metalloprotease. Several experiments have been shown to support this hypothesis. It has been reported that applying tension to the NRR with an AFM probe allows ADAM17 (tumor necrosis factor α -converting enzyme, TACE) or ADAM10 to cleave Notch at S2²³. Additional work using optical tweezers with Dll1-expressing cells reported that endocytosis of ligand bound Notch results in a pulling force of ~ 19 pN per receptor-ligand bond and that this force is dependent on proteins which are characteristic of clathrin-mediated endocytosis^{24, 25}. More recent work reports that the Notch NRR is sensitive to ADAM17-mediated cleavage in the range of 3.5 to 5.4 pN²⁶. Notch activation in lower force regimes is further supported by work using a tension gauge tether (TGT)²⁷. In this system, Notch-expressing cells containing a fluorescent reporter to detect activation were incubated on DNA-based tension gauge surfaces. The DNA was tuned to tolerate tension values of either 12 pN or 58 pN. It was reported that activation of Notch occurred on both TGT surfaces with 12 and 58 pN tension tolerance values, suggesting that if force is required for activation, it is less than 12 pN in magnitude.

4.3 Development of an MTFM probe to study Notch activation

In order to explore the activation of the Notch receptor, a molecular tension probe was developed that allowed for the attachment of a large protein to a flexible linker anchored to a substrate. The probe contained attachment sites for a pair of spectrally matched chromophores that could act as a FRET-based output to signal force-mediated

extension of the linker. Due to the size of the NECD and the sensitivity of ligand binding to receptor orientation²⁸, it was important that the protein be attached site-specifically. Furthermore, in order to ensure a high quenching efficiency (QE) in the absence of applied force, which improves sensor output in response to tension, the fluorophores were also site-specifically located.

4.3.1 DNA-based MTFM Notch probes

Two different types of MTFM probes were used to explore mechanotransduction in the Notch-Delta system. Both probes were functionalized with recombinant human Notch1 extracellular domain (NECD, extending from the N-terminus to the 13th EGF-like repeat, amino acids 1-526) fused to a fluorescent protein, either mCherry or eGFP depending on the requirements of the experiment (**Figure 4.4a**). This recombinant protein also contained a site for enzymatic biotinylation by the birA enzyme and a 10x histidine tag for purification purposes. The first probe design contained a 3-stranded DNA hairpin, which was anchored to a glass slide through biotin-streptavidin binding (**Figure 4.4b**). Given that forces between Notch and its ligand are thought to be in the range of ~ 5 pN²⁶, a DNA hairpin sensor developed by Zhang, et al.²⁹ was used for all Notch MTFM experiments. This hairpin has a calibrated force requirement at which 50% of the hairpins unfold ($F_{1/2}$) under 4.7 pN of tension. The DNA hairpin was hybridized to two shorter DNA oligomers. The lower oligomer contained a 5' biotin group for anchoring the duplex to the surface and a 3' amine for conjugation with the non-fluorescent acceptor (quencher) QSY21. The top oligomer was functionalized with a 5' amine for coupling with an Atto 647N fluorophore and a 3' biotin. This 3' biotin group

allowed a second streptavidin protein to be used to bind the biotinylated NECD-fluorescent protein fusion.

An alternate version of the MTFM probe was developed in response to difficulties encountered in consistently reproducing the streptavidin anchored MTFM surfaces. The updated MTFM probe (**Figure 4.4c**) contained the same hairpin construct as the initial sensor but was anchored to a gold nanoparticle (AuNP) on the glass surface through gold-thiol binding. This method of anchoring the sensor was initially developed by Liu, et al^{30,31}. Attachment of the NECD was achieved through biotin-streptavidin binding in the same manner as the initial streptavidin anchored system.

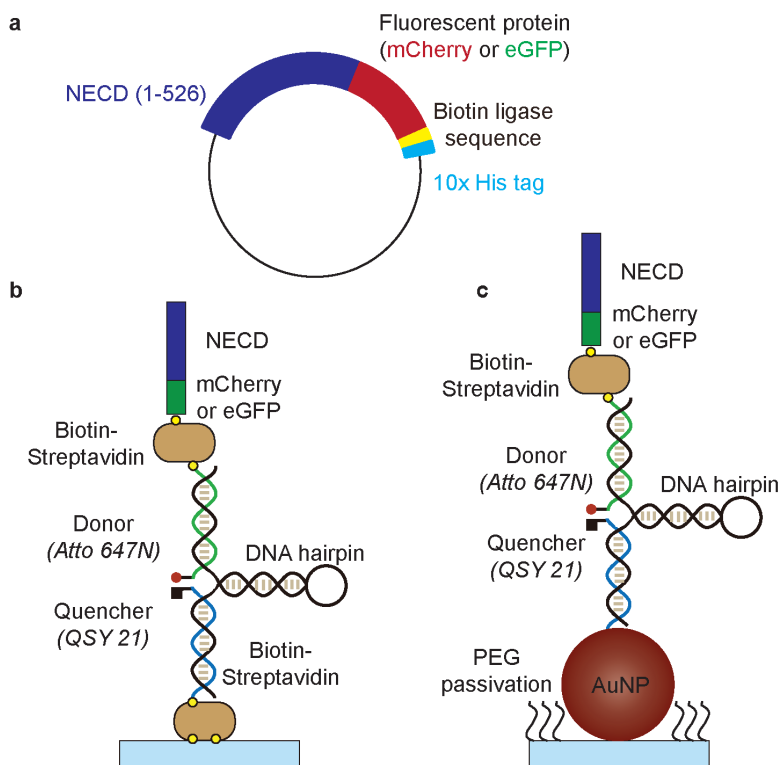


Figure 4.4 Design of two MTFM probes used to explore Notch mechanotransduction by ligand expressing cells. a) General construct of the plasmid used to express recombinant NECD. b) Schematic of streptavidin anchored DNA hairpin MTFM Notch probe c) Schematic of AuNP anchored DNA hairpin MTFM Notch probe

4.3.2 Binding of Dll1-expressing cells to a recombinant Notch 1 extracellular domain

Before testing Dll1-expressing cells on the MTFM probe, the ability of cells to bind and interact with the recombinant NECD was confirmed. Initially, a NECD-mCherry construct was expressed via baculovirus-mediated transfection of Sf9 insect cells. However, when this recombinant NECD protein was bound to supported lipid bilayer (SLB) surfaces, Dll1-eGFP expressing cells did not bind or interact efficiently with the receptor (**Figure 4.5**). Fluorescence imaging of NECD-mCherry confirmed its presence on the lipid surface (**Figure 4.5a**). T-Rex-CHO-K1 cells permanently transfected with a tetracycline inducible (TO) Dll1-mCherry construct (developed by Sprinzak, et al.³²) were seeded on lipid surfaces containing NECD-mCherry, cyclic RGD (cRGD), or both and only bound to surfaces containing cRGD (**Figure 4.5 b, c**) regardless of Dll1-mCherry expression. This suggests that cellular integrins were able to bind the cRGD ligand but Dll1 did not bind the NECD.

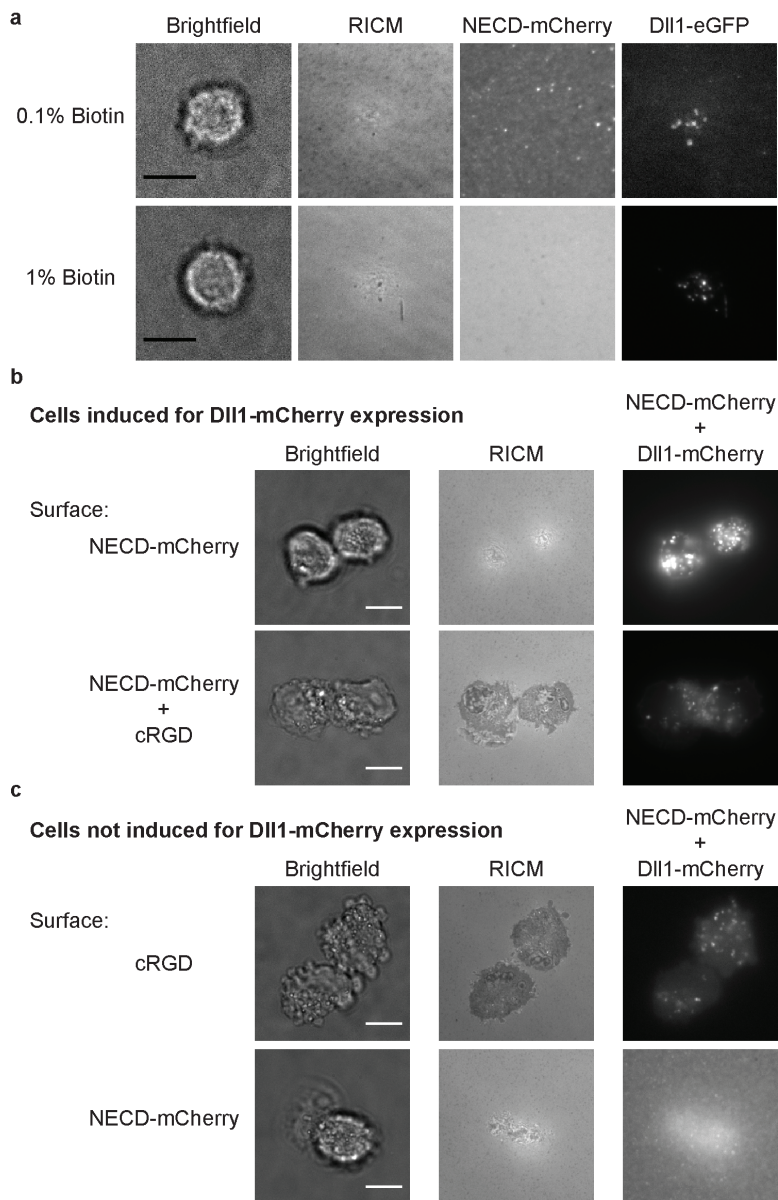


Figure 4.5 Binding of Dll1-expressing cells to recombinant NECD-mCherry expressed by Sf9 cells. a) Mouse Ltk- cells expressing Dll1-GFP adhere poorly to NECD-mCherry expressed by Sf9 insect cells and bound to lipid bilayer surfaces via biotin-streptavidin. Increasing the ligand density by increasing the surface biotinylated lipid density did not improve cell binding. b) T-Rex-CHO-K1 cells containing a tetracycline-inducible (TO) Dll1-mCherry protein (developed by Sprinzak, et al.³²) also failed to bind to NECD-mCherry expressed by Sf9 insect cells. However, when cRGD-biotin was present on the lipid surfaces cells were able to bind and spread. Note that in (b) and (c) the NECD-mCherry on the surface and the Dll1-mCherry are observed in the same fluorescence channel and therefore cannot be distinguished. Scale bar represents 10 μm .

Sf9 insect cells are capable *O*- and *N*-linked glycosylations that are similar to that of mammalian cells^{33, 34}. However, in light of the poor binding to the surface observed with the NECD expressed by Sf9 cells and the known importance of post-translational glycosylation for Notch-ligand binding, a mammalian expressed recombinant NECD was tested for cell binding. The NECD, a commercially available Fc chimera (R and D Systems), was randomly labeled with Cy5 using N-hydroxysuccinimide (NHS)-ester chemistry and bound to the lipid surface via a biotinylated (also randomly coupled via NHS-ester chemistry) protein A/G. Then TO-Delta cells induced to express Dll1-mCherry were incubated on the surface and compared to cells not expressing the ligand (**Figure 4.6**). Cell binding was markedly improved on the NECD-Fc coated lipid surfaces over surfaces containing Sf9 expressed NECD. However, the NECD-Fc chimera presents a NECD dimer to the cells and protein A/G, which contains several Fc binding domains, creates clusters of these dimers. Therefore, it is difficult to determine whether the increase observed in cell binding was due to pre-clustering of the NECD, increased density of the receptor, or specific differences in the characteristics of the mammalian expressed receptor protein versus the Sf9 expressed protein.

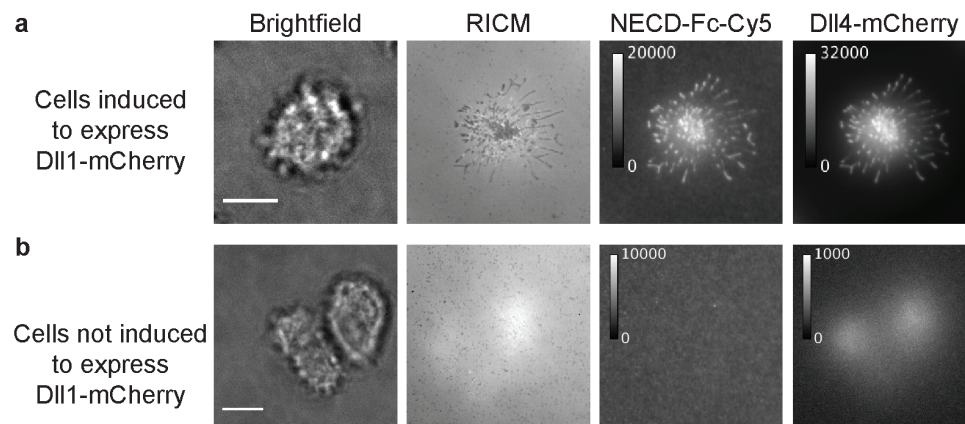


Figure 4.6 Binding of Dll1-mCherry expressing cells to recombinant NECD-Fc chimera expressed by mammalian cells. a) Induction of Dll1-mCherry expression by treatment

with 1 $\mu\text{g/ml}$ doxycycline resulted in cell binding to the NECD-Fc-Cy5 surface. Dll1-mCherry is also seen to correlate with clustered NECD-Fc-Cy5. b) When expression of Dll1-mCherry was not induced, cells do not bind to the NECD-Fc-Cy5 surface. Scale bar represents 10 μm .

4.3.3 Differentiating the effects of clustering and density in Dll1-expressing cells

binding to NECD surfaces

In order to determine the mechanism behind enhanced cell binding for the NECD-Fc compared to the Sf9 expressed NECD, mammalian HEK293FT cells were used to express a monomeric NECD-mCherry protein. The aim was to better understand the role of NECD clustering and determine the best expression system for the recombinant protein. Monomeric NECD-mCherry was bound to Ni-NTA functionalized supported lipid bilayers (SLBs) through a 10x histidine tag at the C-terminus. Dll1-mCherry expressing (TO-Delta) cells were then incubated on lipid surfaces containing 0.4%, 1%, or 4% Ni-NTA lipids (**Figure 4.7a, b**). Quantitative analysis of the degree of cell spreading on each surface (**Figure 4.7c**), revealed similar results when comparing the two surfaces. However, when the fluorescence intensity under the same imaging conditions of the various surfaces were considered, the NECD-mCherry density was greater on Sf9 expressed NECD surfaces (**Figure 4.7d**). This data shows that Dll1-expressing cells are able to bind to NECD expressed by Sf9 or HEK293FT cells and that binding is highly dependent on ligand density. The data also suggests that cell binding is far more sensitive to NECD-mCherry expressed by HEK293FT cells. Therefore, in future experiments

mammalian HEK293FT expressed recombinant NECD is used for MTFM surfaces.

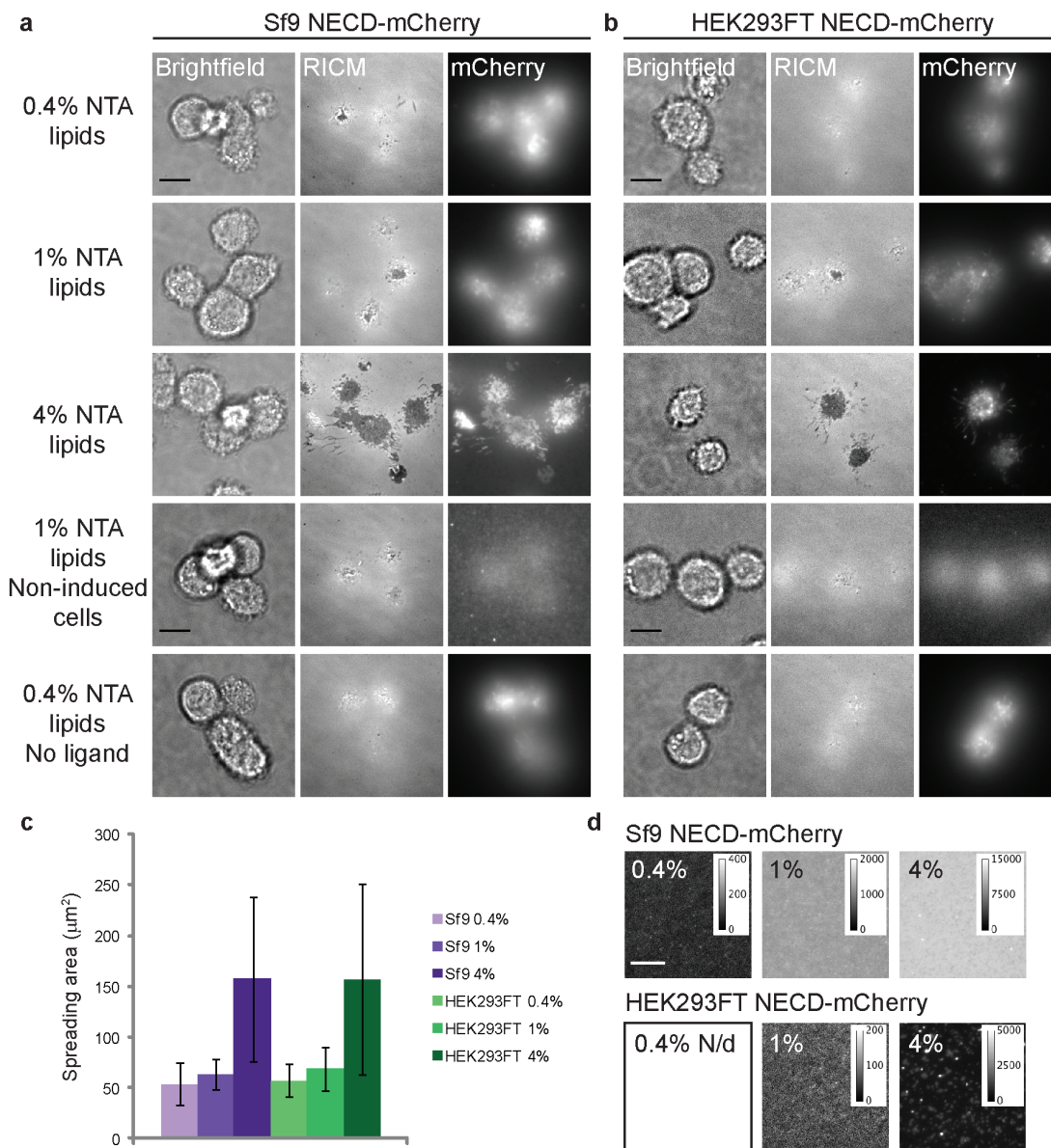


Figure 4.7 Ligand density affects the degree of binding to NECD coated lipid surfaces. a) Representative brightfield, RICM, and fluorescence images of Dll1-mCherry expressing cells interacting with Sf9 expressed NECD-mCherry on lipid surfaces. b) Representative brightfield, RICM, and fluorescence images of Dll1-mCherry expressing cells interacting with mammalian (HEK293FT) expressed NECD-mCherry on lipid surfaces. c) Quantitative analysis of cell binding area on Sf9 expressed NECD-mCherry (purple) and HEK293FT expressed NECD-mCherry (green) surfaces. d) Fluorescence intensity of Sf9 expressed NECD-mCherry surfaces (top) and HEK293FT expressed NECD-mCherry surfaces (bottom) taken with the same exposure time and microscope settings. Surfaces containing the HEK293FT NECD-mCherry were so dim at 1% and 4% Ni-NTA lipids that no image was obtained for the 0.4% surface. All scale bars represent 10 µm.

4.4 Testing the ability of Dll1-expressing cells to exert a force on the Notch receptor

Once Dll1-expressing cells reliably bound to recombinant NECD functionalized lipid surfaces, the ability to exert force on the Notch receptor was tested. Initially, streptavidin anchored MTFM probes (**Figure 4.4b**) were used for tension-sensing experiments. However, experimental challenges led to adapting the AuNP anchored MTFM probe (**Figure 4.4c**).

4.4.1 The streptavidin anchored DNA-based MTFM Notch sensor

As an initial test to measure mechanical forces applied across the Notch-ligand bond, Ltk- cells expressing unlabeled Dll1 were added to streptavidin anchored MTFM probe (**Figure 4.4b**) surfaces. Results showed that cells bound to NECD-eGFP MTFM surfaces (**Figure 4.8**) and after 35 min an increase in fluorescence was observed under the cells (**Figure 4.8a**). These results support the hypothesis that Dll1-expressing cells apply ≥ 4.7 pN of tension to the Notch receptor. Cells that are allowed to incubate for longer times exhibit greater fluorescent signal in the MTFM sensor channel (**Figure 4.8b**), suggesting that more hairpin sensors are unfolded. In the absence of quencher, a decrease in fluorescence was observed under attached cells (**Figure 4.8c**). This fluorescence decrease is likely due to shearing or unzipping of the hybridized DNA and removal of the upper DNA arm containing the Atto647N fluorophore. It may also be due to dissociation of the biotin-streptavidin bond anchoring the probe to the surface, although this is unlikely based on the high degree of affinity observed for this bond compared to the low affinity reported for Notch-ligand binding. Either scenario, however, suggests that tension applied by the Dll1-expressing cells may exceed 4.7 pN. In the

absence of ligand, cells are not able to bind to the surface and fluorescence intensity is unchanged (**Figure 4.8d**).

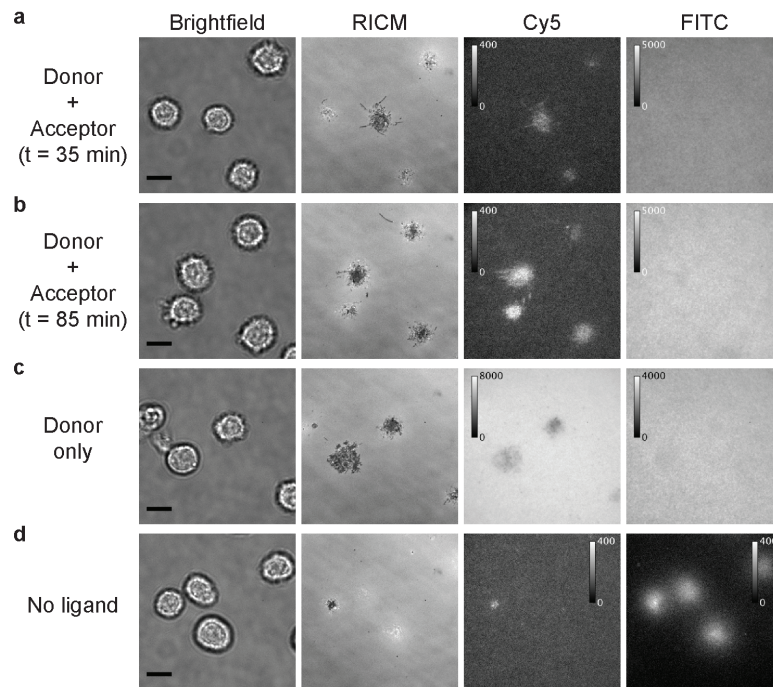


Figure 4.8 Unlabeled Dll1-expressing cells on streptavidin anchored MTFM surfaces exhibit positive fluorescence signal. a) Representative brightfield, RICM, and epifluorescence images of Ltk- cells expressing unlabeled Dll1 incubated on MTFM probe surfaces. Increased fluorescence under cells in the sensor (Cy5) channel indicates a force equal to or greater than 4.7 pN is being applied to the probes. This signal was observed within 35 minutes of cells being added to the surface. b) MTFM probe surfaces on which Ltk- cells were allowed to incubate for 85 min appear to exhibit increased fluorescence intensity. c) MTFM probe surfaces that lack the quencher create areas of decreased fluorescence under the cells, indicating that all or part of the MTFM probe is being removed from the surface. d) Surfaces containing the DNA probe without an attached NECD ligand do not allow for cell binding. All scale bars represent 10 μm .

Initial experiments were performed using Ltk- cells expressing unlabeled Dll1 ligands, however, to correlate the positive Notch MTFM signal with ligand-receptor interactions experiments using Dll1-mCherry expressing (TO-Delta) cells needed to be performed. However, difficulty in consistently reproducing streptavidin anchored MTFM

surfaces led to an examination of the streptavidin anchored MTFM probe surface. For example, **Figure 4.9** shows a streptavidin anchored MTFM surface on which the fluorescently labeled DNA-based probe is bound at a very low density as evidenced by the low fluorescence intensity of the surface. Additionally, it was found that, despite passivation of the surface with the inert protein bovine serum albumin (BSA) and the addition of free biotin to block available streptavidin binding sites prior to *in situ* hybridization of the biotinylated upper DNA strand, a large portion of the NECD-eGFP was non-specifically bound to the surface (**Figure 4.9**). As a result of these findings, an alternate version of MTFM probe was employed to explore tension in the Notch-Delta pathway.

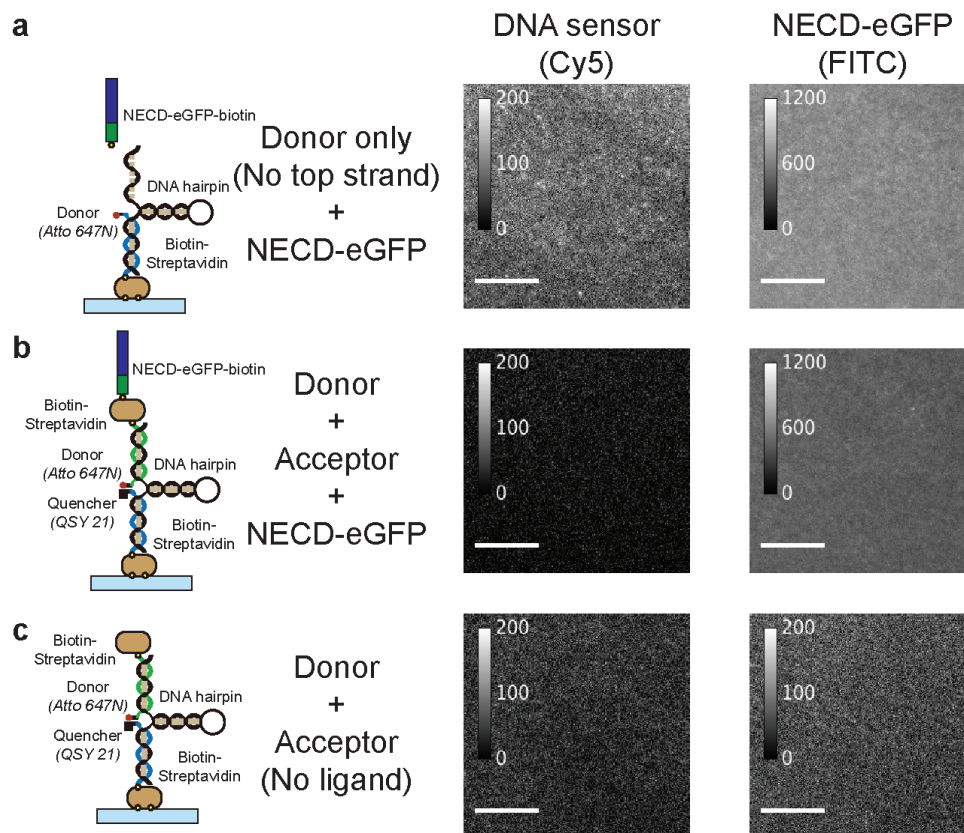


Figure 4.9 Non-specific binding of NECD to streptavidin anchored MTFM surfaces. a) The streptavidin anchored Notch MTFM probe containing only the donor fluorophore and lacking the upper biotinylated DNA strand was placed on a glass slide. Imaging in the Cy5 channel revealed low fluorescence intensity despite the absence of quencher, suggesting poor sensor binding. Image in the FITC channel shows NECD-eGFP added to the surface binds despite the absence of the upper biotinylated DNA strand. b) Fully functionalized (containing donor and acceptor) MTFM probes on surface exhibit the same amount of NECD-eGFP fluorescence as surface lacking a specific NECD-eGFP-biotin binding site. c) MTFM probes (containing donor and acceptor) without the NECD-eGFP ligand. Scale bars represent 10 μm .

4.4.2 The AuNP anchored DNA-hairpin MTFM sensor

The AuNP anchored MTFM probe (**Figure 4.4c**) has several advantages over the streptavidin-anchored probe. First, it addresses the issue of non-specific binding by passivating the glass surface with methoxy-capped PEG polymers. Second, by using gold-thiol chemistry to anchor the DNA hairpin, the possibility of biotin or streptavidin binding to the wrong layer of the sensor is eliminated due to the orthogonal attachment method for binding the upper and lower DNA sites. Finally, the AuNP acts as a second fluorescence quencher, thus increasing the quenching efficiency of the probe in the absence of tension.

This updated tension sensor appeared to minimize the problem of non-specific protein binding, however, a new issue became apparent when imaging TO-Delta cells with Atto647N labeled sensors and NECD-eGFP. As shown in **Figure 4.10**, the bright Dll1-mCherry in TO-Delta cells results in spectral bleedthrough into the MTFM sensor channel. In order to address the challenge of imaging MTFM surfaces in three fluorescence channels without bleedthrough contamination obscuring the MTFM sensor signal, a new optical configuration was used to image the AuNP MTFM probe surfaces (**Figure 4.11**).

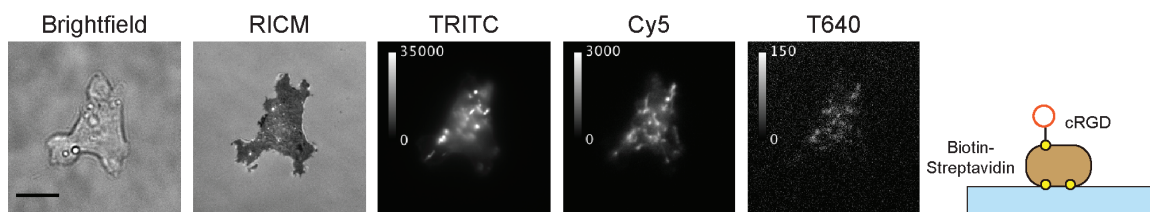


Figure 4.10 Bleedthrough occurs from Dll1-mCherry into the sensor channel. Dll1-mCherry cells plated on surfaces containing cRGD-biotin bound to unlabeled streptavidin attached to glass slide covalently modified with biotin. Bleedthrough in the epifluorescence Cy5 channel is more pronounced than bleedthrough seen with T640 imaging. Scale bar represents 10 μm .

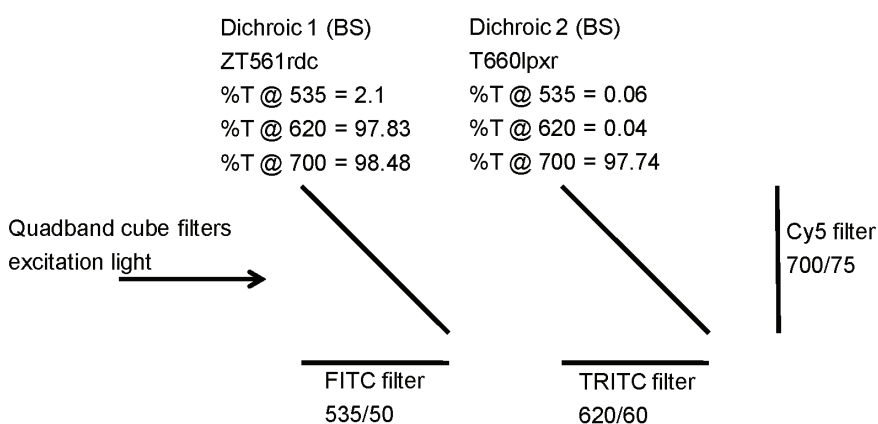


Figure 4.11 Updated optical configuration for correction of spectral bleedthrough. Laser excitation light is filtered through a TIRF quadband cube, which allows transmission of all three fluorescence emission wavelengths. Emission light then passes through two bandsplitters (BS), which are placed into an OptoSplit III image splitter. The first BS transmits wavelengths greater than ~ 535 nm and reflects ~ 535 nm light through the FITC emission filter and to the CCD camera. The second BS reflects light that is less than ~ 700 nm to the TRITC emission filter and transmits wavelengths greater than ~ 620 nm to be filtered by the Cy5 emission filter.

The optical configuration described in **Figure 4.11**, was tested for spectral bleedthrough by imaging three different SLB surfaces composed of the fluorescent proteins and dye used in MTFM Notch cell experiments. One surface was functionalized with NECD-eGFP through biotin attachment to unlabeled streptavidin on the surface. Another SLB contained Dll1-mCherry and was also attached via biotin-streptavidin binding. On the third surface, Atto647N labeled streptavidin was present. These three

surfaces were then imaged using the new optical set-up. Fluorescence bleedthrough was measured as the ratio of emission intensity when the surface was excited with the laser wavelength for the channel being tested for bleedthrough and when the surface was excited with the laser corresponding to the excitation wavelength of the surface fluorophore. For example, to test for bleedthrough from the mCherry protein into the 640 nm channel, the Dll1-mCherry functionalized surface was excited by the 640 nm laser and the fluorescence emission of the resulting image was divided by the emission of the same surface when excited by the 561 nm laser. In this way, as shown in **Table 4.1**, the spectral bleedthrough from each fluorophore into the other two imaging channels was determined. Results indicated that the largest amount of bleedthrough occurs in the 488 nm channel and comes from the mCherry fluorophore. This is not an issue since the bleedthrough is relatively small and the 488 channel is used to observe the NECD-eGFP, primarily to simply confirm its presence on the surface. Bleedthrough into the 640 nm channel, from either NECD-eGFP or the Dll1-mCherry is so small that it is insignificant and thus effectively eliminates the possibility of spectral bleedthrough producing a false positive signal in the MTFM sensor channel.

Surface fluorophore	BT into 488 channel	BT into 561 channel	BT into 640 channel
NECD-eGFP	N/a	0.009%	0.0008%
Dll1-mCherry	1.5%	N/a	0.03%
Streptavidin-Atto647N	0.03%	0.15%	N/a

Table 4.1 Percentage of spectral bleedthrough observed when imaging single fluorophore functionalized surfaces.

With the issue of spectral bleedthrough resolved, the next step was to test for mechanical tension with Dll1-mCherry expressing cells on an MTFM AuNP anchored

surfaces. To this end, TO-Delta cells were induced for Dll1-mCherry expression, incubated on a AuNP-MTFM surface and imaged using the updated optical configuration. **Figure 4.12a** shows a representative cell interacting with NECD-eGFP on the surface after a 30 min incubation period. In **Figure 4.12b**, the same cell is followed over the course of 5 min. Bright fluorescent spots of DLL1-mCherry correlated with spots of increased fluorescence in the MTFM sensor channel. These areas of correlated fluorescence appear at several time points within the observed time frame. Specific spots have been pointed out at $t = 80$ s (yellow arrow), $t = 160$ s (white arrowhead), and $t = 260$ s (red arrow). This dynamic correlation of Dll1-mCherry fluorescence and MTFM fluorescence suggests that clustered regions of the Dll1 ligand are exerting at least 4.7 pN of force on the NECD. These results further support the hypothesis that ligand-expressing cells apply tension to the Notch receptor.

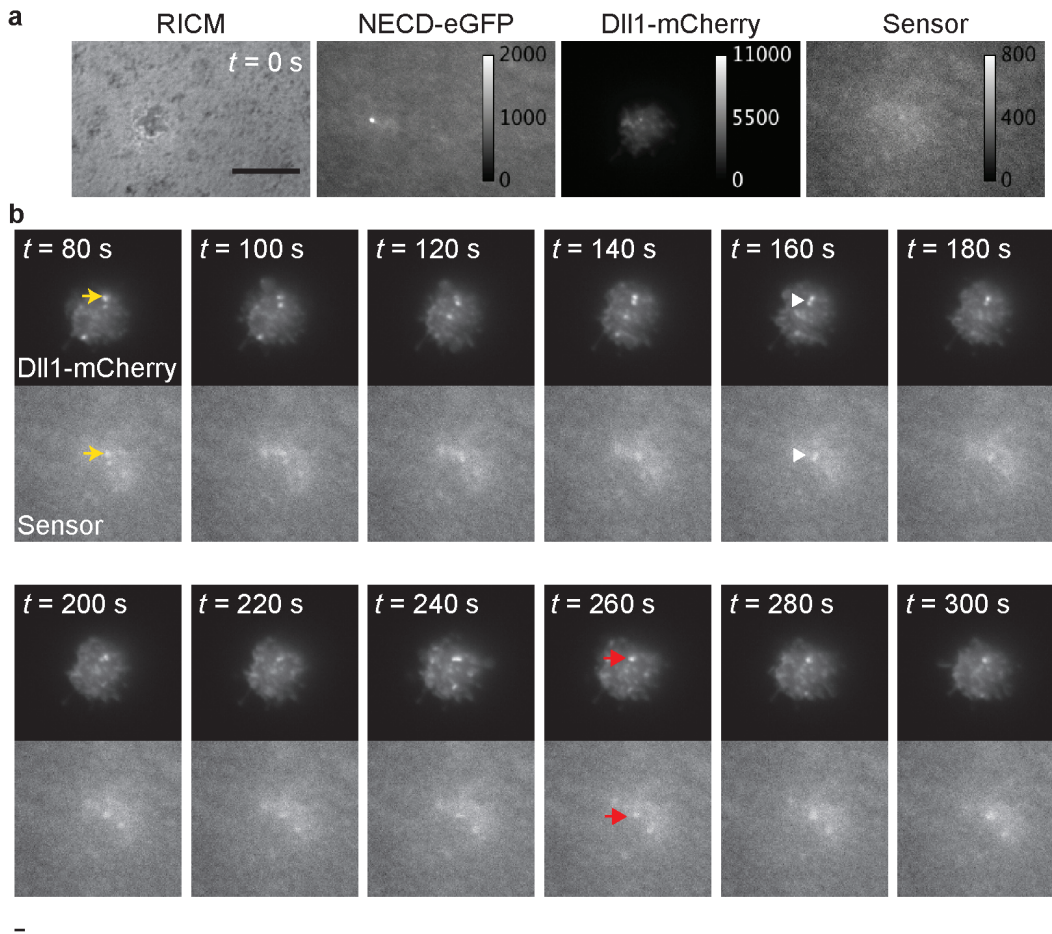


Figure 4.12 Dll1-mCherry bound to NECD-eGFP on AuNP MTFM surface exhibits positive tension signal. a) Images of Dll1-mCherry expressing cell on AuNP-DNA MTFM surface at the start of imaging ($t = 0$) after 30 min. incubation on the surface. b) The Dll1-mCherry and MTFM sensor signal in the same cell as in (a) is imaged over the course of 5 min. Yellow arrow at $t = 80$ s, white arrowhead at $t = 160$ s, and red arrow at $t = 260$ s highlight regions at which Dll1-mCherry fluorescence correlates to NECD MTFM sensor tension. Scale bar represents 10 μm .

In order to confirm that Dll1-mediated tension on the NECD-eGFP is common to other Dll1-expressing cells, Ltk- cells expressing unlabeled Dll1 were also tested on the AuNP anchored MTFM surfaces. Since these cells do not express mCherry labeled Dll1, the imaging method did not require the quadband cube or the image splitter. Instead, images were obtained using standard TIRF microscopy methods.

The results of these experiments, shown in **Figure 4.13**, reveal that ligand-expressing cells remove the fluorescently labeled sensor construct from the surface. This occurs when cells are plated on a fully functional AuNP anchored sensor surface (**Figure 4.13a**), on a surface that contains the donor and quencher labeled DNA linker but lacks the extendable hairpin loop (**Figure 4.13b**), and on surfaces where the NECD-eGFP is not present (**Figure 4.13c**). These results suggest that cells are able to non-specifically bind to the MTFM sensor surface and that removal of the NECD-eGFP and sensor construct is not likely to be driven by specific Dll1 interactions with the NECD.

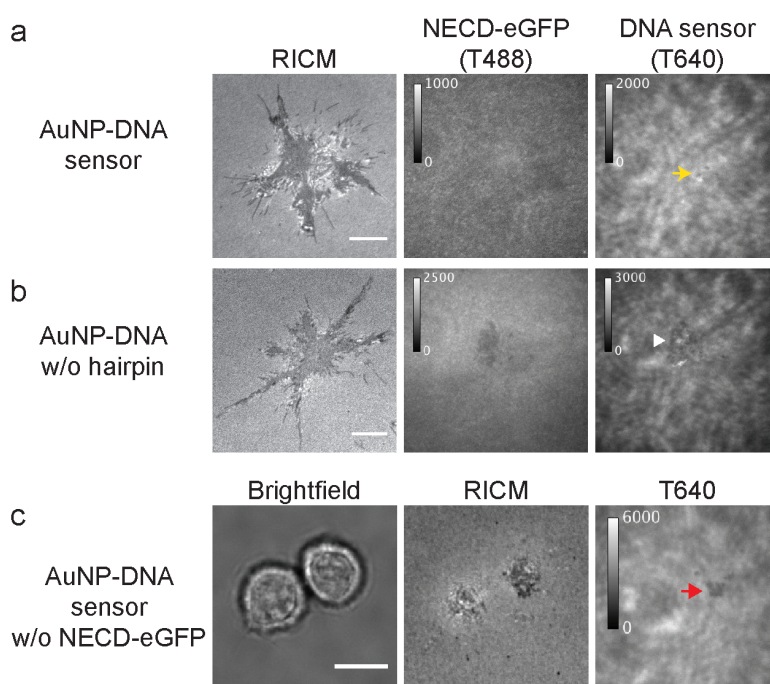


Figure 4.13 Unlabeled Dll1 expressing cells appear to remove MTFM probe from the surface. a) After a 30 min incubation on a AuNP-DNA MTFM surface, surface bound Ltk- cells expressing unlabeled Dll1 exhibit regions of diminished fluorescence under the cell in both the NECD-eGFP channel and the DNA sensor channel. b) On AuNP anchored surface containing a DNA sensor construct that lacks the hairpin, cells produce the same darkened regions of fluorescence as in (a). c) Ltk- cells expressing unlabeled Dll1 are able to bind the AuNP anchored MTFM surface even in the absence of the NECD-eGFP. Regions of decreased fluorescence in the DNA sensor channel also occur under these bound cells. Scale bars represent 10 μ m.

4.5 Conclusions

The results of experiments using both the streptavidin anchored MTFM Notch sensor and the AuNP anchored MTFM Notch sensor suggest that Dll1 expressing cells apply a mechanical force to the Notch receptor. However, difficulties in reliably repeating experimental results on MTFM surfaces limit the conclusions that can be drawn. Further experiments would benefit from a more robust surface preparation method that consistently provides effective passivation to prevent non-specific binding of proteins and cells.

4.6 Materials and methods

4.6.1 Cell Culture

Ltk- mouse cells permanently transfected to express either unlabeled Dll1 or Dll1-eGFP (a gift from G. Weinmaster) were cultured in Dulbecco's modified Eagle's medium (DMEM, Mediatech) supplemented with 10% fetal bovine serum (FBS) (Mediatech), L-glutamine (2.5 mM, Mediatech), penicillin G (100 IU/ml, Mediatech), and streptomycin (100 mg/ml, Mediatech). TO-Delta cells (a gift from M. Elowitz) were cultured in Alpha MEM Earle's Salts (Irvine Scientific) supplemented with 10% fetal bovine serum (FBS) (Mediatech), L-glutamine (2.5 mM, Mediatech), penicillin G (100 IU/ml, Mediatech), and streptomycin (100 mg/ml, Mediatech), Blastidin (10 µg/mL), Geneticin (600 µg/mL), Zeocin (400 µg/mL) and hygromycin (500 µg/mL) (Life Technologies). Cells were induced for Dll1-mCherry expression by the addition of doxycycline (1 µg/mL) 24 – 36 h prior to cell experiment. HEK 293FT cells were cultured in DMEM (Mediatech) supplemented with 10% FBS (Mediatech), nonessential amino acids (1%), L-glutamine

(2.5 mM, Mediatech), penicillin G (100 IU/ml, Mediatech), streptomycin (100 mg/ml, Mediatech), and Geneticin (500 µg/mL). All cells were incubated at 37 °C with 5% CO₂ and passaged at 70–80% confluency.

4.6.2 Insect cell (Sf9) transfection and expression of NECD-mCherry

Expression of NECD-mCherry in Sf9 insect cells was mediated by a baculovirus expression vector system (BD Biosciences). The NECD-mCherry fusion sequence was cloned (Emory Cloning Center) into a pVL1393 plasmid and used for Sf9 cell transfection according to manufacturers instructions. After initial baculovirus propagation, subsequent Sf9 flasks were treated with 1.5 mL of cell media containing the virus in order to transfect a new flask for protein expression.

4.6.3 Mammalian cell (HEK293FT) transfection

HEK293FT cells were transiently transfected with either NECD-mCherry or NECD-eGFP fusion proteins through a calcium phosphate transfection method protocol developed by G. Weinmaster. The NECD construct was cloned (Emory Cloning Center) into a pcDNA3 plasmid (Life Technologies). This construct (10 µg) was then diluted in 450 µl of Nanopure water, 500 µl of 2x HBS (Hepes buffered salt) solution, and 50 µl of 2.5 M CaCl₂. The transfection mixture was added to a 10 cm culture dish containing HEK293FT cells, allowed to incubate for 16 h, then rinsed with DMEM lacking serum or phenol red, and allowed to express protein for five days. Typically, 10 – 20 culture dishes were transfected per batch of NECD protein.

4.6.4 Purification and biotinylation of expressed proteins

Five days after initial transfection, cell media was collected from all transfected flasks and centrifuged (5,000 rpm, 5 min) to remove any residual cells. Supernatant was

concentrated by filtration through a 50 mL, 30 kDa MWCO filter (Amicon) using repeated cycles of centrifugation (4,000 x g, 7 – 12 min) until a final volume of ~ 1 mL was reached. Magnetic Ni-NTA coated beads (Qiagen) were then added to the concentrated supernatant and allowed to incubate on a rotating platform for 30 – 60 min at room temperature and protected from light. Beads were then washed and eluted according to manufacturers instructions. Elution was buffer exchanged into Tris using a 1 mL, 30 kDa MWCO filter (Amicon). The NECD protein construct was then biotinylated using the birA enzyme (Gencopoeia) according to manufacturers instructions, and exchange to PBS after the reaction was complete.

4.6.5 Synthesis of synthetic lipid bilayer surfaces

Lipids consisted of 1,2-dioleoyl-*sn*-glycero-3-phosphocholine (DOPC, Avanti Polar Lipids) and either 1,2-dioleoyl-*sn*-glycero-3-phosphoethanolamine-N-(cap biotinyl) (sodium salt) (DPPE-biotin, Avanti Polar Lipids) or 1,2-dioleoyl-*sn*-glycero-3-[(N-(5-amino-1-carboxypentyl)iminodiacetic acid)succinyl] (nickel salt) (DOGS NTA, Avanti Polar Lipids) depending on the experiment. After being mixed in the correct proportions in chloroform, lipids were dried with a rotary evaporator and placed under a stream of N₂ to ensure complete evaporation of the solvent. Lipids were then resuspended in Nanopure water and subjected to three freeze-thaw cycles by alternating immersions in an acetone and dry ice bath and a warm water bath (40 °C). To obtain small unilamellar vesicles, lipids were extruded through a high-pressure extruder with a 100 nm nanopore membrane (Whatman).

Supported lipid bilayers were assembled by adding small unilamellar vesicles to base-etched 96-well plates with glass-bottomed wells. After blocking with BSA (0.1

mg/ml) for 30 min, 50 mM NiCl₂ was added to the wells in Tris buffer and 300 mM NaCl for 10 min. Wells were rinsed 3 times with 5 ml of the Tris, 300 mM NaCl buffer then incubated with 100 nM NECD-mCherry for 1 h and rinsed 3 times with 5 ml of Tris, 300 mM NaCl buffer before imaging.

4.6.6 Synthesis of streptavidin anchored MTFM surfaces

The glass substrates were covalently functionalized with biotin following literature precedent^{35,36}. Briefly, glass coverslips (number 2, 25 mm diameter; VWR) were sonicated in Nanopure water for 15 min and etched in piranha (3:1 mixture of sulfuric acid (AR ACS, Macron Chemicals) and 30% hydrogen peroxide) for 15 min. Warning: piranha is extremely corrosive and may explode if exposed to organics. The coverslips were thoroughly rinsed with Nanopure water and then placed into three successive wash beakers containing ethyl alcohol (200 proof, Decon Labs, King of Prussia, PA). Next, coverslips were placed into a beaker containing 43 mM silane (3-aminopropyltriethoxysilane (APTES) solution in ethanol. After 1 h immersion in the silane solution, slides were submerged in three separate beakers filled with ethanol, rinsed with additional ethanol, and then dried under a stream of ultrahigh purity N₂. Substrates were then baked in an oven at ~100 °C for 15–30 min. After cooling, the slides were incubated with NHS-biotin (Thermo Fisher) at 2 mg/ml in DMSO overnight at room temperature. Substrates were then rinsed with ethanol, dried under N₂, and stored at room temperature until used for sensor preparation.

The biotin functionalized slides were placed into cell chambers (attofluor chambers, Life Technologies), rinsed with 50 ml of Nanopure water, and then 50 ml of PBS, pH 7.4. To minimize nonspecific protein adsorption, surfaces were incubated with

100 µg/ml bovine serum albumin (BSA) (OmniPur BSA, Fraction V; EMD Chemicals) at room temperature for 1 h. The chamber was rinsed with 50 ml PBS, pH 7.4 and streptavidin was added to a final concentration of 47 nM. After 1 h incubation, the chamber was rinsed with 50 ml PBS, pH 7.4, and pre-hybridized DNA consisting of the biotin-tagged anchoring arm and the DNA hairpin was added to the surface. Chamber was rinsed again with 50 ml PBS after 1 h and 100 nM D-biotin was added (for 1h) to block any remaining streptavidin binding sites. Chamber was then rinsed with 50 ml PBS and the remaining DNA strand was allowed to hybridize to the sensor *in situ* for 2 h. After rinsing with another 50 ml of PBS, streptavidin was added to the surface at a concentration of 47 nM for 1 h. The chamber was then rinsed with 50 ml PBS and the NECD construct was added to a final concentration of 100 nM, allowed to incubate for 1 h and the surface was given a final rinse with 50 ml PBS.

4.6.7 Synthesis of AuNP-DNA MTFM surfaces

To synthesize the AuNP anchored MTFM surfaces, glass coverslips were functionalized in a similar fashion as described for the streptavidin anchored MTFM surfaces. For the AuNP surfaces, silanization was accomplished by using 3-aminopropyltrimethoxysilane (APTMS) instead of APTES and performed in acetone rather than ethanol. To the resulting amine functionalized surface 5 mg of mPEG (2000 MW) and 0.5 mg of lipoic acid-PEG was added to the surface in 0.1M NaHCO₃ and left at 4 °C overnight. Excess PEG was then rinsed off the slides with Nanopure water and 200 µl of AuNPs (9 nm in diameter) was incubated on the slide for 30 min, then rinsed with Nanopure water. The pre-hybridized DNA-sensor construct was then added to the surface (200 nM in 1M NaCl) and left at 4 °C overnight. Unbound DNA was then rinsed

from the surface with PBS and strepavidin to a final concentration of ~200 nM was added to the surface for 30 min. After rinsing with PBS, the NECD construct (100 nM) was incubated on the surface for 1 h, then the surface was rinsed with PBS and imaged.

4.6.8 Microscopy methods

An Eclipse Ti microscope driven by the Elements software package (Nikon) was used for all imaging experiments. The microscope features an Evolve electron multiplying charge-coupled device (EMCCD; Photometrics), an Intensilight epifluorescence source (Nikon), a CFI Apo 100 (numerical aperture (NA) 1.49) objective (Nikon), and a total-internal reflection fluorescence (TIRF) launcher with three laser lines (Coherent): 488 nm (10 mW), 640 nm (20 mW), and 561 nm (50 mW). This microscope also includes the Nikon Perfect Focus System, an interferometry-based focus lock that allowed the capture of multipoint and time-lapse images without loss of focus. The microscope was equipped with the following Chroma filter sets: TIRF 488, TIRF 640, Cy5, TRITC, FITC and reflection interference contrast microscopy (RICM).

To prevent bleedthrough when imaging three fluorescent wavelengths, a quadband cube (Chroma) was used to filter excitation wavelengths and an OptoSplit III (Cairn) equipped with Chroma Cy5, TRITC, and FITC emission filters (**Figure 4.11**) was used to filter fluorescence emission.

4.7 References

1. Penton, A.L., Leonard, L.D. & Spinner, N.B. Notch signaling in human development and disease. *Semin. Cell Dev. Biol.* **2012**, *23*, 450-457.
2. Ranganathan, P., Weaver, K.L. & Capobianco, A.J. Notch signalling in solid tumors: a little bit of everything but not all the time. *Nature* **2011**, *11*, 338-351.

3. Gordon, W.R., Arnett, K.L. & Blacklow, S.C. The molecular logic of Notch signaling - a structural and biochemical perspective. *J. Cell Sci.* **2008**, *121*, 3109-3119.
4. Kopan, R. & Ilagan, M.X.G. The canonical Notch signaling pathway: Unfolding the activation mechanism. *Cell* **2009**, *137*, 216-233.
5. Chillakuri, C.R., Sheppard, D., Lea, S.M. & Handford, P.A. Notch receptor-ligand binding and activation: Insights from molecular studies. *Semin. Cell Dev. Biol.* **2012**, *23*, 421-428.
6. Takeuchi, H. & Haltiwanger, R.S. Significance of glycosylation in Notch signaling. *Biochem. Biophys. Res. Comm.* **2014**, *453*, 235-242.
7. Chillakuri, C.R. et al. Structural analysis uncovers lipid-binding properties of Notch ligands. *Cell Rep.* **2013**, *5*, 861-867.
8. D'Souza, B., Miyamoto, A. & Weinmaster, G. The many facets of Notch ligands. *Oncogene* **2008**, *27*, 5148-5167.
9. Tiyanont, K. et al. Evidence for increased exposure of the Notch1 metalloprotease cleavage site upon conversion to an activated conformation. *Structure* **2011**, *19*, 546-554.
10. Okajima, T., Xu, A. & Irvine, K. Modulation of Notch-ligand binding by protein O-fucosyltransferase 1 and Fringe. *J. Biol. Chem.* **2003**, *278*, 42340-42345.
11. Panin, V.M., Papayannopoulos, V., Wilson, R. & Irvine, K. Fringe modulates Notch-ligand interactions. *Nature* **1997**, *387*, 908-912.
12. Moloney, D.J. et al. Fringe is a glycosyltransferase that modifies Notch. *Nature* **2000**, *406*, 369-375.

13. Bruckner, K., Perez, L., Clausen, H. & Cohen, S. Glycosyltransferase activity of Fringe modulates Notch-Delta interactions. *Nature* **2000**, *406*, 411-415.
14. Hicks, C. et al. Fringe differentially modulates Jagged1 and Delta1 signalling through Notch1 and Notch2. *Nat. Cell Biol.* **2000**, *2*, 515-520.
15. Cordle, J. et al. Localization of the Delta-like-1-binding site in human Notch-1 and its modulation by calcium affinity. *J. Biol. Chem.* **2008**, *283*, 11785-11793.
16. Shimizu, K. et al. Mouse Jagged1 physically interacts with Notch2 and other Notch receptors. *J. Biol. Chem.* **1999**, *274*, 32961-32969.
17. Shimizu, K., Chiba, S., Saito, T., Kumano, K. & Hirai, H. Physical interaction of Delta1, Jagged1, and Jagged2 with Notch1 and Notch3 receptors. *Biochem. Biophys. Res. Comm.* **2000**, *276*, 385-389.
18. Luca, V.C. et al. Structural basis for Notch1 engagement of Delta-like 4. *Science* **2015**, *347*, 847-853.
19. Acar, M. et al. Rumi is a CAP10 domain glycosyltransferase that modifies Notch and is required for Notch signaling. *Cell* **2008**, *132*, 247-258.
20. Parks, A.L., Klueg, K.M., Stout, J.R. & Muskavitch, M.A.T. Ligand endocytosis drives receptor dissociation and activation in the Notch pathway. *Development* **2000**, *127*, 1373-1385.
21. Wang, W. & Struhl, G. Drosophila Epsin mediates a select endocytic pathway that DSL ligands must enter to activate Notch. *Development* **2004**, *131*, 5367-5380.
22. Yamamoto, S., Charng, W.-L. & Bellen, H.J. Endocytosis and intracellular trafficking of Notch and its ligands. *Curr. Top. Dev. Biol.* **2010**, *92*, 165-200.

23. Stephenson, N.L. & Avis, J.M. Direct observation of proteolytic cleavage at the S2 site upon forced unfolding of the Notch negative regulatory region. *Proc. Natl. Acad. Sci. U.S.A.* **2012**, *109*, E2757-E2765.
24. Shergill, B., Meloty-Kapella, L., Musse, A.A. & Weinmaster, G. Optical tweezers studies on Notch: Single-molecule interaction strength is independent of ligand endocytosis. *Develop. Cell* **2012**, *22*, 1313-1320.
25. Meloty-Kapella, L., Shergill, B., Kuon, J., Botvinick, E. & Weinmaster, G. Notch ligand endocytosis generates mechanical pulling force dependent on dynamin, epsins, and actin. *Develop. Cell* **2012**, *22*, 1299-1312.
26. Gordon, W.R. et al. Mechanical allostery: Evidence for a force requirement in the proteolytic activation of Notch. *Develop. Cell* **2015**, *33*, 729-736.
27. Wang, X. & Ha, T. Defining single molecular forces required to activate integrin and Notch signaling. *Science* **2013**, *340*, 991-994.
28. Narui, Y. & Salaita, K. Membrane tethered Delta activates Notch and reveals a role for spatio-mechanical regulation of the signaling pathway. *Biophys. J.* **2013**, *105*, 2655-2665.
29. Zhang, Y., Ge, C., Zhu, C. & Salaita, K. DNA-based digital tension probes reveal integrin forces during early cell adhesion. *Nat. Commun.* **2014**, *5*, 5167.
30. Liu, Y., Yehl, K., Narui, Y. & Salaita, K. Tension sensing nanoparticles for mechano-imaging at the living/nonliving interface. *J. Am. Chem. Soc.* **2013**, *135*, 5320-5323.
31. Liu, Y. et al. Nanoparticle tension probes patterned at the nanoscale: Impact of integrin clustering on force transmission. *Nano Lett.* **2014**, *14*, 5539-5546.

32. Sprinzak, D. et al. Cis-interactions between Notch and Delta generate mutually exclusive signalling states. *Nature* **2010**, *465*, 86-90.
33. Gaunitz, S. et al. Mucin-type proteins produced in the *Trichoplusia ni* and *Spodoptera frugiperda* insect cell lines carry novel *O*-glycans with phosphocholine and sulfate substitutions. *Glycobiology* **2013**, *23*, 778-796.
34. Shi, X. & Jarvis, D.L. Protein N-glycosylation in the Baculovirus-insect cell system. *Curr. Drug Targets* **2007**, *8*, 1116-1125.
35. Stabley, D.R., Jurchenko, C., Marshall, S.S. & Salaita, K.S. Visualizing mechanical tension across membrane receptors with a fluorescent sensor. *Nat. Methods* **2012**, *9*, 64-67.
36. Clack, N.G., Salaita, K. & Groves, J.T. Electrostatic readout of DNA microarrays with charged microspheres. *Nat. Biotech.* **2008**, *26*, 825-830.

Chapter 5: Summary and future directions

5.1 Summary

The centerpiece of this thesis is the development of a new class of molecular tension probes to image receptor forces in living cells. These new probes represent an initial first step toward the ultimate goal of elucidating the interplay between molecular recognition and mechanics in cell biology. The thesis also shows the logical progression toward generating more sophisticated probes tailored toward each pathway of interest. Taken together, the thesis describes the application of MTFM probes to observe and quantify receptor-mediated forces at the cell membrane in the integrin and EGFR pathways.

The initial design for MTFM probes utilized a biotin-streptavidin anchoring method, a flexible PEG linker, and a fluorophore-quencher pair that was randomly coupled to the streptavidin anchoring protein and the protein ligand presented to the cell receptor. As described in Chapter 2, application of this probe to study the molecular force involved in endocytosis of the ligand-bound EGFR led to the finding that during endocytosis cell receptors exert pN range tension on their bound ligands¹. These experiments also presented the first proof-of-principle for the viability and utility of MTFM probes. Although our initial tension probes were directed toward the EGFR pathway, the success of this initial probe led to the development of a new generation of MTFM probes that were then refined and tailored toward alternate pathways.

In Chapter 3, an updated probe design addressed limitations of the initial MTFM probe. Site-specific, orthogonal coupling of the fluorophore and the PEG linker to a cRGD ligand reduced the degree of error that random coupling of the fluorophore-quencher pair introduced into the force measurements and ensured that ligand molecules

were properly oriented for receptor binding to the surface². The biotin-streptavidin anchoring method in this updated sensor remained the same as in the initial MTFM probe. The biotin-streptavidin bond is widely considered to be the most stable, high affinity non-covalent bond in nature and thus is a gold standard in cell biology research, often used to capture and immobilize proteins of interest. However, we found that integrins in focal adhesions were able to dissociate the sensor from the surface by mechanically disrupting this bond. These results indicate that cellular adhesion forces transmitted through individual integrin receptors are larger than initially estimated. Additionally, enhanced stability in focal adhesion contacts may be related to the clustering of integrin receptors in FAs and the synergistic effect of the macromolecular assembly of adapter proteins that connect integrins to the cytoskeleton. Also, we learned that anchoring the MTFM probes via non-covalent protein interactions is not sufficient stable for studying cellular forces and specifically cell adhesion forces.

In Chapter 4, two types of MTFM probes were described that allowed conjugation of the large (~90 kDa) NECD-eGFP protein to the sensor. This was achieved through site-specific incorporation of biotin to the C-terminus of the recombinant NECD-eGFP, which was subsequently used for binding to a DNA-based MTFM probe. Coupling of the fluorophore-quencher pair to a DNA hairpin allowed for greater quenching efficiencies, thus resulting in lower background and a more sensitive tension probe (~30-fold vs ~10-fold fluorescence increase over background)³ than had been achieved with previous designs. This effect was augmented by the use of a gold nanoparticle surface, which provided additional quenching to the dye and further lowering the background signal. In addition, by replacing the entropic PEG spring with a DNA hairpin, the response

threshold of the probe could be tuned by changing the GC content of the DNA hairpin. This allowed for facile tuning of the force at which 50% of the hairpin will unfold ($F_{1/2}$)⁴. Finally, by anchoring the probe to a gold nanoparticle using the thiol-gold bond rather than biotin-streptavidin, the MTFM sensor was more stable under applied force. Despite this much-improved probe, we did not obtain direct evidence showing that the Notch receptor experiences pN range forces during ligand-receptor binding and activation.

5.2 Future directions

5.2.1 Advancing the MTFM probe design

Future versions of the MTFM probe would likely benefit from additional modifications. First, covalent attachment to the surface would create a stable anchoring system that could withstand any biological scale force exerted through a single receptor-ligand complex. For example, a new approach utilizing HaloTag technology⁵ to covalently immobilize a tension sensor was recently used to study integrin-mediated tension⁶. This approach required designing a unique plasmid coding for a linear RGD ligand, a protein-based flexible linker, a modified HaloTag protein, and a site for incorporating an unnatural amino acid. The resulting protein was then expressed, purified, modified, and covalently attached to a surface functionalized with the HaloTag ligand. Although effective, this approach is complicated, challenging, and limited to the use of protein constructs. In order to use PEG- or DNA-based tension sensors, this method would need to be adapted or an entirely different method would need to be employed. Development of such a method would eliminate the need for using biotin-streptavidin binding to anchor the probe, which is labile and not suitable for adhesion

receptors and for long-term (>24 h) force imaging experiments that may become useful in studying cell development and wound healing processes.

Second, a reliable method to covalently couple large proteins to the flexible linker would expand the scope of signaling pathways that could be explored using MTFM. This would require the tension probe to be modified at four unique sites, one site each for the two chromophores, a site for anchoring to a surface, and a site where a recombinant protein could bind. This is a challenging endeavor. The aforementioned HaloTag method, or similar technology, could address this challenge. However, it would not provide a complete solution for working with PEG- or DNA-based probes. The DNA-based MTFM sensor described in Chapter 4 bound the large NECD-eGFP construct to a DNA oligomer via biotin-streptavidin binding. If the tension between Notch and its ligand is on the order of ~5 pN as has been reported⁷, then this attachment method may be sufficient. However, if this or other biological ligand-receptor interactions employ forces large enough to disrupt non-covalent binding then covalent attachment methods will need to be used.

5.2.2 Clustering and force

Another challenge for studying receptor-mediated forces is the unknown role that receptor clustering may play in molecular tension. In all the experiments described herein, the MTFM probes are anchored to a substrate that does not allow for lateral mobility and clustering. This immobilization is necessary to prevent increases in fluorescence due to an increase in local concentration of fluorophores, which would obscure the FRET readout of the force probe. However, in light of the important role that oligomerization plays in receptor signaling and cell biology, the ideal molecular tension

sensor would be capable of differentiating clustering from tension and thus deconstructing the interplay between clustering receptor mechanics.

To address the role of clustering during cellular tension events, experiments would need to be performed on a surface that allowed for clustering. Supported lipid bilayers are a likely candidate for this goal. Assuming that FRET is used as the tension probe readout, a method to distinguish increases in fluorescence intensity due to clustering of the probe on the bilayer from intensity changes resulting from receptor mediated tension would be needed. This could be provided by monitoring changes in the fluorescence intensity of a fluorophore bound to the probe but not associated with tension sensing measurements. Alternatively, a system that is inherently sensitive to fluorophore clustering, such as PRIM (proximity imaging), would allow clustering and cell tension to be concurrently monitored. Implementing imaging techniques such as FLIM (fluorescence lifetime imaging microscopy), which is insensitive to clustering effects, would also be beneficial.

5.3 References

1. Stabley, D.R., Jurchenko, C., Marshall, S.S. & Salaita, K.S. Visualizing mechanical tension across membrane receptors with a fluorescent sensor. *Nat. Methods* **2012**, *9*, 64-67.
2. Jurchenko, C., Chang, Y., Narui, Y., Zhang, Y. & Salaita, K.S. Integrin-generated forces lead to streptavidin-biotin unbinding in cellular adhesions. *Biophys. J.* **2014**, *106*, 1436-1446.

3. Jurchenko, C. & Salaita, K.S. Lighting up the force: Investigating Mechanisms of mechanotransduction using fluorescent tension probes. *Mol. Cell Biol.* **2015**, *35*, 2570-2582.
4. Zhang, Y., Ge, C., Zhu, C. & Salaita, K. DNA-based digital tension probes reveal integrin forces during early cell adhesion. *Nat. Commun.* **2014**, *5*, 5167.
5. Los, G.V. et al. HaloTag: A novel protein labeling technology for cell imaging and protein analysis. *ACS Chem. Biol.* **2008**, *3*, 373-382.
6. Morimatsu, M., Mekhdjian, A.H., Chang, A.C., Tan, S.J. & Dunn, A.R. Visualizing the interior architecture of focal adhesions with high-resolution traction maps. *Nano Lett.* **2015**, *15*, 2220-2228.
7. Gordon, W.R. et al. Mechanical allostery: Evidence for a force requirement in the proteolytic activation of Notch. *Develop. Cell* **2015**, *33*, 729-736.